STUDIES OF CHARMED BARYONS DECAYING TO $\Lambda_c^+(n\pi)$

By

JIU ZHENG

A DISSERTATION PRESENTED TO THE GRADUATE SCHOOL
OF THE UNIVERSITY OF FLORIDA IN PARTIAL FULFILLMENT
OF THE REQUIREMENTS FOR THE DEGREE OF
DOCTOR OF PHILOSOPHY

UNIVERSITY OF FLORIDA

1999

ACKNOWLEDGMENTS

Most of all, I would like to thank my adviser, John Yelton. He taught me from scratch how to do physics analysis in CLEO, introduced me to charmed baryon studies, and suggested a research topic which turned into this dissertation. Over five years he has been always very supportive in my work in physics and with many other aspects of my life.

I thank Paul Avery, who has taught me much about high energy physics, data analysis, and CLEO software. I gained a large part of my knowledge of elementary particles from his one year introductory course. The magnificent KNLIB he provided has given tremendous help to my analysis.

I am greatly indebted to my former college classmate, Song Yang, who influenced me to pursue the study of high energy physics. When he was a research associate at the University of Florida, he gave me much help with Monte Carlo simulations, Unix, C++, and GNU Make.

Thanks go to Craig Prescott for answering many of my questions about CLEO software and for engaging in much useful discussion about physics. My life in CLEO would have been much more difficult without him. His longtime maintenance and support of the CLEO software library have helped everybody in CLEO do better analyses. I used his Vee-finding library and primary-vertex-finding routine directly in my analysis.

I enjoyed lectures on "the Standard Model" by Pierre Sikivie and on "the Experimental High Energy Physics" by Guenakh Mitselmakher. I also thank Zongan Qui, Sergei Obukhov, and Charles Hooper for their first-year courses. I appreciate the help provided by my former colleagues, Jorge Rodriguez and Fadi Zeini. The Latex template provided by Youli Kanev and Mike Jones saved me a lot of time on writing this dissertation.

I would like to express my gratitude for the entire CLEO collaboration and all staff members in the Cornell Electron Storage Ring. I wish happiness and success to all high energy physicists. The world is a much better place with these people's dedication to answer the big, important questions.

Finally, I would like to thank my wife, Hongyan Yan. This work would have been impossible without her love and support. Much credit for this work goes to my mother, Chunyu Xu, my father, Zhiyi, and my father-in-law, Boxun. I have learned many things about life from my little son, David.

To my grandmothers

TABLE OF CONTENTS

Abstract of Dissertation Presented to the Graduate School
of the University of Florida in Partial Fulfillment of the
Requirements for the Degree of Doctor of Philosophy

STUDIES OF CHARMED BARYONS DECAYING TO $\Lambda_c^+(n\pi)$

By

Jiu Zheng

May 1999

Chairman: J. Yelton
Major Department: Physics

This dissertation presents studies of charmed baryons the Λ_{c1}^+, Σ_c, and Σ_c^*. The two Λ_{c1}^+ baryons are the $L = 1$ excited states of the Λ_c^+, and they decay to a Λ_c^+ and two pions; the Σ_c triplet is the spin 1/2 $I = 1$ state corresponding to the Λ_c^+; and Σ_c^* is the spin 3/2 excitation of the Σ_c. Both Σ_c and Σ_c^* decay to a Λ_c^+ and a pion. We performed comprehensive measurements on the masses, widths, fragmentation functions, and the production ratios of these particles from 10 GeV/c^2 e^+e^- annihilations.

A new decay channel of the Λ_{c1}^+, $\Lambda_c^+\pi^0\pi^0$, is first observed and its decay ratio relative to $\Lambda_c^+\pi^+\pi^-$ is reported. A detailed study of Λ_{c1}^+ decays through the intermediate Σ_c is performed.

The Σ_c intrinsic widths are first measured with consistency with theoretical predictions. The relative production ratios among the three Σ_c's are measured to be consistent with 1. The first evidence of the existence a new particle, the Σ_c^{*+}, is reported.

To my grandmothers

CHAPTER 1
THEORY OVERVIEW

1.1 Quark Model

Tremendous progress has been made in high energy physics since the beginning of this century. We now have a simple picture about the ultimate constituents of matter: All matter is composed of quarks, which carry fractional electric charges, and leptons, such as the electron and neutrino. A quark does not exist individually and strong interactions hold quarks together in hadrons, which are built from two types of quark combination: a baryon consists of three quarks and a meson consists of a quark and an antiquark.

Quarks come in six flavors (called d, u, s, c, b, and t), as do leptons (three types of charged and three of neutral). Each quark has spin 1/2 and baryon number 1/3. Table 1.1 shows the additive quantum numbers (other than baryon number) of the three generations of quarks. By convention each quark is assigned positive parity, so each antiquark has negative parity. The masses of quarks vary largely for different

Table 1.1: Additive quantum numbers of quarks.

Flavor	d	u	s	c	b	t
Charge	$-\frac{1}{3}$	$+\frac{2}{3}$	$-\frac{1}{3}$	$+\frac{2}{3}$	$-\frac{1}{3}$	$+\frac{2}{3}$
Isospin z-component	$-\frac{1}{2}$	$+\frac{1}{2}$	0	0	0	0
Strangeness	0	0	-1	0	0	0
Charm	0	0	0	+1	0	0
Bottomness	0	0	0	0	-1	0
Topness	0	0	0	0	0	+1

flavors,* ranging from a few MeV/c^2 for u and d quarks to about 170 GeV/c^2 for t quark. Since u and d are very light, the isospin SU(2) symmetry is a very good approximation. In the limit that isospin is an exact symmetry, the u and d quarks are considered identical except the charge difference.

Analogous to the photon in electromagnetic interactions, a strong coupling happens via a mediating boson, call a gluon. In the theory of quantum chromodynamics (QCD), there are six types of strong charge, called "color," representing an internal degree of freedom. A quark can carry one of the three red, blue, or green colors, and an antiquark can carry one of the corresponding anticolors. The quark-quark force is independent of quark color, so the color symmetry, SU(3), is exact.

All baryons are three-quark (qqq) states, and each such state is an SU(3) color singlet, a completely antisymmetric state of the three possible colors. Since quarks are fermions, the state function for any baryon must be antisymmetric under interchange of any two equal-mass quarks (up and down quarks in the limit of isospin symmetry). The state function of a baryon can be written as

$$|qqq\rangle_A = |color\rangle_A \times |space, spin, flavor\rangle_S,$$

where the subscripts S and A indicate symmetry or antisymmetry under interchange of any two of the equal-mass quarks.

For baryons made up of u, d, and s quarks, the three flavors imply and approximate flavor SU(3). This flavor SU(3) symmetry requires that a corresponding group of baryons belong to the multiplets on the right side of

$$\mathbf{3} \otimes \mathbf{3} \otimes \mathbf{3} = \mathbf{10}_S \oplus \mathbf{8}_M \oplus \mathbf{8}_M \oplus \mathbf{1}_A,$$

*The values of quark masses depend on precisely how they are defined. The quark masses we referred to here follow the meanings defined by the Particle Data Group [1], which are different from the constituent quark masses.

where the subscript M indicates mixed-symmetry states under interchange of any two quarks. Taking spin symmetry, SU(2), into account, the two $\mathbf{8}'_M s$ will end up with one octet of baryon states of $|spin, flavor\rangle_S$. This octet is shown as the bottom layer of Figure 1.1(a) In the ground state of the multiplet, the SU(3) flavor singlet **1** is forbidden by Fermi statistics. The decuplet formed by $\mathbf{10}_S$, shown as the bottom layer in Figure 1.1(b), contains the states with the three quark spins aligned to the same direction (spin $J = 3/2$).

If we add the c quark to the three light quarks, the flavor symmetry is extended to SU(4). The SU(4) multiples are shown in Figure 1.1(a) and Figure 1.1(b). All the particles in a given multiplet have the same spin and parity. Since the mass of the c quark is large, this SU(4) symmetry is very badly broken.

1.2 Heavy-Quark Effective Theory

1.2.1 QCD

In QCD, the Lagrangian describing the interactions of quarks and gluons is

$$L_{QCD} = -\frac{1}{4}F^{(a)}_{\mu\nu}F^{(a)\mu\nu} + i\sum_q \overline{\phi}^i_q \gamma^\mu (D_\mu)_{ij}\phi^j_q - \sum_q m_q \overline{\phi}^i_q \phi_{qi}, \tag{1.1}$$

$$F^{(a)}_{\mu\nu} = \partial_\mu A^a_\nu - \partial_\nu A^a_\mu + g_s f_{abc} A^b_\nu A^c_\nu,$$

$$(D_\mu)_{ij} = \delta_{ij}\partial_\mu - ig_s \sum_a \frac{\lambda^a_{i,j}}{2} A^a_\mu,$$

where g_s is the QCD coupling constant ($\alpha_s = g_s^2/4\pi$), and the f_{abc} are the structure constants of the SU(3) algebra. The $\phi^i_q(x)$ are the 4-component Dirac spinors associated with each quark field of color i and flavor q, and the $A^a_\mu(x)$ are the Yang-Mills gluon fields.

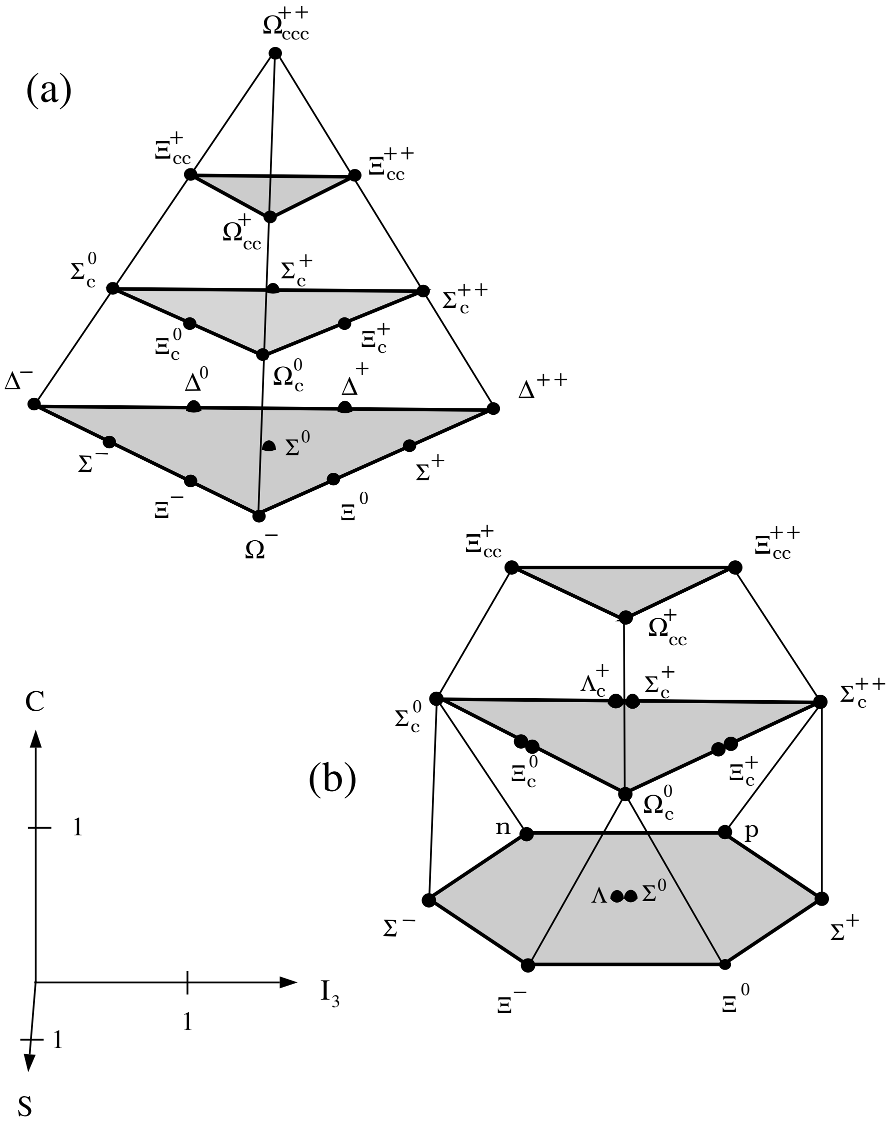

Figure 1.1: SU(4) multiplet of baryons made of u, d, s, and c quarks shown in (I_z, S, C) coordinates. (a) The 20-plet with an SU(3) decuplet. (b) The 20-plet with an SU(3) octet.

QCD is believed to be the fundamental theory of strong interactions. But to date, there are no practical means to do full QCD calculations of hadron masses and their decay widths, and a variety of different approximate methods have been introduced. Potential models have been well recognized to be the most useful in understanding the mass spectrum and the decay patterns of heavy-flavor hadrons. The correlation between flavor and spin wave functions is outside the realm of QCD. Some assumptions can be made using the empirical evidence of the constituent quark model. Heavy-hadron perturbation theory can be used to predict the decay widths.

1.2.2 Potential Models

Although the details of modern potential models have evolved greatly since the discovery of J/ϕ, the essential features remain unchanged. The potential between two quarks is often taken to be of the form

$$V_s = -\frac{4}{3}\frac{\alpha_s}{r} + kr,$$

where r is the inter-quark separation, and $\alpha_s \sim 1$, about two orders larger than α, represents the magnitude of the strong coupling. The factor $4/3$ holds for the interaction between a quark and an antiquark. It is $2/3$ for the interaction between two quarks. The first term dominating at small distance r arises from a single gluon exchange, and the linear term is associated with the confinement of quarks and gluons inside hadrons at large r. Because of the linear term, attempts to free a quark from a hadron simply result in the production of new $q\overline{q}$ quark-antiquark pairs. The annihilation process $e^+e^- \to$ hadrons is viewed in terms of the process $e^+e^- \to q\overline{q}$ followed by "fragmentation" of the quark and antiquark into hadrons. One important feature of potential models is that, except for mass dependencies, the inter-quark potential is independent of quark flavor.

Potential models cannot be formally derived from QCD, but they can be interpreted by it. In QCD, the short-distance behavior is dominated by one gluon exchange described in the lowest-order perturbation theory. The linear behavior at large r can be seen by considering that a $q\overline{q}$ pair are attracted to each other and a color flux tube forms between them. Lattice calculations suggest that the tension per unit length in this flux tube is a constant[2, 3], and therefore the energy stored in the tube is proportional to the separation of the charges. Finally, couplings described in QCD are flavor independent.

The most well-known and successful potential model is described Isgur, et al. [4, 5, 6]. Early models[5, 6] are non-relativistic and later they are improved by adding some relativistic terms[4]. The Hamiltonian of a baryon is,

$$H = \sum_{i=1}^{3}(m_i + \frac{p_i^2}{2m_i}) + \sum_{i<j}(H_c^{ij} + H_{BF}^{ij}), \tag{1.2}$$

$$H_c^{ij} = -\frac{2}{3}\frac{\alpha_s}{r} + a + br,$$

$$H_{BF}^{ij} = c_i \overrightarrow{L}_{ij} \cdot \overrightarrow{S}_i + c_j \overrightarrow{L}_{ij} \cdot \overrightarrow{S}_j + c_T(3\overrightarrow{S}_i \cdot \hat{r}\overrightarrow{S}_j \cdot \hat{r} - \overrightarrow{S}_i \cdot \overrightarrow{S}_j) + c_H \overrightarrow{S}_i \cdot \overrightarrow{S}_j,$$

where i, j run over all quarks inside the baryon, and

$$c_k = (\frac{1}{m_k^2} + \frac{1}{m_i m_j})\frac{4}{3}\frac{\alpha_s}{r^3} - \frac{1}{2m_k^2}\frac{b}{r}, \quad k = i, j,$$

$$c_T = \frac{1}{m_i m_j}\frac{4}{3}\frac{\alpha_s}{r^3},$$

$$c_H = \frac{8\pi}{3}\frac{1}{m_i m_j}\frac{4}{3}\frac{\alpha_s}{r}\delta^3(\overrightarrow{r}).$$

H_c^{ij} is the confinement term, and the spin-dependent term H_{BF}^{ij} is very similar to the Breit-Fermi Hamiltonian of atomic and nuclear physics. It is very crucial that in H_c the α_s and b terms have opposite signs, and the two contributions to the spin-orbit coupling cancel almost exactly. Since this model does not perform a full relativistic treatment, it is called a "relativized" quark potential model. Compared with non-relativistic models, it has slightly different values of a and b.

In the limit of $m_Q \to \infty$, where Q indicates the heavy quark, the Hamiltonian is simplified and a new good quantum number $\vec{j}_l$, the total angular momentum of the light degrees of freedom, is introduced. $\vec{j}_l$ is the direct analogy with the total angular momentum of the electron in a hydrogen atom.

1.2.3 Heavy-Quark Chiral Perturbation Theory

The quark contribution to the QCD Lagrangian in equation 1.1 can be considered to have two parts. The first comes from the light degrees of freedom, and the second part is from heavy quarks. Each of the two parts has distinct symmetry.

The light-quark part of the Lagrangian has a flavor $SU(3)_L \times SU(3)_R$ chiral symmetry in the limit that the light-quark masses are set to zero. $SU(3)_L \times SU(3)_R$ is only an approximate symmetry since the quark masses explicitly break it. This chiral symmetry is spontaneously broken and leads to eight massless Goldstone bosons, the π's, K's, and η. Their couplings to hadrons are determined by PCAC (partial conservation of axial-vector current) and current algebra, or, alternatively, by the nonlinear chiral Lagrangians.

For the heavy-quark part, in the limit of infinite quark masses, the dynamics of a heavy quark in QCD depends on its velocity and is independent of its mass and spin. As a consequence, a new flavor and spin symmetry appear for hadrons containing one heavy quark. This symmetry is called heavy-quark symmetry. Many models based on different approaches have been proposed by theorists from [7, 8, 9, 10, 11, 12, 13, 14, 15, 16]. This new symmetry implies that the excitation spectrum and the transition form factors in weak decays of heavy hadrons are independent of the heavy-quark species and heavy-quark spins. This is similar to a hydrogen-like atom in QED having an excitation spectrum and transition matrix elements independent of the mass and spin of the nucleus.

Since heavy hadrons contain both heavy and light quarks, both the chiral symmetry of the light quarks and heavy-quark symmetry affect the low-energy dynamics of heavy hadrons interacting with the Goldstone bosons. Experimentally, strong decays such as $\Sigma_c \to \Lambda_c^+ \pi$ involving soft pions give such examples.

1.3 Introduction to Charmed Baryons decaying to $\Lambda_c^+(n\pi)$

1.3.1 Spectroscopy

The charmed baryons which are covered in this work are those containing a c quark and two u or d quarks. The two light quarks are often referred to as a diquark. In the $m_c \to \infty$ limit, the total angular momentum of the light constituents,

$$\vec{j}_l = \vec{S}_l + \vec{L},$$

become a good quantum number. Here $\vec{S}_l$ is the total spin of the two light quarks and $\vec{L}$ is the orbital angular momentum between the c quark and the two light quarks. In potential models, $\vec{j}_l$ has an analogy with the total angular momentum of an electron in a hydrogen atom. Therefore, the properties of a charmed baryon are mostly dictated by its light-quark contents. In HQET, the final angular momentum of the baryon is given as

$$\vec{J} = \vec{j}_l + \vec{S}_c,$$

where $\vec{S}_c$ is the spin of the c quark.*

*For $L = 0$, we simply have $\vec{J} = \vec{S}_l + \vec{S}_c$. But when L is non-zero, the angular momenta can be coupled as either $\vec{J} = (\vec{S}_c + \vec{S}_l) + \vec{L}$ or $\vec{J} = \vec{S}_c + (\vec{S}_l + \vec{L})$. Although the final physics

Table 1.2: The s-wave (both L and L_l are 0) and p-wave (either L or L_l is 1) charmed baryons and their quantum numbers: isospin (I), orbital angular momentum between the diquark and the c quark (L), orbital angular momentum between the two light quarks (L_l), total spin of the diquark (S_l), total angular momentum of the light degree of freedom (j_l), and spin-parity of the baryon (J^P). S_l and j_l are good quantum numbers in the limit of $m_c \to \infty$.

State	I	L	L_l	S_l	j_l	J^P
Λ_c^+	0	0	0	0	0	$\frac{1}{2}^+$
Σ_c	1	0	0	1	1	$\frac{1}{2}^+, \frac{3}{2}^+$
Λ_{c1}	0	1	0	0	1	$\frac{1}{2}^-, \frac{3}{2}^-$
Σ_{c0}	1	1	0	1	0	$\frac{1}{2}^-$
Σ_{c1}	1	1	0	1	1	$\frac{1}{2}^-, \frac{3}{2}^-$
Σ_{c2}	1	1	0	1	2	$\frac{3}{2}^-, \frac{5}{2}^-$
Λ'_{c0}	0	0	1	1	0	$\frac{1}{2}^-$
Λ'_{c1}	0	0	1	1	1	$\frac{1}{2}^-, \frac{3}{2}^-$
Λ'_{c2}	0	0	1	1	2	$\frac{3}{2}^-, \frac{5}{2}^-$
Σ'_{c1}	1	0	1	0	1	$\frac{1}{2}^-, \frac{3}{2}^-$

The properties of all $L = 0$ (s-wave) and $L = 1$ (p-wave) baryons of cuu, cud, and cdd states are listed in Table 1.2. The lowest-lying $L = 0$ state is the Λ_c^+, a cud state in which the ud diquark has isospin of $I = 0$. The state is antisymmetric under the exchange of the u and d quarks. Since it is required that the total $|spin, flavor\rangle$ be symmetric, the spin state has to be antisymmetric. The the ud diquark must be in a $S_l = 0$ state. Combining S_l with the spin of the c quark gives a total spin of $J = 1/2$. By convention, the Λ_c^+, like all spatial ground state baryons, has positive parity.

For Σ_c states, which have $I = 1$, the diquark must have $S_l = 1$ to satisfy the requirement of $|spin, flavor\rangle$ being symmetric. Adding $S_l = 1$ with the spin of the

does not depend on the order of coupling, the latter choice leads to a larger amount of algebra in the calculations of most of the HQET models. The choice of $\overrightarrow{J} = \overrightarrow{S}_c + \overrightarrow{j}_l$ coupling also helps us derive the physical states more easily.

c quark results a doublet having $J^P = 1/2^+$ (Σ_c) and $J^P = 3/2^+$ (Σ_c^*). Λ_c^+, Σ_c, and Σ_c^* are called s-wave particles since there is no orbital angular momentum involved.

It is worthing mentioning that we have the similar $L = 0$ states in the strange baryon sector, Λ, Σ, and Σ^*. An important fact is that

$$\frac{M(\Sigma_c^*) - M(\Sigma_c)}{M(\Sigma^*) - M(\Sigma)} \sim \frac{m_s}{m_c},$$

for the hyperfine splittings. Based on HQET, a hyperfine splitting arises from the color magnetic moment of the heavy quark. Since $m_s/m_c \simeq 1/3$, the $M(\Sigma_c^*) - M(\Sigma_c)$ is expected to be about one-third of $M(\Sigma^*) - M(\Sigma)$.

Now Let us consider the lowest-lying $L = 1$ (p-wave) particles. In the $I = 0$ case, there must be $S = 0$ for the same reason as for the Λ_c^+ baryon, so $j_l = 1$. The c quark brings hyperfine splitting to give two baryon states of $J^P = 1/2^-$ and $J^P = 3/2^-$, where the negative parity comes from the one unit of the orbital angular momentum. This doublet is named Λ_{c1}.

Same as Σ_c, for $I = 1$, we have $S = 1$. This gives $j_l = 0, 1, 2$. Each of these is split by its hyperfine interaction with the c quark. This type of excitation ends up with five baryons: the Σ_{c0} singlet, the Σ_{c1} doublet, and the Σ_{c2} doublet.

Another type of p-wave states come from one unit of the orbital angular momentum between the two light quarks, $L_l = 1$. This implies that the $I = 0$ ud diquark must have $S = 1$. This produces $j_l = 0, 1, 2$. Then the hyperfine splittings give five baryon states: the Λ'_{c0} singlet, the Λ'_{c1} doublet, and the Λ'_{c2} doublet.

Finally, it can be easily derived that $L_l = 1$ and $I = 1$ require $S = 0$. Then the hyperfine splitting gives a doublet of Σ'_{c1} baryons. Note that the degeneracy of the $L = 1$ ($L_l = 1$) and $L_l = 1$ ($L = 1$) switches with the change from $I = 0$ to $I = 1$.

1.3.2 Strong Decays

All the charmed baryons we described in the last section will decay to the Λ_c^+, since it is the lowest state of u, d, c compositions. The purpose of these research work is to get better understanding on how the $\Sigma_c^{(*)}$ baryons and even p-wave charmed baryons decay to Λ_c^+.

To date, only the Σ_c triplet, two states of the Σ_c^* triplet, and the Λ_{c1} doublet have been found, and only strong decays through one or two pions have been observed. Based on the mass predictions by the relativized potential model[4], other p-wave baryons may decay strongly to the final states containing a Λ_c^+ and one, two, or three pions, but this work failed see any more p-wave states higher than the Λ_{c1}. In general, the higher states which have the same decay modes are expected to be wide and difficult to observe. So this dissertation only reports the studies of the $\Sigma_c^{(*)}$ and Λ_{c1} baryons. This subsection gives a brief review of the strong decays of these baryons.

The selection rules of these decay can be easily derived from conservation of parity and angular momentum. For a strong decay $A \to BC$, where the spin-parities of these particles are denoted by $J_A^{P_A}$, $J_B^{P_B}$, and $J_C^{P_C}$, and a possible orbital angular momentum between B and C is denoted by L_{BC}, it is required that L must satisfy

$$\overrightarrow{J}_A = \overrightarrow{L}_{BC} + \overrightarrow{J}_B + \overrightarrow{J}_C,$$

and

$$P_A = P_B P_C (-1)^{L_{BC}}$$

in order to decay with a partial wave corresponding to L_{BC}. In addition, isospin has to be conserved in all strong decays.

Table 1.3: Allowed partial waves for strong decays of the $\Sigma_c^{(*)}$ and Λ_{c1} baryons. The $\Lambda_c^+\pi\pi$ mode listed in the table only represents the non-resonance decay mode.

Particle	Decay Mode	Allowed Partial Wave
Σ_c	$\Lambda_c^+\pi$	P
Σ_c^*	$\Lambda_c^+\pi$	P
$\Lambda_{c1}(1/2)$	$\Lambda_c^+\pi\pi$	P
$\Lambda_{c1}(1/2)$	$\Sigma_c\pi$	S
$\Lambda_{c1}(3/2)$	$\Lambda_c^+\pi\pi$	P
$\Lambda_{c1}(3/2)$	$\Sigma_c\pi$	D

Table 1.3 lists the all the possible decay channels for strong decays of the $\Sigma_c^{(*)}$ and Λ_{c1} baryons. The $\Sigma_c^{(*)}$ baryons do not have the $\Lambda_c^+\pi\pi$ decay because there is no phase space. They should entirely decay through $\Lambda_c^+\pi$. The Λ_{c1} baryons do not have the $\Lambda_c^+\pi$ decay because of isospin conservation. Based on the table, we should expect that the S-wave $\Sigma_c\pi$ would dominate the $\Lambda_{c1}(1/2)$ decay. The $\Lambda_{c1}(3/2)$ can only have D-wave $\Sigma_c\pi$ decay because of the conservation of total angular momentum; the $\Lambda_{c1}(3/2)\rightarrow\Sigma_c^*\pi$ decay would be S-wave, but is kinematically forbidden. Thus we should expect that P-wave non-resonance $\Lambda_c^+\pi\pi$ decay dominates the $\Lambda_{c1}(3/2)$ decay.

1.4 HQET Predictions on $\Sigma_c^{(*)}$ and Λ_{c1}^+

Many quark models have the ability to make quantitative predictions on heavy-baryon masses, and almost all of such models use the "constituent quark masses" which are derived from well-known hadron masses. Predictions vary from model to model, and they all fall in roughly the same range. Among all the models, the quark potential model developed by Isgur et al.[4, 6] is the most complete, and it covers all the baryons from the proton to bottom baryons.

Table 1.4: The constituent quark mass assumptions by the potential models. All numbers are in units of MeV/c^2.

Quark	Non-relativistic Model	Relativized Model
u	350	220
d	350	220
s	550	419
c	1500	1628
b	5000	4977

Table 1.5: Some charmed baryon mass predictions by the potential models in comparison with average values of experiments. All numbers are in units of MeV/c^2. All uncertainties of the experiments measured numbers are less than 3 MeV/c^2.

Quark	Non-relativistic Model	Relativized Model	Experiment
Λ_c^+	2260	2265	2285
Σ_c	2440	2440	2453
Σ_c^*	2510	2495	2518
$\Lambda_{c1}^+(1/2)$	2510	2630	2594
$\Lambda_{c1}^+(3/2)$	2590	2640	2627

An important part of the potential models is to specify the constituent masses of quarks. Typical values used in both non-relativistic models and relativized models are listed in Table 1.4. Although they use different mass assumptions, both models work extremely well for light baryons and strange baryons, and their predictions on charmed baryons are also close. Table 1.5 lists some of the predictions[4, 6] compared with the average experimental values[1].

Potential model also predicted the masses of other p-wave charmed baryons. The masses of Σ_{c0} (the next state higher than Λ_{c1}) and Σ_{c1} doublet are predicted to lie around 2770 MeV/c^2, within 10 MeV/c^2. Other nine states are also close to each other in masses and range from 2780 MeV/c^2 to 2900 MeV/c^2. Based on these predictions, unless some of these states have very narrow width, it would be difficult to see them. In our work, we looked at these mass ranges for $\Lambda_c^+\pi^\pm$ and $\Lambda_c^+\pi^+\pi^-$decays, and did not see any obvious signals.

The potential models can make calculations on decay widths but do not work very well. Their predictions are very rough and agree with experimental values only in their order of magnitude.

The most-recognized theoretical model which can predict heavy-hadron widths was developed by Yan et al.[16], who used the nonlinear chiral quark model[17] to calculate heavy-quark coupling to the Goldstone bosons. In a charmed baryon, the diquark with $s_l^{P_l} = 1^+$ can be represented by an axial-vector field ϕ_μ; and the diquark with $s_l^{P_l} = 0^+$ can be represented by a Lorentz scalar field ϕ. The decays $\phi_\mu \to \phi'_\mu + \pi$ and $\phi_\mu \to \phi + \pi$ can be described by two independent coupling constants g_1 and g_2, respectively. For the decay $\Sigma_c \to \Lambda_c^+\pi$, the decay rate is determined by g_2 and masses of the Σ_c, Λ_c^+, and π. Their mode predicts

$$g_2 = -\frac{2}{3} g_A,$$

where g_A is the coupling constant in the single-quark transition $u \to d$. g_A is generally assumed to have a value of 1, but the experimental extracted value is 0.75[17]. g_2 values are not very different from other theoretical predictions[18, 19, 20]. Their Lagrangian gives the following decay width:

$$\Gamma(\Sigma_c^0 \to \Lambda_c^+\pi^-) = \frac{g_2^2}{2\pi f_\pi^2} \frac{M_{\Lambda_c^+}}{M_{\Sigma_c^0}} p_\pi^3, \tag{1.3}$$

$$\Gamma(\Sigma_c^{*0} \to \Sigma_c^+\pi^-) = \frac{g_1^2}{16\pi f_\pi^2} \frac{M_{\Sigma_c^+}}{M_{\Sigma_c^{*0}}} p_\pi^3, \tag{1.4}$$

where $f_\pi = 93$ MeV$/c^2$ is the pion decay constant and p_π is the pion momentum in the center of mass frame. equation 1.3 predicts the total width of Σ_c^0 since Σ_c decays 100% to $\Lambda_c^+\pi$. equation 1.4, however, is invalid since the decay $\Sigma_c^* \to \Sigma_c\pi$ is kinematically forbidden. If we neglect the radiative decay width associated with the decay $\Sigma_c^* \rightarrow \Sigma_c \gamma$,* the total width of Σ_c^* is given by

$$\Gamma(\Sigma_c^*) = \frac{g_2^2}{2\pi f_\pi^2} \frac{M_{\Lambda_c^+}}{M_{\Sigma_c^*}} p_\pi^3. \tag{1.5}$$

$g_2 = 0.612$ (with $g_A = 0.75$) will lead to

$$\Gamma(\Sigma_c) = 2.45 \text{ MeV}/c^2,$$

$$\Gamma(\Sigma_c^*) = 17.6 \text{ MeV}/c^2, \quad \text{if} \quad M_{\Sigma_c^*} - M_{\Lambda_c^+} = 233.5 \text{ MeV}/c^2.$$

Equations 1.3 and 1.5 show that the Σ_c width is directly related to the Σ_c^* width, which has been reported by CLEO collaboration[21]. This work includes the first attempt to measure that Σ_c width. If these widths can be measured accurately, g_2 can be derived from equation 1.3 or equation 1.4 and then further predicts the widths of other particles, for example, Ξ_c^*.

Recently Pirjol and Yan[22] included all possible strong-interaction couplings (S-wave, P-wave, and D-wave) among and between s-wave and p-wave baryons in the chiral Lagrangian. This model contains 45 independent coupling constants up to and including D-wave interactions. Besides g_1 and g_2, coupling constants h_2, h_3, h_4, ... are involved, which correspond to the p-wave baryons. In this theory, they derived model-independent sum rules which contain these couplings and relate them to properties of the lowest-lying baryons. However, couplings h_2 and h_8, which correspond to lowest p-wave baryons, cannot be directly predicted from the constituent quark model. Using published Λ_{c1}^+ masses[1] $M(\Lambda_{c1}^+(2593) - \Lambda_c^+) =$

---

*A radiative decay can happen when the strong decay is largely suppressed. Since the widths of scst$\rightarrow\Sigma_c\pi$ decays have been measured to be around 16 MeV/c^2, there should be almost no radiative decay.

308.6 MeV/c^2 and $M(\Lambda_{c1}^+(2625) - \Lambda_c^+) = 341.5$ MeV/c^2 together with $g_2 = 0.57$,* and neglecting radiative modes $\Lambda_{c1}^+ \to \Lambda_c^+\gamma$, they calculated

$$\Gamma(\Lambda_{c1}^+(2593)) = 11.9h_2^2 + 13.8h_8^2 - 0.042h_2h_8 \ (\mathrm{MeV}/c^2),$$

$$\Gamma(\Lambda_{c1}^+(2625)) = 0.52h_2^2 + (0.15 \times 10^6)h_8^2 - 5.2h_2h_8 \ (\mathrm{MeV}/c^2).$$

With $\Gamma(\Lambda_{c1}^+(2593))$ and $\Gamma(\Lambda_{c1}^+(2625))$, the values of h_2 and h_8 can be obtained, and they can be used to further estimate the width of other particles. Based on the published values of $\Gamma(\Lambda_{c1}^+(2593))$ and $\Gamma(\Lambda_{c1}^+(2625))$[1], it can be estimated that

$$h_2 = 0.57^{+0.32}_{-0.20},$$

$$h_8 < 3.5 \times 10^{-3} \ (\mathrm{MeV}/c^2)^{-1}.$$

They further estimated that Σ_{c0} and Σ_{c1}have widths larger than 100 MeV/c^2, If these estimates are correct, it will be very diffucult to observe signals of next-level higher state baryons.

*This value is the average value obtained from applying published masses[21] $M(\Sigma_c^{*++} - \Lambda_c^+) =$ 234.5 MeV/c^2 and $M(\Sigma_c^{*0} - \Lambda_c^+) = 232.6$ MeV/c^2 to equation 1.5.

CHAPTER 2
EXPERIMENTAL FACILITIES

2.1 CESR

The Cornell Electron Storage Ring (CESR) is an electron-positron collider with a circumference of 768 meters located on the campus of Cornell University, Ithaca, NY. It can produce collisions between electrons and positrons with center-of-mass energies between 9 and 12 GeV/c^2. It serves both CLEO for the study of particle physics, and the Cornell High Energy Synchrotron Source (CHESS) for a variety of biological and surface physics studies.

A diagram of CESR's main components is shown in Figure 2.1. This accelerator consists of three major parts: (1) the linear accelerator (LINAC), (2) the synchrotron, and (3) the storage ring. Electrons are accelerated to 150 MeV/c^2 by the 150-foot LINAC. Positrons are created by 50 MeV/c^2 electrons colliding with a thin tungsten target part-way through the LINAC. The electrons and positrons are then boosted to the operating energy of about 5 GeV/c^2 by the synchrotron and transferred into the storage ring, where they can be maintained in the storage ring for about 1 hour in order to achieve the highest integrated luminosity.

Electrons and positrons travel in opposite directions around the storage ring in evenly spaced bunches (currently there are 9) at 390,000 revolutions per second. Electrostatic separators hold the electron beam and the positron beam slightly apart from each other, and two beams only collide in one place — the center of the CLEO-II detector.

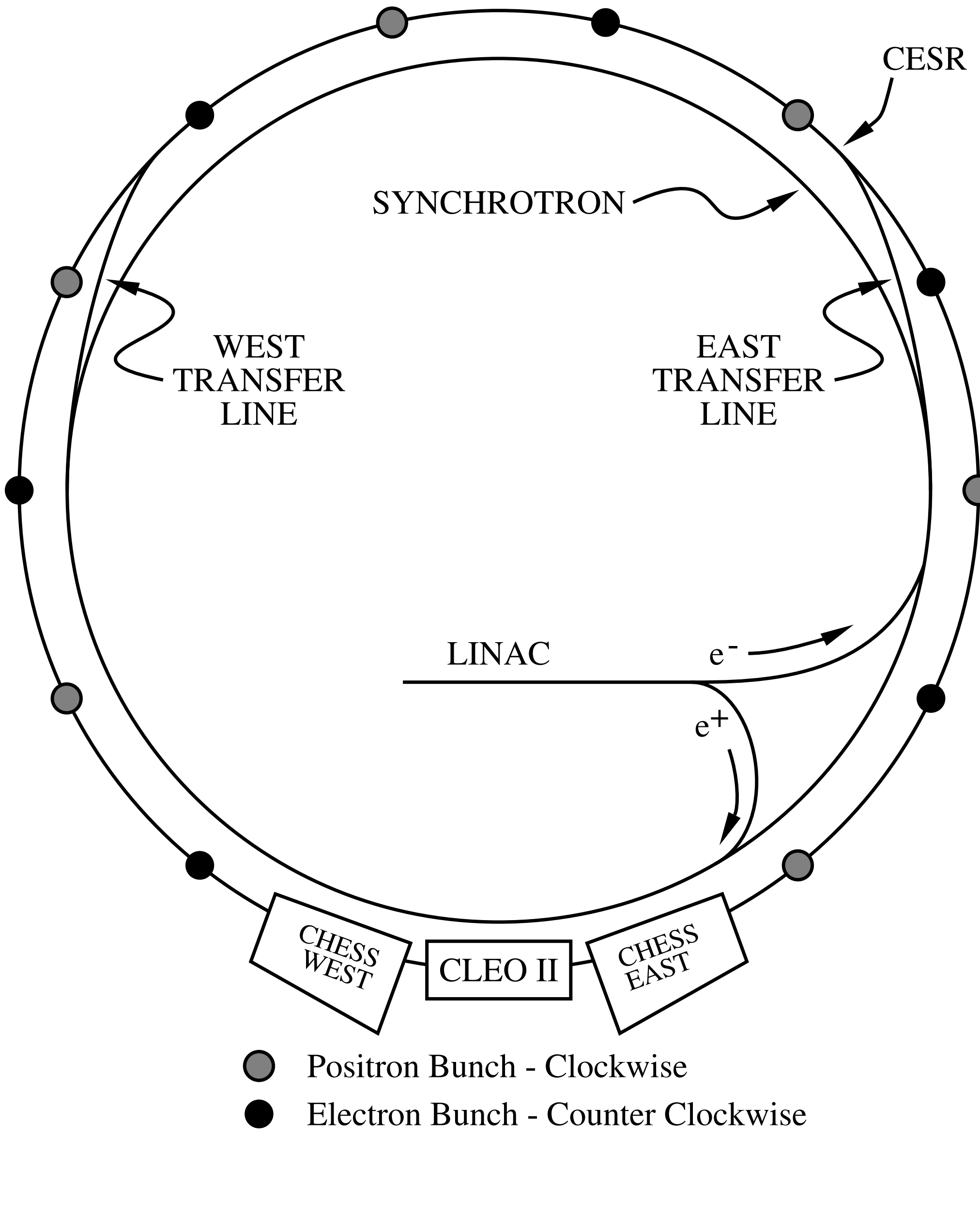

Figure 2.1: CESR layout. The CESR lies in a tunnel 50 feet underground. CLEO-II and the LINAC reside in Wilson Lab.

2.2 CLEO-II

CLEO-II is a multipurpose high energy physics detector incorporating excellent charged and neutral particle detection and measurement used to analyze electron-positron collision events generated by CESR. It is operated by the CLEO collaboration of over 200 physicists from many institutions, including the University of Florida.

Side and end views of the detector are shown in Figure 2.2 and Figure 2.3, respectively. The major components (going outward from the beam pipe) are the central detector (CD) which forms the tracking system, the time of flight (TOF) system, the electromagnetic calorimeter (CC), the 1.5-Tesla superconducting magnet, and muon chambers. The central detector comprises the Precision Tracking Layer (PTL), the Vertex Detector (VD), and the Drift Chamber (DR). CLEO-II is also equipped with timing, trigger, and data acquisition systems. Brief description of the CD, TOF, and CC are given in the following since they are the most important in this analysis.

2.2.1 Tracking System

Charged particle momentum is measured by three cylindrical, coaxial wire chambers sharing a common axis in the direction of the beams.

Figure 2.4 shows the structure of PTL and VD. The PTL is a cell-strawtube-drift-chamber which extends within 1 cm of the 3.5 cm beam pipe. The device consists of 6 layers of mylar tubes with 64 axial wires per layer. It is used to make precise measurement of the transverse position of the particle near the interaction point, with a resolution of 90 μm; and it does not provide longitudinal information. The VD covers the radial region from 7.5 to 17.5 cm. It has 10 layers of hexagonal cells as shown in Fig. 2.4. arranged in 10 layers. The VD provides a tracking resolution of 150 μm in $r - \phi$ and 0.75 mm in z.

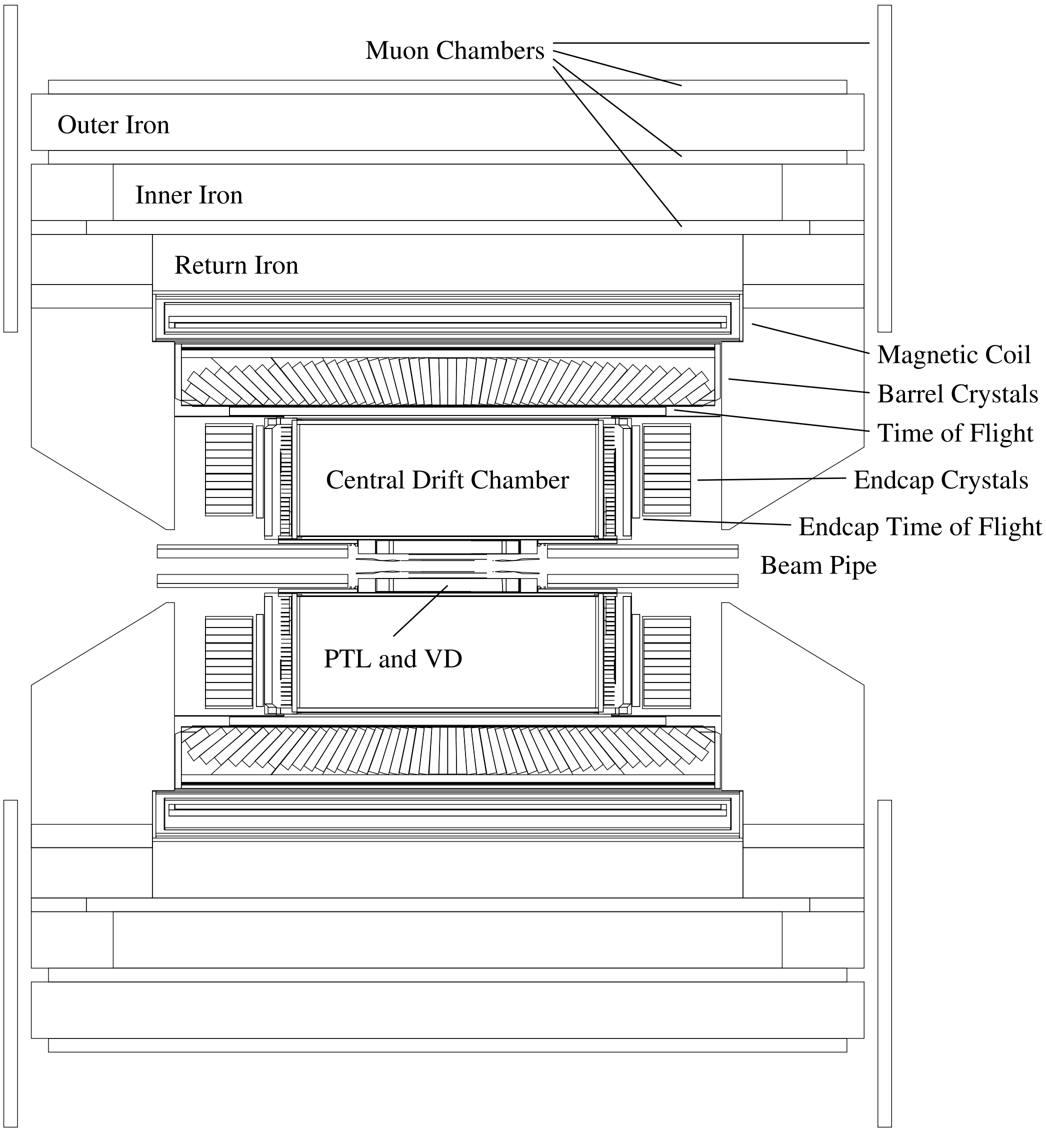

Figure 2.2: Side view of the CLEO-II Detector.

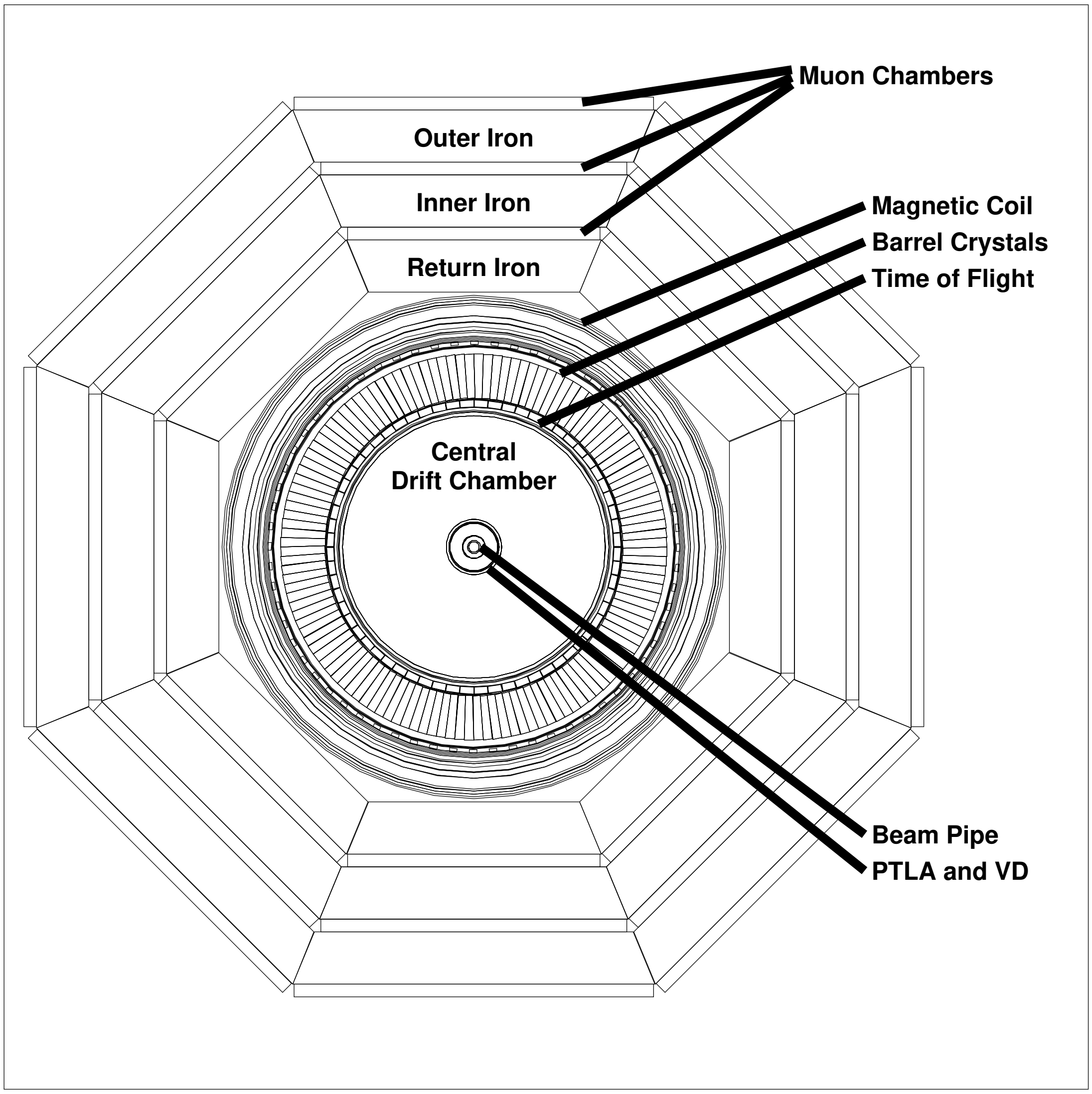

Figure 2.3: End view of the CLEO-II detector.

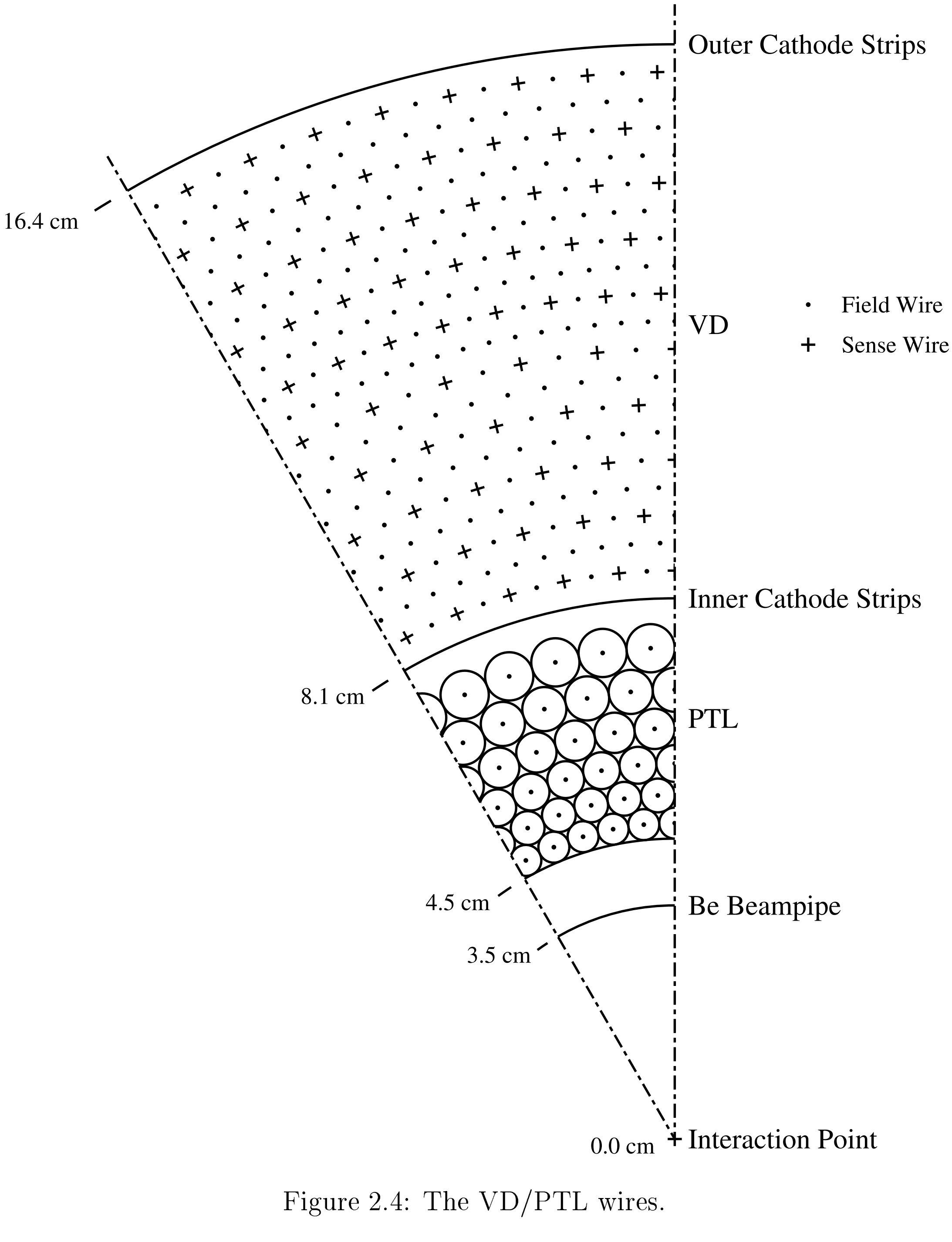

Figure 2.4: The VD/PTL wires.

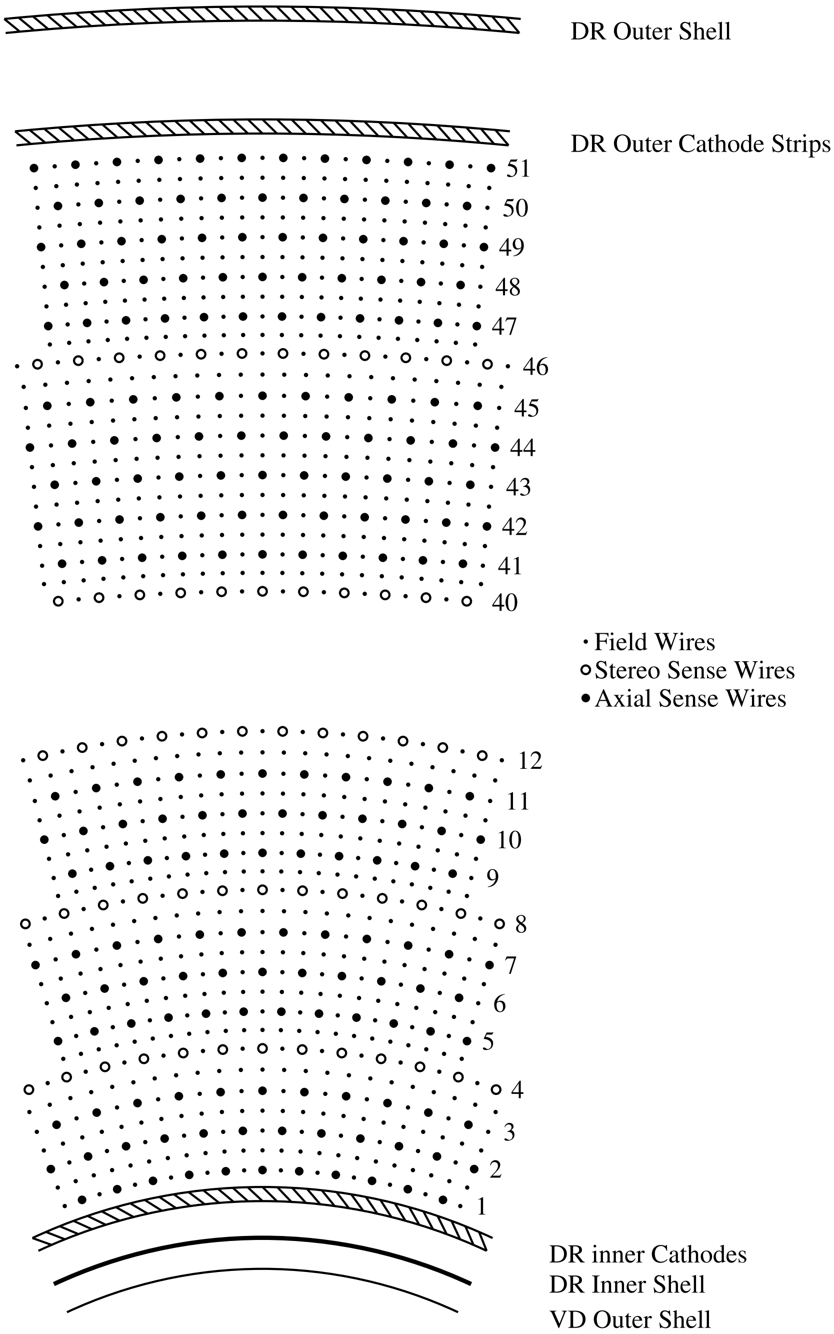

Figure 2.5: The DR wires.

Transverse and longitudinal momentum are best measured by DR, shown in Figure 2.5. This 51-layer outer drift chamber extends from 17.5 cm to 95 cm, including 12,240 sense wires and 36,240 wires. One sense wire and three field wires make a rectangular cell structure. There are 40 axial (parallel to the beam line) layers and 11 stereo (not parallel to the beam line) layers. Axial layers measure transverse momentum, the radial distance of the closest approach to the beam line, and the azimuthal direction of tracks. The stereo layers and 2 cathode layers measure the polar angle and the longitudinal position of the intersection of the track with the beam axis. Sequential layers are offset in azimuth in order to resolve left-right ambiguity in drift distance. An $r - \phi$ position resolution of 110 μm for the axial wires and a z position resolution of about 3 cm can be obtained with this chamber.

Particles can be identified from the specific ionization energy loss (dE/dx) in the DR. The characteristic bands of dE/dx quantity as a function of momentum for different species of particles are shown in Figure 2.6. Protons can be well separated from other particles at momenta below 1 MeV/c, and separation between pions and kaons is possible only below 400 MeV/c.

Track-reconstruction programs are used to find a charged-particle track in an event. First, the pattern of hits, which are the records of the wirescaused by the ionized gas molecules, are recognized; then these hits are fitted to obtain the trajectory of the original particle.

The data from all three chambers are combined to measure the momentum vector of charged particles. Two major factors limit the momentum resolution — multiple scattering and the position resolution of the track. Multiple scattering dominates the resolution at low momentum, and the position resolution dominates at high momentum, where the track curvature is small.

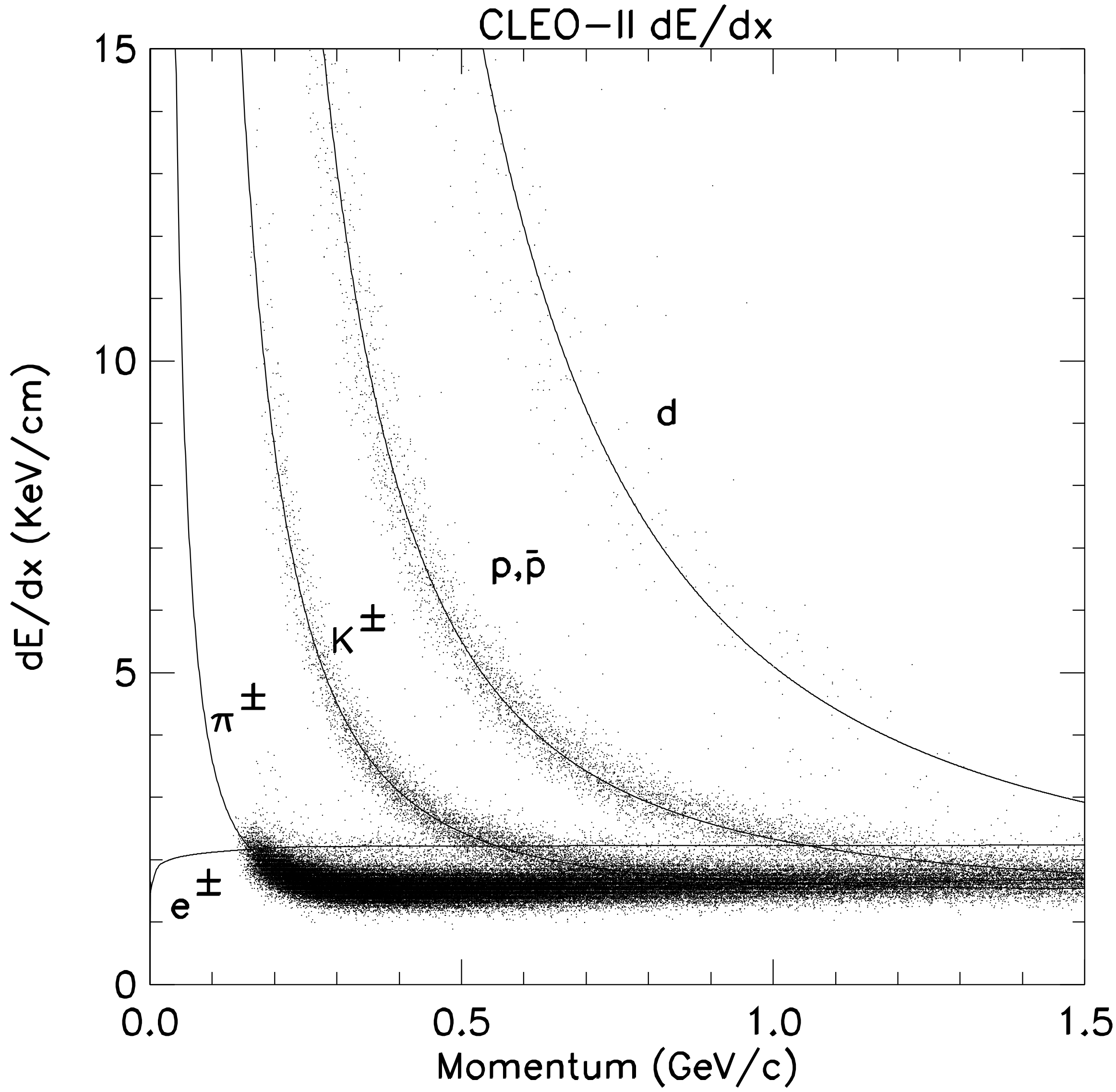

Figure 2.6: dE/dx plotted against momentum for different particles.

The CLEO-II charged-track momentum resolution has been measured to be

$$\delta p/p = \sqrt{0.005^2 + (0.0015)^2 p^2}$$

where the momentum p is in GeV/c. The first term represents the contribution from multiple scattering, and the second term is the contribution from the curvature measurement error. The two terms give equal contributions at a momentum of 3.3 GeV/c.

Charged particles with a transverse momentum greater than 225 MeV/c and a polar angle less than 45° will reach the outer radius of the DR and pass through the TOF counters and crystal calorimeter. These tracks are the best measured in the CLEO-II detector.

2.2.2 Time-of-Flight System

Besides dE/dx measurement in DR, the TOF device is also an important tool for particle identification. The TOF system has two major parts: a barrel system covering polar angles from 36° to 144°, and an endcap system covering polar angles from 15° to 36° on one side and 144° to 165° on the other side.

The barrel system, which is located immediately outside the DR, consists of 64 plastic rectangular scintillation counters, and an endcap system consists of the same but wedge-shaped counters. The scintillators are 5 cm thick and 2.5 m long. Lucite light pipes are attached at each end of the scintillators and connected to photomultiplier tubes.

It takes a 500 MeV/c pion about 3.5 ns to travel from the interaction region to the barrel TOF counters, while it takes a kaon about 4.5 ns. The time resolution for pions in hadronic events is about 150 ps. Figure 2.7 plots $1/\beta$ ($\beta = v/c$) against momentum. As we can see in the plot, the distinction in the bands separates $K - \pi$

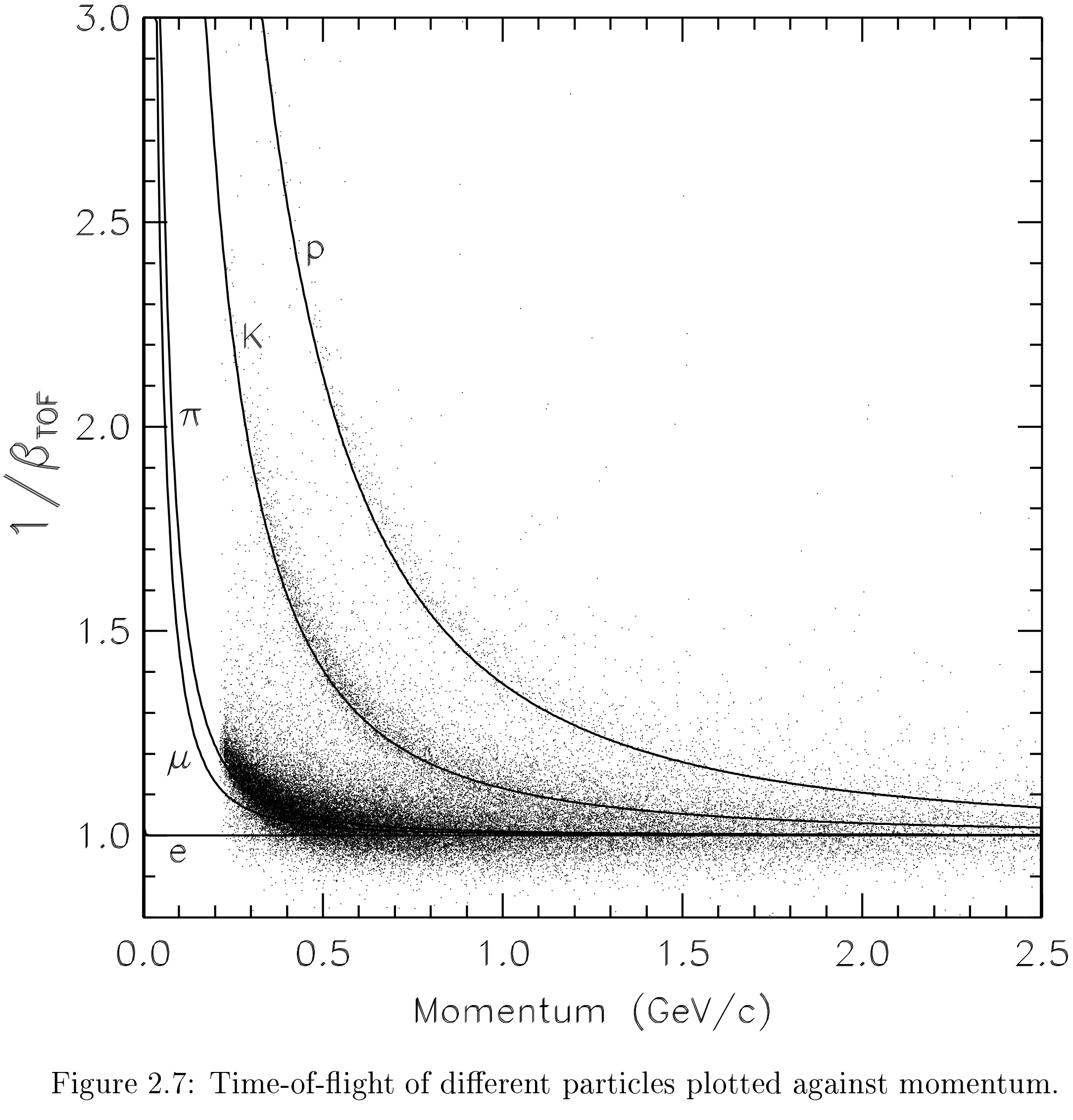

Figure 2.7: Time-of-flight of different particles plotted against momentum.

up to momenta of about 1.1 GeV/c, and protons can be separated up to momenta of about 1.5 GeV/c^2. Like the energy loss information, particles can not be well identified by TOF at high momentum.

2.2.3 Electromagnetic Calorimeter

The CsI crystal calorimeter is used to detect photons and to measure the energies of tracks. It is composed of 7800 thallium-doped cesium iodide scintillating crystals, 6144 in the barrel region and 828 in each endcap, covering 95% of the solid angle. Each crystal is 30 cm long and 5 $\times$ 5 cm^2 in cross section.

When a photon or a charged particle interacts with the atoms in the crystal, an electromagnetic "shower" is emitted by crystals, and it is recorded by 4 Si photodiodes at the back of each crystal. The device allows detection of photons with energy of 30 MeV/c^2 to 5.3 GeV/c^2 with excellent resolution.

Photon energy resolution in the barrel (endcap) is 1.5% (2.6%) at 5 GeV/c^2, and 3.8% (5.0%) at 100 MeV/c^2. The angular resolution in azimuth is 3 mrad (9 mrad) at 5 GeV/c^2 and 11 mrad (19 mrad) at 100 MeV/c^2.

A typical π^0 (from the decay) finding efficiency is about 50%, and the width of the reconstructed π^0 peak is roughly 5 - 10 MeV/c^2.

CHAPTER 3
Λ_c^+ RECONSTRUCTION

3.1 Introduction

In order to study the charmed baryons which decay to Λ_c^+'s, we first need to obtain Λ_c^+ candidates, then add additional pions (one or two in our study) to reconstruct heavier charmed baryons.

Fifteen hadron decay modes were used to reconstruct Λ_c^+ candidates. They are $\mathrm{pK}^-\pi^+$, $\mathrm{pK}^-\pi^+\pi^0$, $\mathrm{p}\overline{\mathrm{K}}^0$, $\mathrm{p}\overline{\mathrm{K}}^0\pi^0\pi^0$, $\mathrm{p}\overline{\mathrm{K}}^0\pi^0$, $\Lambda\pi^+$, $\Lambda\pi^+\pi^+\pi^-$, $\Lambda\pi^+\pi^0$, $\Lambda\mathrm{K}^+\overline{\mathrm{K}}^0$, $\Sigma^+\pi^+\pi^-$, $\Sigma^+\pi^0$, $\Sigma^+\mathrm{K}^+\mathrm{K}^-$, $\Sigma^0\pi^+$, $\Xi^-\mathrm{K}^+\pi^+$, and $\Xi^0\mathrm{K}^+$. All these decay modes have good signal-to-noise ratios and reasonable statistics. The decay $\mathrm{pK}^-\pi^+$ has a very large branching fraction and contributes almost half of all Λ_c^+ candidates. It important to check the consistency of measurements by comparing the results obtained by using the $\mathrm{pK}^-\pi^+$ mode with those obtained from other modes.

3.2 Data and Monte Carlo Sample

CLEO data are taken on and off the $\Upsilon(4S)$ resonance. The beam energy is 5.187 to 5.280 GeV/c^2 for off-resonance and 5.285 to 5.295 GeV/c^2 for on-resonance. We performed our analysis using both on-resonance and off-resonance events in datasets 4S1-4SG,* corresponding to a luminosity of 4.8 fb^{-1}.

All Monte Carlo events generated were with the Λ_c^+ mass 2286.7 MeV/c^2, which is our measured mean value over all the 15 decay modes. In order to optimize

*Each time CESR or CLEO is updated, the data are processed differently, and they become a new dataset. Conventionally, CLEO datasets are named 4S1, 4S2, ..., 4S9, 4SA, 4SB, ..., and so on. "4S" indicates the state $\Upsilon(4S)$.

Table 3.1: Monte Carlo (MC) generated branching fractions for Λ_{c1}^+ and $\Sigma_c^{(*)}$ studies.

Decay mode	Average $\mathcal{B}/\mathcal{B}(\mathrm{pK}^-\pi^+)$	MC generated branching ratio
$\mathrm{pK}^-\pi^+$	1	0.158
$\mathrm{pK}^-\pi^+\pi^0$	0.67±0.04±0.11	0.106
$\mathrm{p}\overline{\mathrm{K}}^0$	0.46±0.02±0.04	0.073
$\mathrm{p}\overline{\mathrm{K}}^0\pi^+\pi^-$	0.52±0.04±0.05	0.082
$\mathrm{p}\overline{\mathrm{K}}^0\pi^0$	0.66±0.05±0.07	0.104
$\Lambda\pi^+$	0.18±0.03	0.028
$\Lambda\pi^+\pi^+\pi^-$	0.66±0.10	0.104
$\Lambda\pi^+\pi^0$	0.73±0.09±0.16	0.115
$\Lambda\mathrm{K}^+\overline{\mathrm{K}}^0$	0.12±0.02±0.02	0.019
$\Sigma^+\pi^+\pi^-$	0.68±0.09	0.107
$\Sigma^+\pi^0$	0.20±0.03	0.032
$\Sigma^+\mathrm{K}^+\mathrm{K}^-$	0.07±0.01±0.01	0.011
$\Sigma^0\pi^+$	0.20±0.04	0.032
$\Xi^-\mathrm{K}^+\pi^+$	0.10±0.02	0.016
$\Xi^0\mathrm{K}^+$	0.08±0.01±0.01	0.013
All		1

the cuts* used to reconstruct each decay mode, 15 individual types of events are generated by sufficient amounts (more than 100,000 events for each mode). In our later study on the Λ_{c1}^+ or the $\Sigma_c^{(*)}$ decaying to the Λ_c^+, we need the Monte Carlo to provide the correct over-all efficiencies. Thus the decay ratios of Λ_c^+ decay modes were generated as shown in Table 3.1. In the table, the average relative branching ratios for $\mathrm{pK}^-\pi^+\pi^0$, $\mathrm{p}\overline{\mathrm{K}}^0$, $\mathrm{p}\overline{\mathrm{K}}^0\pi^+\pi^-$, and $\mathrm{p}\overline{\mathrm{K}}^0\pi^0$ are the values recently measured by CLEO[23]. For other modes we used the PDG average values[1].

*A cut is an action to remove a certain fraction of the events which contribute mostly to the background. An optimized cut on a measured physical quantity is the one which gives the best signal-to-noise ratio after it is applied.

3.3 Event Selection

3.3.1 Track Selection

When a charged particle travels through the tracking chambers, a set of hits, caused by the passage of the track, is generated. The tracking program will fit each set of hits forming a "track," which is a curve representing a possible particle causing the hits. In CLEO, this task is accomplished by the track-finding and fitting program, DUET.

Each track is described by the following five track parameters: (1) `CUCD`: curvature of the track; (2) `FICD`: ϕ of the direction of the track at point of closest approach to the center of the CLEO-II detector; (3) `DACD`: impact parameter of track with respect to the center of the detector; (4) `CTCD`: cotangent of the polar angle, θ (i.e. $\texttt{CTCD} = 0$ for tracks in the $r - \phi$ plane and infinite for tracks pointing down the beam pipe;) (5) `ZOCD`: z coordinate at point of closest approach to the center of the detector. All other information about the track can be calculated from these five parameters.

Before 1996, the track fitter in the CLEO DUET processor ignored the energy loss of a track in materials and included multiple scattering approximately. In 1996, the CLEO collaboration reprocessed the data from 4S1 to 4SG, and the new data are called the recompressed data. For the recompressed data, the old track fitter is replaced by a Kalman Filter. The new Kalman fitter optimally treats both multiple scattering and energy loss, so it gives improved error matrices of track parameters for all tracks and better-measured track parameters for low-momentum tracks. It also fits each track separately for each particle hypothesis.

To select a track as a candidate for a pion, a kaon, or a proton, which come from the $r - \phi$ range of e^+e^- interaction points, we first require it to have not only $r - \phi$

also z information. We reject all tracks which are identified inward going. To ensure these tracks are close to the interaction point, we used the following "track quality" cuts:

$$|\texttt{DBCD}| < \begin{cases} 5 - 3.8|P| \text{ (mm)} & \text{if } |P| < 1, \\ 1.2 \text{ mm} & \text{if } |P| \geq 1, \end{cases}$$

where DBCD is the radial distance of the point of closest approach to the beam line, P is the momentum of the charged track; and

$$|\texttt{ZOCD}| < 5 \text{ cm}.$$

Note that the DBCD cut changes from 5 mm at 0 momentum to 1.2 mm at 1 GeV/c and then becomes flat from 1.2 mm. This is because the low-momentum tracks are more poorly measured, but we still want to keep those having fairly good quality.

Such selected tracks are used as the charged track candidates which are directly decayed from Λ_c^+'s. The Λ_c^+ has a mean lifetime of about $2 \times 10^{-13}s$, so its flight distance in the CLEO detector is within the range of interaction points and is negligible in the invariant mass reconstruction.

3.3.2 Particle Identification

As we discussed in the last chapter, two types of detectors are used for the identification of the charged tracks: the time-of-flight counters and the drift chamber for the dE/dx measurement. The information from each device, if present, is quoted as the number of standard deviations of the measurement from the expected value as a given particle hypothesis. For each charged track, we combine the TOF and the dE/dx information to define a joint

$$\chi_i^2 = \Big[\frac{(dE/dx)_{meas} - (dE/dx)_{exp}}{\sigma_{dE/dx}}\Big]^2 + \Big[\frac{(TOF)_{meas} - (TOF)_{exp}}{\sigma_{TOF}}\Big]^2,$$

where i stands for pion, kaon, and proton hypothesis.

The χ^2 ranges from zero to infinity and it is not very convenient to use when we perform a track identification cut. So, a equivalent parameter, the χ^2 probability, PROB, is calculated for each hypothesis. PROB ranges from zero to one.* For data analysis, it has the advantage of being flat in the zero to one range for particles which are the right species and peaking at zero for particles which are the wrong species.

One particle identification information will be used if the other device does not have the measurement. If neither TOF nor dE/dx information is present, we assume the track is a pion and assign it a small $\texttt{PROB}(\pi)$ value.

In this work, we are more concerned about separating protons, kaons and pions from each other, so a normalized probability, called "PROB level," is used. To strongly identify a proton or a kaon, we make a cut on

$$\texttt{PRLEV} = \frac{\texttt{PROB}(p)}{\texttt{PROB}(p) + \texttt{PROB}(K) + \texttt{PROB}(\pi)}$$

or,

$$\texttt{KALEV} = \frac{\texttt{PROB}(K)}{\texttt{PROB}(p) + \texttt{PROB}(K) + \texttt{PROB}(\pi)}.$$

We do not use a PROB level cut for pions, since we take all the tracks selected as pion candidates.

3.3.3 γ and π^0 Finding

Although the CsI electromagnetic calorimeters can measure the photon energy and angle, they also interact with hadrons. An electromagnetic shower generally has different lateral development than a hadronic shower. This provides us a way

*Note it does not really represent the probability of the track to be a specific particle hypothesis.

to distinguish them from each other. The quantity $E9/E25$ is measured as

$$E9/E25 = \frac{\text{Energy of 9 central crystals}}{\text{Energy of 25 central crystals}}.$$

Here the 9 crystals in the numerator are those in a 3×3 array, with the most energetic crystal at the center. The 25 crystals in the denominator are those in a 5×5 array. Since electromagnetic showers tend to be more narrowly contained than hadronic showers, they mostly have $E9/E25$ near 1. The most widely used cut on $E9/E25$ quantity in CLEO is to keep 99% photons* and get rid of most of the hadronic showers. A $E9/E25$ cut also gets rid of two photons which are close together. Also, as the high energy showers near to each other often deposit energy to the same crystals, we can use a program to "unfold" the nearby shower clusters. The unfolding routine works well to identify high energy photons but become less efficient when photon energy is low. When we select a photon in this analysis, we mostly use unfolded $E9/E25$ at 99% (this cut is called 99% `E9E25U`), and sometimes directly use $E9/E25$ at 99% (not unfolded, called 99% `E9OE25`) when we are certain that the photon energy spectrum is low.

π^0's are formed by taking two photon combinations and calculating the di-photon invariant mass. The di-photon combination must have at least one photon in the barrel region of the crystal calorimeters.

Unless otherwise stated, we always selected π^0 candidates as just described. In addition, we require the mass of each candidate to be within 2.5 $\sigma_{M_{\pi^0}}$ of the known π^0 mass, which is 134.976 MeV/c^2. However, to suppress combinational background, we will place cuts on π^0 momenta in different situations.

*This cut value is actually obtained by a program which returns $E9/E25$ cuts for 1% efficiency loss in a given region of the detector. The 1% is nominal only from MC, and it is a loss in an event with no other showers. Actual efficiency losses are substantially more, e.g., 5-10% efficiency loss for photons in hadronic events from a 1% cut. Harsh cuts, like 5% or 10%, lose too many photon candidates, so they are not often used.

3.3.4 Event Vertex Finding

Finding the event vertex, which is the e^+e^- interaction point, can be very useful to improve the mass resolution of a reconstructed particle. Most of the charged tracks come from the event vertex or vertices extremely close to the event vertex, so we can obtain the event vertex with errors by performing a vertex fit using charged tracks. However, some tracks are not from anywhere close to the event vertex, and some tracks are not measured correctly. Using these tracks will increase the uncertainty of the event vertex. Therefore, to find the event vertex, we start with the two tracks which are the most consistent with the beam position and also not close to back to back, form a vertex, then add more tracks one by one in the order of their consistencies with the current found vertex, until further adding any track would make a poorer vertex fit. If the error of the final found vertex is not small enough to confine itself within the spread of the beam position, or if we do not have more than one charged track, the beam position will be used as the event vertex.

3.3.5 Vee Finding

A large fraction of Λ_c^+'s decay to $\overline{K^0}$'s or Λ's. In CLEO, the $\overline{K^0}$ is reconstructed by the decay $K_S \to \pi^+\pi^-$* and the Λ is reconstructed by its decay to $p\pi^-$. K_S's and Λ's mostly fly a few centimeters away before they decay. The K_S has $c\tau = 2.7$ cm and the Λ has $c\tau = 7.9$ cm. Since in each case the shape of the two daughters' paths looks like the letter V, they are generally called Vees. The vertex of a Vee formed by the two charged tracks is called a secondary vertex, in distinction to the primary vertex, the event vertex.

To find Vee candidates, we first list the tracks which satisfy —`DBCD/DDBCD` > 3— (`DDBCD` is the estimated uncertainty of `DBCD`) to exclude the tracks coming from the

*$\overline{K^0}$ appears in the states of K_S (50%) or K_L (50%). CLEO detector cannot detect the K_L since it travels many meters long ($c\tau = 15.5$ m).

primary vertex. The tracks in the list, called the secondary tracks, are all possible daughters of Vees. Then we take every pair of tracks from the list and fit them to form a vertex. We discard the pair if the fit is very poor ($\chi^2 < 0.001$) or if the significance of the three-dimensional flight distance is smaller than 3σ. We require the total number of hits inside the found vertex for both daughters to be smaller than 2. Also, the reconstructed mass of a Vee should be within 3 σ_M of the known K_S or Λ mass. Note that the Kalman Filter only calculates the track parameters of the secondary tracks from the origin. We corrected these track parameters at the secondary vertex, then further recalculated the momentum and the position of the Vees. Details of the CLEO secondary vertex finding program are described by Prescott[24].

In this analysis, we made a few more cuts on Vee candidates to make the signal clearer with a tiny sacrifice of losing events: a Vee is required to come from the range of the beam position; the separation in z of the two daughters at the $r-\phi$ intersection should not be large (the significance is required to be smaller than 5); for a K_S candidate, each daughter must satisfy $\texttt{PROB}(\pi) > 0.001$; for a Λ candidate, the daughter which carries most of the momentum in the decay in the laboratory frame (according to special relativity, this almost guarantees that it is the proton if its parent is really a Λ) must satisfy $\texttt{PROB}(p) > 0.001$.

3.3.6 Σ and Ξ Finding

The decays of the four Σ and Ξ are shown in Figure 3.1. Because these particles are supposed to be the decay products from the Λ_c^+, which has very short lifetime, it is very reasonable to assume that they all come from the event vertex.

Σ^+ candidates are reconstructed through the decay $\Sigma^+ \to p\pi^0$. The π^0 selection is described in Section 3.3.3. All charged tracks are taken as proton candidates.

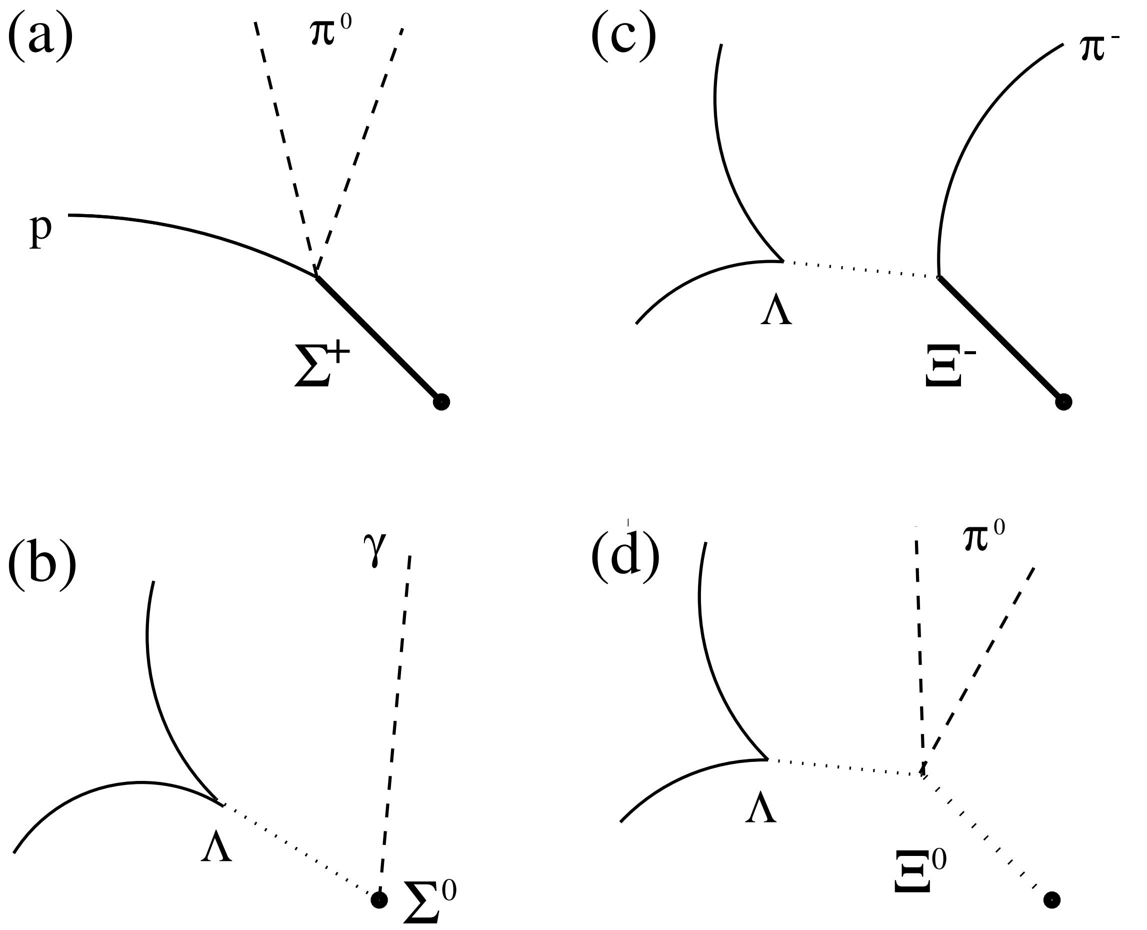

Figure 3.1: Decay paths of (a) $\Sigma^+ \to p\pi^0$ and $\pi^0 \to \gamma\gamma$, (b) $\Sigma^0 \to \Lambda\gamma$ and $\Lambda \to p\pi^-$, (c)$\Xi^- \to \Lambda\pi^-$ and $\Lambda \to p\pi^-$, and (d) $\Xi^0 \to \Lambda\pi^0$, $\Lambda \to p\pi^-$, and $\pi^0 \to \gamma\gamma$. In each figure, the solid curves indicate paths of charged particles; the dashed lines indicate paths of photons; and the dotted lines indicate paths of neutral hyperons. All Σ and Ξ are assumed to be created at the event vertex, which is shown as $\bullet$. The Σ^+, Ξ^-, Ξ^0, and Λ travel for a distance before decay. The Σ^0 and π^0 decay immediately after being created.

A particle identification cut PRLEV > 0.5 is used. After adding the 4-momenta of the proton and the π^0, the flight distance of Σ^+ can be calculated by constraining the Σ^+ coming from the event vertex, and, further, the Σ^+ decay vertex can be obtained. Since the Σ^+ has a long lifetime ($c\tau = 2.4$ cm), we require the transverse flight distance of the Σ^+ to be bigger than 5 mm and DBCD of the proton to be bigger than 0.5 mm. In addition, to reduce the combinational background, we make a momentum cut of 300 MeV/c^2 for the π^0 and 500 MeV/c^2 for the proton. We require the mass of each Σ^+ candidate to be 20 MeV/c^2 within the known Σ^+ mass, 1189.4 MeV/c^2.

Σ^0 candidates are reconstructed through the decay $\Sigma^0 \to \Lambda\gamma$, where selections of the Λ and γ are described in the previous sections. A 50 MeV/c^2 photon energy cut is used to reduced the background. We require the mass of each Σ^0 candidate to be 20 MeV/c^2 within the known Σ^0 mass, 1192.6 MeV/c^2.

Ξ^- candidates are reconstructed through the decay $\Xi^- \to \Lambda\pi^-$. All negative-charge tracks are used to be the π^- candidates. The Ξ^- has $c\tau = 4.9$ cm so its decay vertex should be distinctly displaced from the event vertex. The initial guess of the Ξ^- vertex is at the intersection of the projected Λ path and the π^- track. The combination is discarded if the vertex cannot be reasonably formed or the combined direction does not point back to the event vertex. The invariant mass of $\Lambda\pi^-$ is required to be within 6 MeV/c^2 of the known Ξ^- mass, which is 1197.4 MeV/c^2. Then the track parameters of the Λ and the π^- are recalculated at the new vertex by constraining the $\Lambda\pi^-$ invariant mass to be 1197.4 MeV/c^2. The Ξ^- momentum and vertex are further obtained more accurately. The Ξ^- flight distance is required to be larger than 5 mm, and its $r - \phi$ radial distance is required to be larger than 1 mm.

Ξ^0 candidates are reconstructed by a $\Xi^0 \to \Lambda\pi^0$. We initially build the Ξ^0 vertex, then combine the π^0 angle with the projected Λ path. The combined direction is required to point back to the event vertex. We correct the π^0 4-momentum by constraining it to come from the Ξ^0 vertex. Then the Ξ^0 4-momentum is recalculated. The reconstructed Ξ^0 mass is required to be within 8 MeV/c^2 of the known Ξ^0 mass, which is 1315 MeV/c^2. The $r-\phi$ radial distance of the Ξ^0 vertex from the event vertex has to be larger than 5 mm. A 100 MeV/c^2 π^0 momentum cut is used.

3.4 Λ_c^+ Selection

A Λ_c^+ is reconstructed by calculating its 4-momentum and decay vertex from the momentum, mass assumption, and vertex information of its direct daughters. The Λ_c^+ signal can be measured by fitting its reconstructed mass spectrum using Mn_Fit.[25]* Mn_Fit is an interactive plotting and fitting package that uses MINUIT[26] to fit histograms or data read in from a file and to display the fitting results. It is widely used by high energy experimental groups to perform data analysis.

Although the purpose of reconstructing the Λ_c^+ baryons is to observe the Λ_{c1}^+ and the Σ_c which decay to the Λ_c^+, our Λ_c^+ candidates are not selected by direct optimizing the Λ_{c1}^+ or $\Sigma_c^{(*)}$ signals. The Λ_{c1}^+ or Σ_c signals should not be biased by Λ_c^+ selection. In general, for each Λ_c^+ decay mode we try to use cuts to get the best signal-to-background ratio at $x_p > 0.5$. x_p is the Λ_c^+ momentum normalized to the maximum possible Λ_c^+ momentum, defined as

$$x_p = \frac{p_{\Lambda_c^+}}{\sqrt{E^2 - M_{\Lambda_c^+}^2}},$$

where E is the energy of the $e^+(e^-)$ beam of CESR. Note that $x_p > 0.5$ is only used to optimize the Λ_c^+ selection cuts, and not for Λ_c^+ selection. The momentum

*In this dissertation, all histograms, fitted curves and direct statistical results are obtained from Mn_Fit.

spectra of charmed hadrons from the e^+e^- annihilation have been shown to be hard compared to the combinational background. Therefore a cut on x_p is a very good way to improve the signal-to-background ratio. For most of the decay modes, the $x_p > 0.5$ cut makes the signal be roughly same large as the background. Later, when we look at Λ_{c1}^+ or $\Sigma_c^{(*)}$ signals, we make x_p cuts on these heavier baryons, and there will be no cut on the x_p of the Λ_c^+.

Since a Λ_c^+ travels at a distance of the order of 100 μm before it decays, its vertex can be slightly displaced from the event vertex. We find that constraining all direct Λ_c^+ daughters (except π^0's which do not have position information) to come from an unknown vertex significantly improves the mass resolution of the Λ_c^+. Thus for each of the 15 decay modes, the Λ_c^+ candidate is built at its vertex.

For the decay modes containing a proton, strong particle identification cuts are needed. Since the proton momentum spectrum are different for different decay modes (generally higher for two-body decays and lower for three-body and four-body decays), the cut value on `PRLEV` does not correspond to the same efficiency for the different modes of background rejection. The numbers we used — 0.3 for $\mathrm{p\overline{K}^0}$, 0.6 for $\mathrm{pK^-\pi^+}$, and 0.8 for $\mathrm{pK^-\pi^+\pi^0}$, $\mathrm{p\overline{K}^0\pi^0\pi^0}$, and $\mathrm{p\overline{K}^0\pi^0}$— have roughly the same efficiencies. For the two modes containing a proton and a $\mathrm{K^-}$, the identification cuts are relatively softer since the proton is already strongly identified. Since the signals of $\Sigma^+\mathrm{K^+K^-}$, $\Xi^-\mathrm{K^+}\pi^+$, and $\Xi^0\mathrm{K^+}$are already very clean, very soft `PROB`(K) cuts are used to keep the highest efficiencies. To suppress combinational background, Monte Carlo optimized momentum cuts on charged tracks or π^0's are used. For charged particles, we generally cut at high values for two-body decays and lower values for multi-body decays. All decay modes containing a π^0 have very high backgrounds, so we always need restrictive cuts on π^0 momenta.

Table 3.2: Particle Identification and Momentum cuts used in the 15 decay modes for the Λ_c^+ selection. The values of physical parameters in the table are required to be larger than the corresponding numbers listed. The momenta $P_{K^\pm}$, $P_{\pi^\pm}$, and P_{π^0} are in units of MeV/c.

Decay	PRLEV	KALEV	PROB(K)	$P_{K^\pm}$	$P_{\pi^\pm}$	P_{π^0}
$\mathrm{pK}^-\pi^+$	0.6	0.2			100	
$\mathrm{pK}^-\pi^+\pi^0$	0.8	0.5			200	500
$\mathrm{p\overline{K}}^0$	0.3					
$\mathrm{p\overline{K}}^0\pi^+\pi^-$	0.8				500	
$\mathrm{p\overline{K}}^0\pi^0$	0.8					500
$\Lambda\pi^+$					300	
$\Lambda\pi^+\pi^+\pi^-$					200	
$\Lambda\pi^+\pi^0$					300	500
$\Lambda\mathrm{K}^+\mathrm{\overline{K}}^0$		0.3				
$\Sigma^+\pi^+\pi^-$					100	
$\Sigma^+\pi^0$						300
$\Sigma^+\mathrm{K}^+\mathrm{K}^-$			0.02		100	
$\Sigma^0\pi^+$					400	
$\Xi^-\mathrm{K}^+\pi^+$			0.01		100	
$\Xi^0\mathrm{K}^+$			0.01	300		

The cuts used to reconstruct Λ_c^+'s for each decay mode are listed in Table 3.2. Note that the vertex constraint routines are common for all modes. The selection criteria of all immediate Λ_c^+ daughters have been described in previous sections.

Figures 3.2 to 3.16 show the reconstructed mass of Λ_c^+ for the 15 idividual decay modes, and Figure 3.17 shows the sum over all modes. For the purpose of display a $x_p > 0.5$ cut is applied to the Λ_c^+ momentum.

The measurements on all 15 modes and their summation are tabulated in Table 3.3. All parameters are obtained by fitting the signal with a single Gaussian. The Gaussian width of each decay mode reflects the detector resolution of the Λ_c^+ mass. The table shows that the fitted widths agree very well with those of the Monte Carlo, except some modes with a π^0 and "All." For the modes with a π^0, we found that the widths are all wide and the signals could not be fitted well by a single Gaussian.

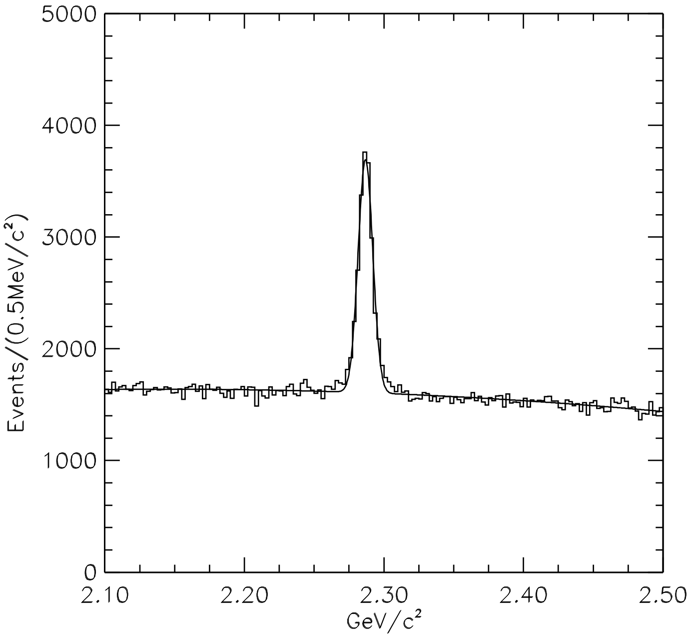

Figure 3.2: Invariant mass of $pK^-\pi^+$.

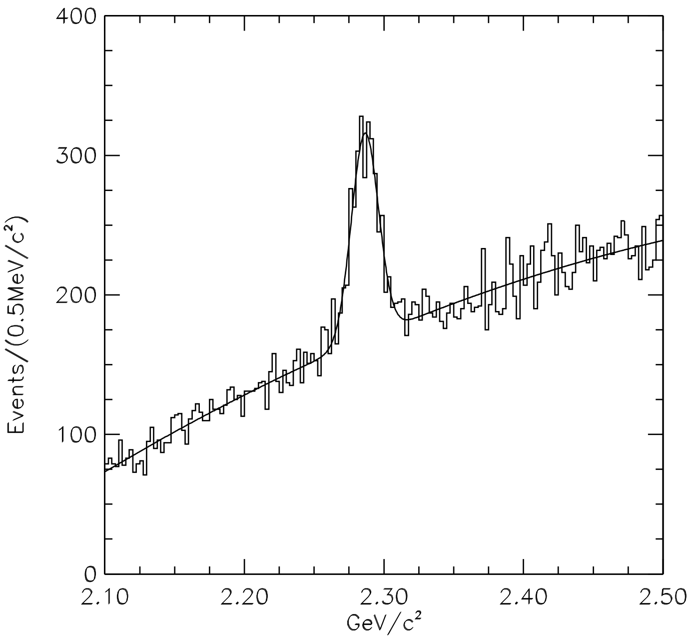

Figure 3.3: Invariant mass of $pK^-\pi^+\pi^0$.

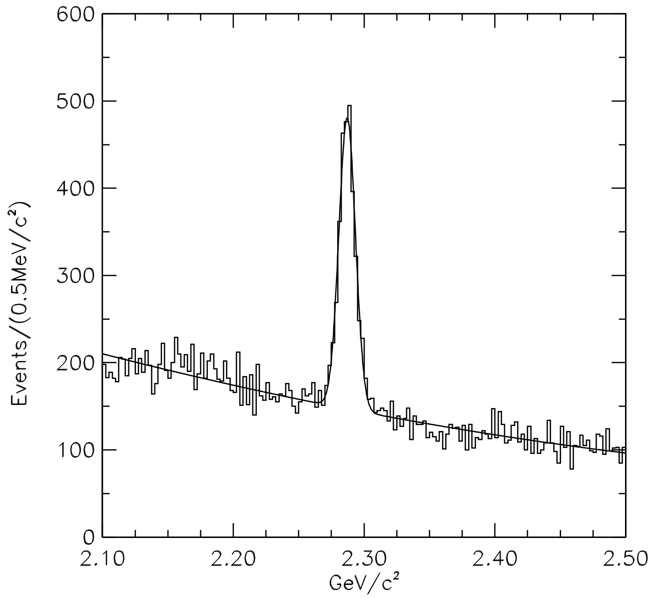

Figure 3.4: Invariant mass of $p\overline{K}^0$.

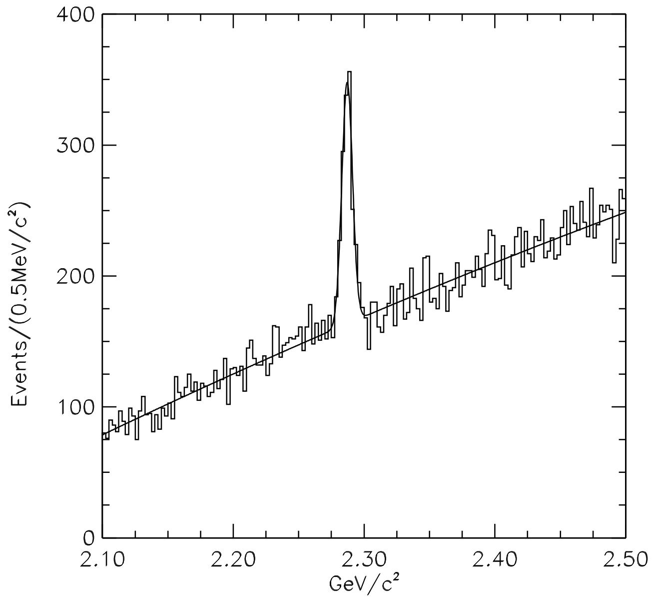

Figure 3.5: Invariant mass of $p\overline{K}^0\pi^0\pi^0$.

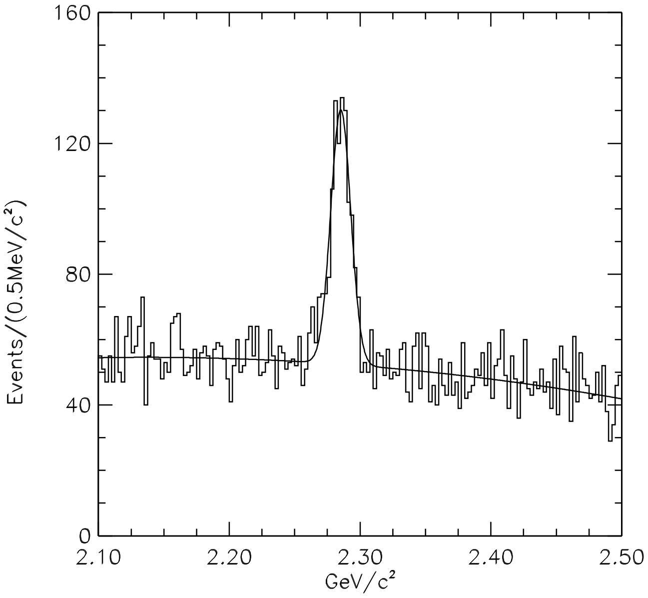

Figure 3.6: Invariant mass of $p\overline{K}^0\pi^0$.

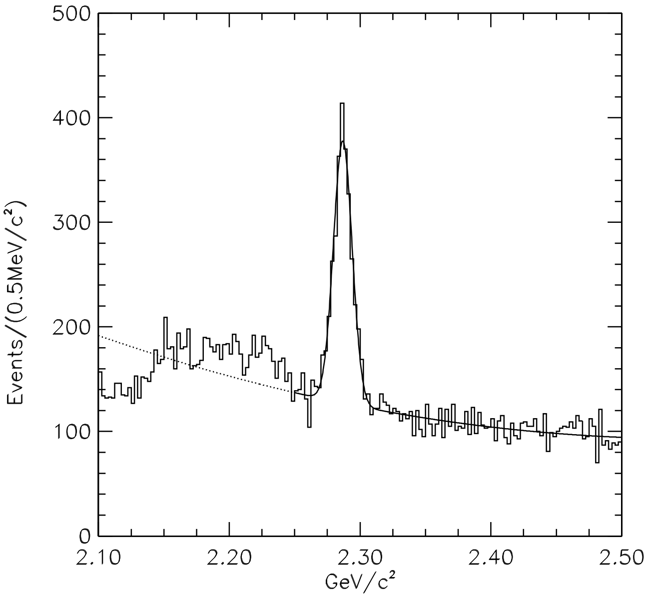

Figure 3.7: Invariant mass of $\Lambda\pi^+$.

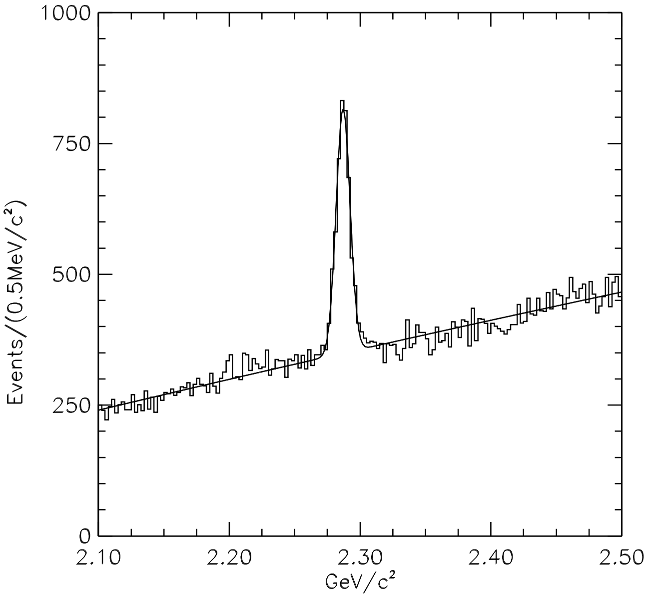

Figure 3.8: Invariant mass of $\Lambda\pi^+\pi^+\pi^-$.

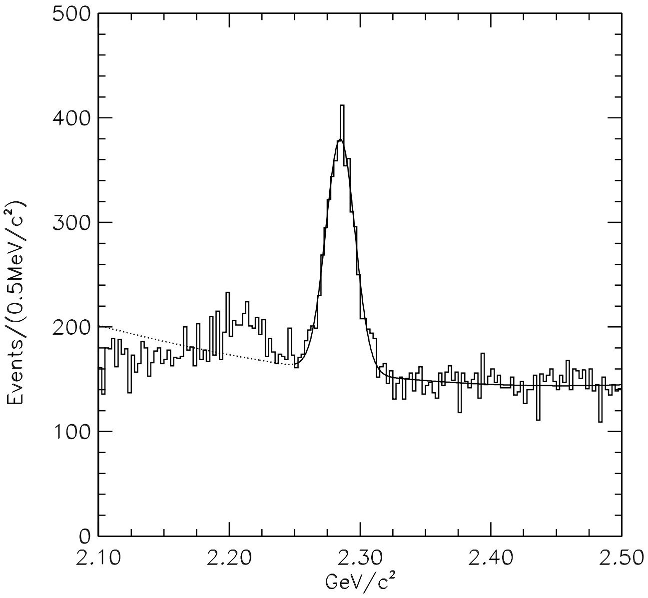

Figure 3.9: Invariant mass of $\Lambda\pi^+\pi^0$.

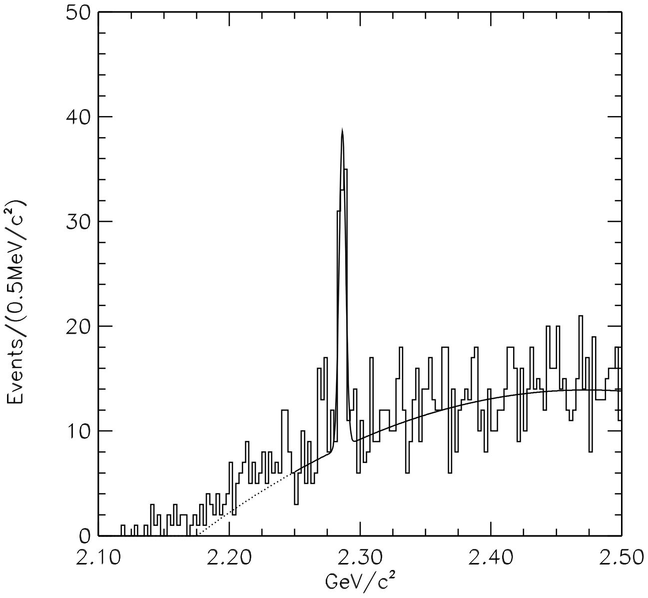

Figure 3.10: Invariant mass of $\Lambda K^+\overline{K}^0$.

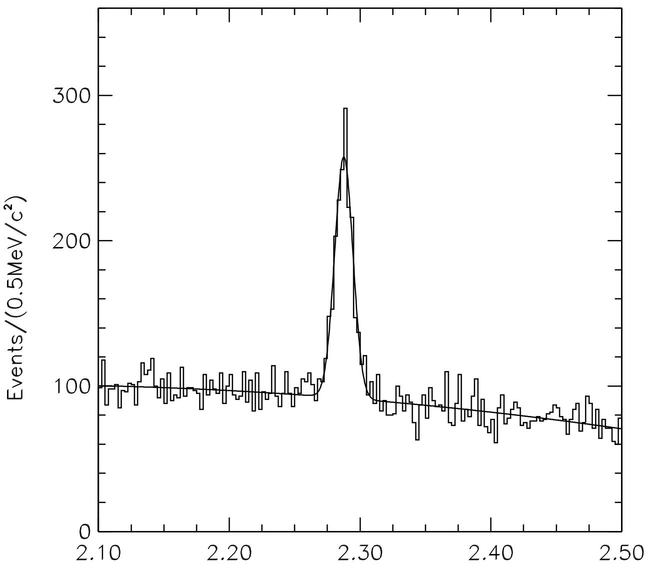

Figure 3.11: Invariant mass of $\Sigma^+\pi^+\pi^-$.

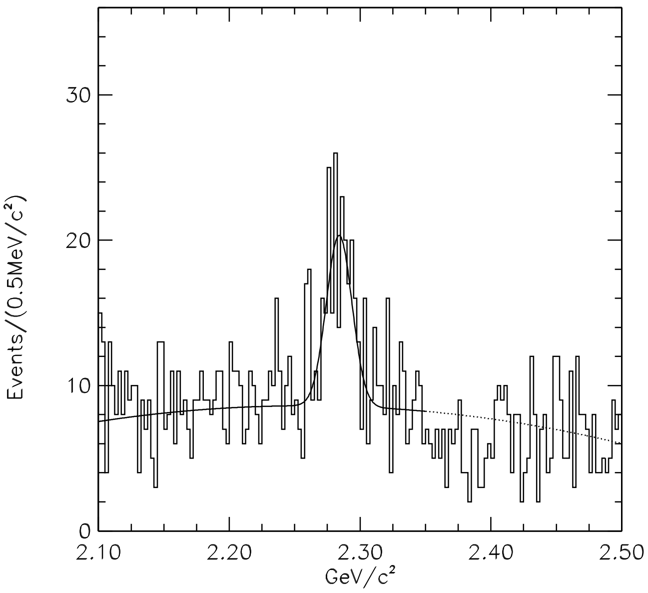

Figure 3.12: Invariant mass of $\Sigma^+\pi^0$.

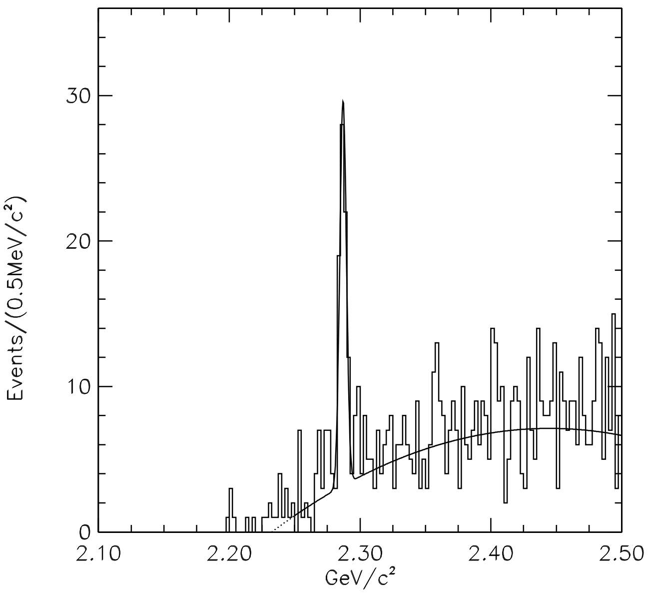

Figure 3.13: Invariant mass of $\Sigma^+K^+K^-$.

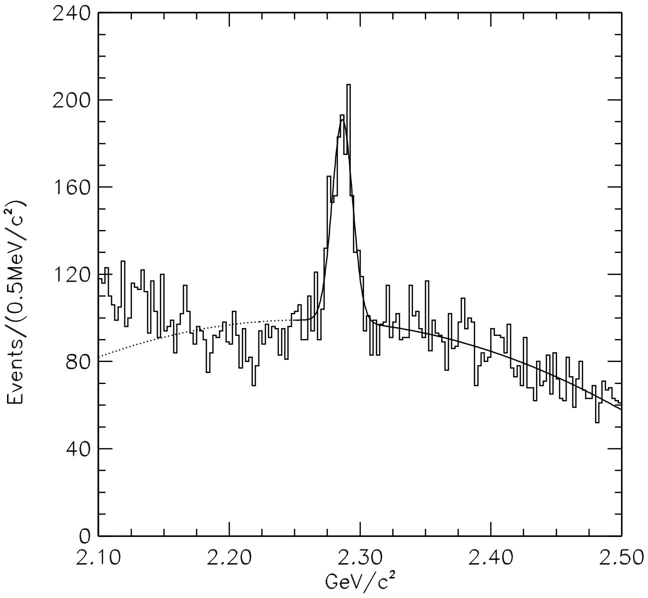

Figure 3.14: Invariant mass of $\Sigma^0\pi^+$.

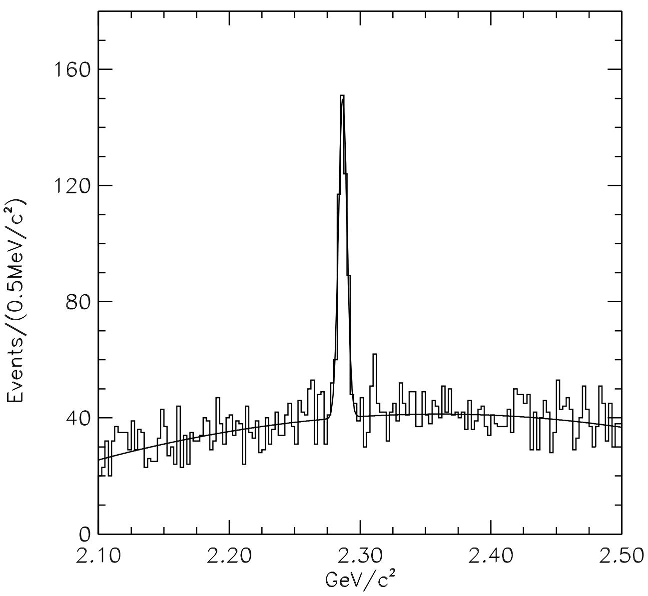

Figure 3.15: Invariant mass of $\Xi^- K^+\pi^+$.

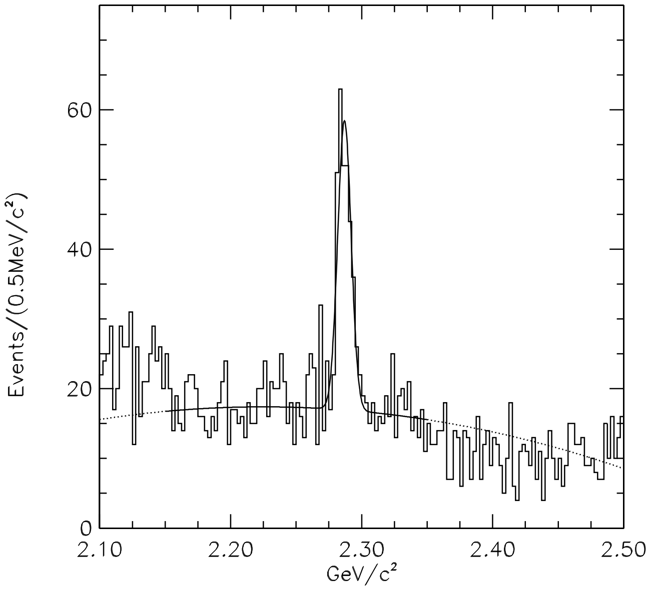

Figure 3.16: Invariant mass of $\Xi^0 K^+$.

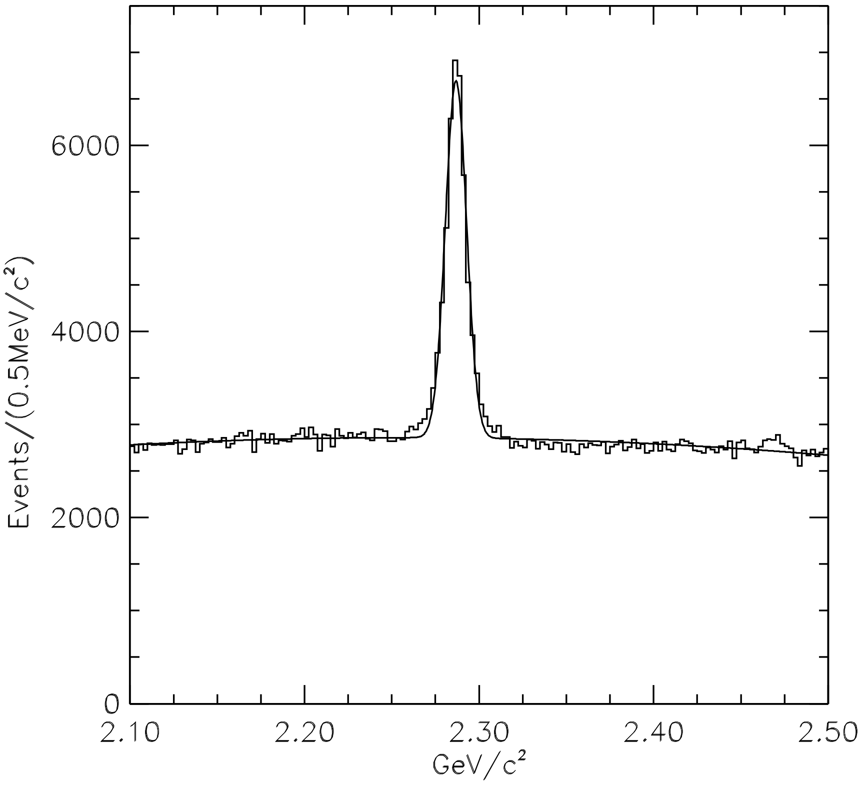

Figure 3.17: Invariant mass of Λ_c^+ candidates reconstructed by 15 decay modes. Although the distribution overlaid by 15 different Gaussians is not exactly in a Gaussian shape, we fit it by a single Gaussian to roughly check the central mass value and the signal-to-background ratio.

Table 3.3: Masses, Monte Carlo widths (σ_M(MC)), Fitted widths (σ_M(Fit)) together with the number of Λ_c^+'s found with $x_p > 0.5$. The mass for all modes is the error-weighted mean value over all modes and the same value is obtained when we fit Figure 3.17. The signal the background shown in the table are the fitted areas within $1.6\sigma_M$(Fit) around 2286.7 MeV/c^2. Masses and widths are in units of MeV/c^2. Only statistical errors are shown. The statistical errors on Monte Carlo width are all 0.01 MeV/c^2.

Decay Mode	Mass	σ_M(MC)	σ_M(Fit)	Signal	Background
$\mathrm{pK}^-\pi^+$	2286.7±0.1	5.20	5.26±0.11	9650	11660
$\mathrm{pK}^-\pi^+\pi^0$	2286.4±0.6	8.11	9.04±0.62	1252	1928
$\mathrm{p}\overline{\mathrm{K}}^0$	2287.1±0.2	6.51	6.33±0.23	1716	1019
$\mathrm{p}\overline{\mathrm{K}}^0\pi^+\pi^-$	2287.1±0.3	3.98	4.07±0.30	568	690
$\mathrm{p}\overline{\mathrm{K}}^0\pi^0$	2285.2±0.6	8.61	7.63±0.63	514	490
$\Lambda\pi^+$	2287.8±0.3	7.03	7.15±0.31	1368	658
$\Lambda\pi^+\pi^+\pi^-$	2287.0±0.2	5.28	5.37±0.21	1916	1812
$\Lambda\pi^+\pi^0$	2285.0±0.4	10.38	11.18±0.56	2007	1864
$\Lambda\mathrm{K}^+\overline{\mathrm{K}}^0$	2286.5±0.4	2.91	2.51±0.32	70	25
$\Sigma^+\pi^+\pi^-$	2287.6±0.3	7.41	6.96±0.38	947	696
$\Sigma^+\pi^0$	2284.0±1.7	10.32	9.80±0.23	95	101
$\Sigma^+\mathrm{K}^+\mathrm{K}^-$	2287.0±0.4	2.61	2.54±0.31	65	18
$\Sigma^0\pi^+$	2286.5±0.6	7.54	7.79±0.59	707	896
$\Xi^-\mathrm{K}^+\pi^+$	2286.7±0.1	3.50	3.27±0.25	317	171
$\Xi^0\mathrm{K}^+$	2286.9±0.5	6.73	6.10±0.51	221	173
All	2286.7±0.1			20675	22160

If we fit them by a double-Gaussian, the data and the Monte Carlo are in better agreement (about half way closer). Thus we can conclude that the Monte Carlo can predict the mass resolution of the Λ_c^+ very well.

Note that our measured mean value of Λ_c^+ mass, 2286.7 MeV/c^2, is slightly larger than the PDG mean value 2284.9±0.6 MeV/c^2, which is partially determined by the result of CLEO-I.5[27]. CLEO-II has measured many more decay modes with much better mass resolutions and tiny statistical errors, and has constantly shown a higher value. So in this work, we decided to use the CLEO-II value as the "known" Λ_c^+ mass. As we will show in later chapters, as we look at Λ_{c1}^+ or $\Sigma_c^{(*)}$

mass by mass differences with Λ_c^+, the error on Λ_c^+ mass contributes little to the systematic errors of our measurements. The purpose of this work does not include the Λ_c^+ mass measurement. It should be a separate research work which will require a comprehensive study of the systematic uncertainties of the mass scale.

CHAPTER 4
STUDIES OF Λ_{c1}^+ BARYONS

4.1 Introduction

Two particles have been found decaying to Λ_c^+ and two charged pions. They have been named $\Lambda_c^+(2625)$ and $\Lambda_c^+(2593)$ by the Particle Data Group[1]. The first observation of the $\Lambda_c^+(2625)$ was made by the ARGUS Collaboration[28]. The E687[29] and CLEO[30] Collaborations subsequently confirmed this charmed state. CLEO also reported the first observation of $\Lambda_c^+(2593)$, and E687[31] and ARGUS[32] published the confirmation of these states. Since hese particles were seen only in $\Lambda_c^+\pi^+\pi^-$ modes but not in $\Lambda_c^+\pi^0$ mode, they are believed to be the excited Λ_c^+ baryons rather than higher states of Σ_c baryons, which decay through both $\Lambda_c^+\pi$ and $\Lambda_c^+\pi^+\pi^-$ channels but should prefer $\Lambda_c^+\pi$ modes. Proposed by the previous experiments and strongly confirmed in this work, the two states are a fine structure doublet of the excited Λ_c^+ baryons in which the light diquark ud has an orbital angular momentum $L = 1$ with respect to the c quark, Therefore, even though they were called Λ_c^{*+} in previous experimental publications just referred above, we prefer to call them the $\Lambda_{c1}^+(2593)$ and $\Lambda_{c1}^+(2625)$,* where subscript 1 refers to the total spin of the light degrees of freedom.

The $\Lambda_{c1}^+(2593)$ decays largely, and perhaps entirely, into $\Sigma_c\pi$. As explained in Chapter 1, this is the expected dominant decay channel. The quark model predicts that Σ_c has $J^P = 1/2^+$, so almost certainly the $\Lambda_{c1}^+(2593)$ has $J^P = 1/2^-$. The

*They are called $\Lambda_{c1}^+(1/2)$ and $\Lambda_{c1}^+(3/2)$ in Chapter 1 in order to conviently distinguish the spin difference. But the general convention to name a excited state particle is to used the particle name followed by its first observed mass.

J^P of the $\Lambda_{c1}^+(2625)$ is expected to be $3/2^-$. The $\Lambda_{c1}^+(2593)$ and the $\Lambda_{c1}^+(2625)$ are presumably the charm counterparts of the strange particles the $\Lambda(1405)$ and the $\Lambda(1520)$.

Since the last publication of these states in 1995, the CLEO-II detector has collected 60% more data, and the recompress made in 1996 significantly improved the resolution of low-momentum tracks, which is very important in order to observe $\Lambda_{c1}^+ \rightarrow \Lambda_c^+ \pi^+ \pi^-$ decays. We think it is time to confirm or update our previous results and look for a new decay channel, $\Lambda_c^+ \pi^0 \pi^0$.

In this chapter, we first describe Monte Carlo simulation of Λ_{c1}^+ decays. This is followed by the observations of $\Lambda_c^+ \pi^+ \pi^-$ and $\Lambda_c^+ \pi^0 \pi^0$ signals. Then we present our measurements on $\Sigma_c \pi$ decay substructures and the search for the decays of $\Lambda_c^+ \pi^0$ and $\Lambda_c^+ \gamma$. In later sections, we report the results on masses, widths, fragmentation functions, branching ratios, production ratios, together with a detailed discussion on estimating systematic errors. We also compare our results with theoretical predictions.

4.2 Monte Carlo Studies

In order to determine the detector resolution of signals and estimate the reconstruction efficiencies, large amounts (more than 100,000 events for each decay mode) of Monte Carlo events were generated. Therefore, statistical errors on all quantities directly derived from Monte Carlo can always be neglected in the numerical calculations.

The $\Lambda_{c1}^+(2593)$ events are first generated with a mass of 2593.9 MeV/c^2 and zero width to obtain the mass resolution of the detector. After a preliminary measurement of the natural width using the real data, more $\Lambda_{c1}^+(2593)$ events with the measured natural widths were generated. We found that our invariant mass reconstruction program can extract the Monte Carlo generated natural width very well, and efficiencies calculated from 0 width events and events with a finite width are very close.

The $\Lambda_{c1}^+(2625)$ events are generated with a mass of 2626.6 MeV/c^2 and zero width.

To study the substructure of Λ_{c1}^+ decays, we generated samples with both $\Sigma_c\pi$ and non-resonance decay modes. The non-resonance modes are simply the decays $\Lambda_{c1}^+ \to \Lambda_c^+\pi\pi$ and $\Lambda_{c1}^+ \to \Lambda_c^+\pi^0\pi^0$. The $\Sigma_c\pi$ modes are (1) the mixed 50% $\Lambda_{c1}^+ \to \Sigma_c^{++}\pi^-$ and 50% $\Lambda_{c1}^+ \to \Sigma_c^0\pi^+$, with $\Sigma_c^{++} \to \Lambda_c^+\pi^+$ and $\Sigma_c^0 \to \Lambda_c^+\pi^-$, and (2) the $\Lambda_{c1}^+ \to \Sigma_c^+\pi^0$ with $\Sigma_c^+ \to \Lambda_c^+\pi^0$. The$\Lambda_{c1}^+ \to \Sigma_c\pi$ and $\Lambda_{c1}^+ \to \Lambda_c^+\pi\pi$ modes are used for the $\Lambda_{c1}^+(2593)$ and the $\Lambda_{c1}^+(2625)$, respectively, to evaluate the corresponding efficiencies and resolutions, as the data show us that these are the dominating decay modes.

Determination of the detector resolution by the Monte Carlo is very crucial for extracting the intrinsic width of a particle when its intrinsic width is close or smaller than the resolution. As stated in the last chapter, we have checked for all 16 Λ_c^+ decay modes, and the Monte Carlo predicted widths are all in good agreement with the fitted widths of the data signal. However, the charged daughters of Λ_c^+'s are all at quite high momentum ranges, but the two independent pions in $\Lambda_{c1}^+ \to \Lambda_c^+\pi\pi$ decays are both soft. It is possible that the CLEO-II official Monte Carlo program overestimates the performance of the detectors on measurements of low-momentum-track parameters. This can make the Monte Carlo predicted resolutions smaller than actual resolutions of $\Lambda_{c1}^+ \to \Lambda_c^+\pi\pi$ signals.

Measuring the signal of the D^{*+}, which has $\Gamma < 0.13$ MeV/c^2 at 90% confidence level[1], can be used to check the accuracy of the resolution of the low-momentum pions by the Monte Carlo. To do this, we looked at the mass difference $M(D^{*+}) - M(D^0)$ of decay $D^{*+} \to D^0\pi^+$ (and $D^0 \to K^-\pi^+$) in which the momentum spectrum of the independent pion is close to those of the two independent pions from Λ_{c1}^+

decays. The fitted width of the signal of $M(D^{*+}) - M(D^0)$ distribution is (0.550 $\pm$ 0.001) MeV/c^2 for the Monte Carlo, but about 0.63 MeV/c^2 for the real data in the worst case,* about 15% larger. We think the actual detector resolution is in the 0 - 15% range larger than the Monte Carlo predicted one. The D^{*+} width is largely affected by the angular resolution of the soft pion. This is not the case for Λ_{c1}^+ widths based on our study of comparing the Monte Carlo widths with the data at different decay angle. So the amount of the disagreement between real data and the Monte Carlo for D^{*+} may not reflect the same amount of the disagreement for Λ_{c1}^+ widths. But it appears that the Monte Carlo prediction of the resolution is too optimistic. This was not noticeable in the previous research in CLEO since the mass resolution itself was poor. For the CLEO-II recompressed data, this effect should be seriously considered as a big source of systematic uncertainties for particles whose natural widths and mass resolutions are small.

Some studies are performed to check the correctness of Monte Carlo determined efficiencies of particle reconstruction. We calculated the decay ratios of each Λ_c^+ decay mode relative to p$K^-\pi^+$ based on the actual yields from the data and Monte Carlo predicted efficiencies, and they all agree within 10% with the Monte Carlo generated ratios. As we measure all production and branching fractions by ratio relative to Λ_c^+, the effect of the error of Λ_c^+ reconstruction efficiency mostly cancels in the ratio.

*For the real data, the $M(D^{*+}) - M(D^0)$ spectrum is difficult to fit due to the uncertain background shape near the peak, which is very close to the kinematic threshold. When we fitted the signal at a different pion momentum range, we found that fitted width is closer to the Monte Carlo predicted resolution at higher momentum pions. By using different fitting procedures to fit signals at different pion momentum ranges, 0.63 MeV/c^2 is the largest fitted width. We believe that 15% is a conservative estimate of how much the Monte Carlo miscalculates the mass-difference resolution.

4.3 Signals and Fits

To observe Λ_{c1}^+ signals, we combine each Λ_c^+ candidate with two pions ($\pi^+\pi^-$ or $\pi^0\pi^0$), reconstruct the invariant mass with the Λ_c^+, then fit the spectrum of the mass difference $M(\Lambda_c^+\pi\pi) - M(\Lambda_c^+)$. Λ_c^+ selection criteria are described in the last chapter, and the reconstructed masses of Λ_c^+ candidates are required to be within $1.6\sigma_{M_{\Lambda_c^+}}$ of 2.2867 MeV/c^2, our fitted mean value of the Λ_c^+mass. As Λ_{c1}^+ decays are strong decays, their lifetimes are very short. We can assume that they decay at the interaction point of e^+e^- annihilation. The event vertex finding procedure is described in Chapter 3. When we reconstruct the invariant mass of each $\Lambda_c^+\pi\pi$ combination, we constrain the three particles to be from the event vertex. We find that using vertex constraint improves the resolution of the $\Lambda_{c1}^+(2625)$ by more than 10% for the $\Lambda_c^+\pi^+\pi^-$case. In order to see very clean signals,* we require $x_p > 0.7$ for each $\Lambda_c^+\pi\pi$ combination. x_p is defined as

$$\frac{p_{\Lambda_{c1}^+}}{\sqrt{E_{beam}^2 - M_{\Lambda_{c1}^+}^2}},$$

where $p_{\Lambda_{c1}^+}$ is the total momentum of the $\Lambda_c^+\pi\pi$ combination, E_{beam} is the beam energy of the $e^+(e^-)$, and $M_{\Lambda_{c1}^+}$ is the mass of the Λ_{c1}^+.

4.3.1 $\Lambda_c^+\pi^+\pi^-$

Shown in Figure 4.1 is the mass-difference spectrum of $\Lambda_c^+\pi^+\pi^-$ combinations. The large peak at 342 MeV/c^2 is due to the decay $\Lambda_{c1}^+(2625) \rightarrow \Lambda_c^+\pi^+\pi^-$, and the smaller peak at approximately 309 MeV/c^2 is from $\Lambda_{c1}^+(2593) \rightarrow \Lambda_c^+\pi^+\pi^-$.

To fit the the mass-difference distribution, we used a second-order Chebyshev polynomial to fit the background and two signal functions to fit the peaks. Each

*As we can see in later sections, having low background is very important to measure the $\Sigma_c\pi$ substructure.

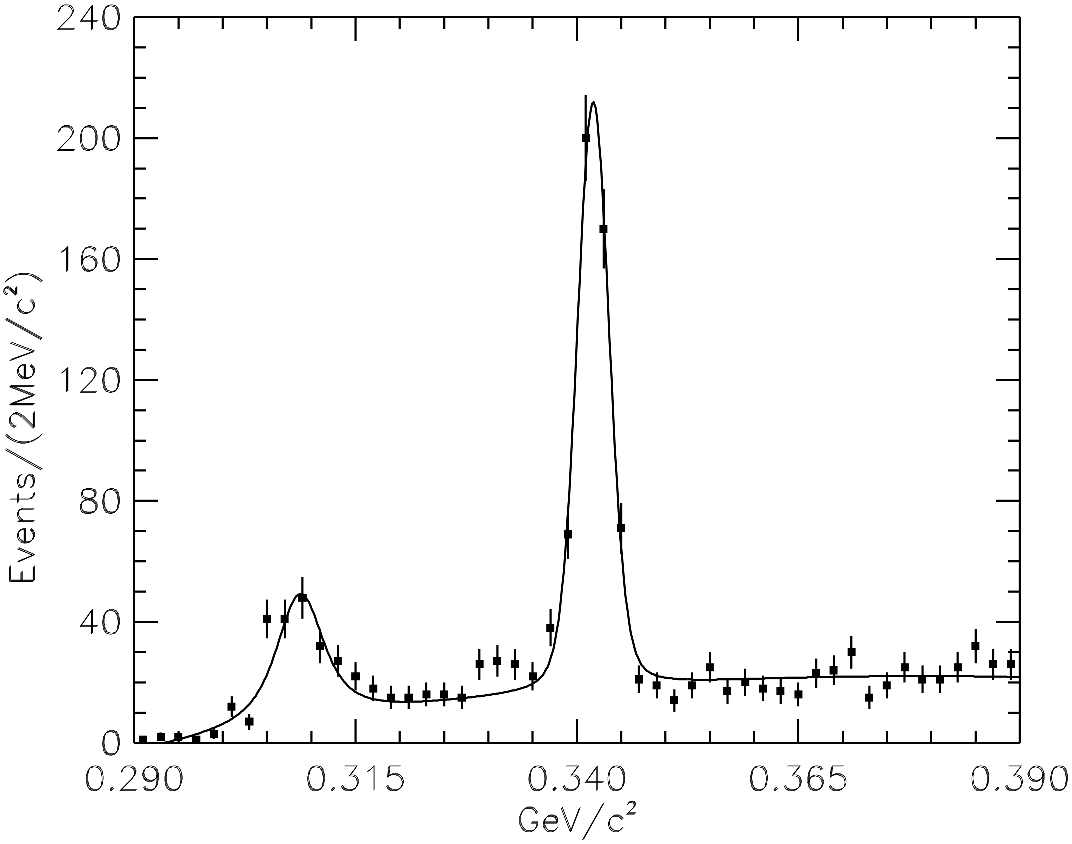

Figure 4.1: Mass difference $M(\Lambda_c^+\pi^+\pi^-) - M(\Lambda_c^+)$

signal function is a Breit-Wigner function with a floating width convoluted with a single Gaussian function with a fixed width. The Breit-Wigner widths reflect the intrinsic widths of the particles; while the Gaussian widths, which are 1.28 MeV/c^2 for the $\Lambda_{c1}^+(2593)$ and 1.62 MeV/c^2 for the $\Lambda_{c1}^+(2625)$ determined from the Monte Carlo studies, are used to parameterize the detector resolutions.

In order to prove that signals in Figure 4.1 are not artifacts of special selection criteria, we checked the backgrounds from two sources: one is the combination of a fake Λ_c^+ candidate taken Λ_c^+ sidebands and $\pi^+\pi^-$, the other is the combination of a Λ_c^+ with two same-sign pions ($\pi^\pm\pi^\pm$). As Figure 4.2 shows, these mass-difference distributions are smooth and similar to the $\Lambda_c^+\pi^+\pi^-$ background. These plots can be fitted very well using the fixed background parameterization as used in Figure 4.1.

As shown in Figure 4.1, it is obvious that the $\Lambda_{c1}^+(2593)$ peak is not fitted well by a Breit-Wigner convoluted with a Gaussian. Fitting uncertainties on both the mass and the width are big. We will discuss this further in the next chapter after presenting the Σ_c mass measurements.*

The extracted Breit-Wigner width of the $\Lambda_{c1}^+(2625)$ with a 1.62 MeV/c^2 Gaussian resolution is 0.7±0.3 MeV/c^2, close to zero. But the question is, have we measured a finite width of the $\Lambda_{c1}^+(2625)$?

As we mentioned in the last section, for CLEO-II the actual detector resolution may be as much as 15% larger than the Monte Carlo predicted value. If we fit the $\Lambda_{c1}^+(2625)$ with a single Gaussian with a floating width, the fitted width is 1.76±0.12 MeV/c^2, less than 10% larger than the Monte Carlo predicted value. So taking statistical errors into account, we cannot conclude that we have observed a finite natural width of the $\Lambda_{c1}^+(2625)$. Therefore, in the following study, we calculated the

*We also remeasured the $\Lambda_{c1}^+(2593)$ signal by a new technique. This second method is only possible after a measurement of Σ_c width and mass. The measurements give different mass and width values.

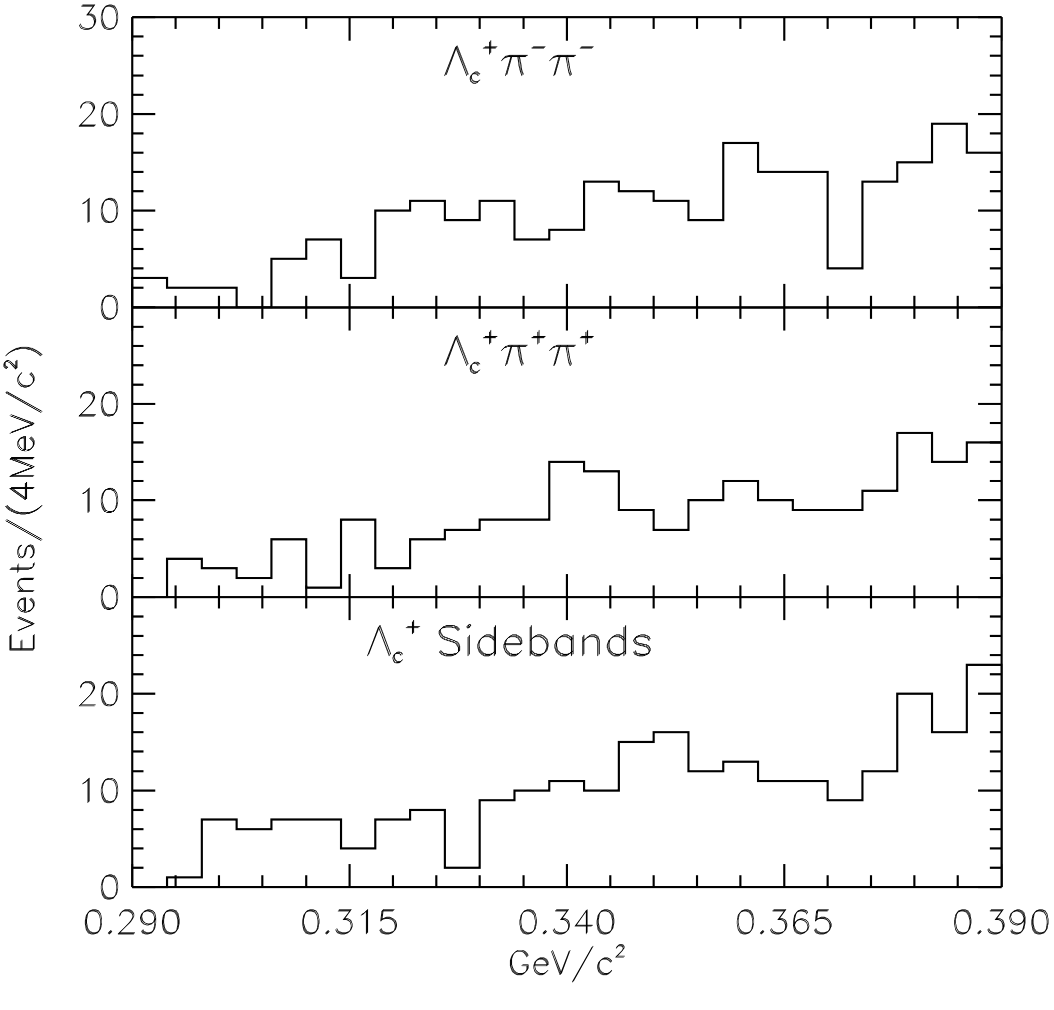

Figure 4.2: The top plot shows the mass difference $M(\Lambda_c^+\pi^-\pi^-) - M(\Lambda_c^+)$ and the middle plot shows $M(\Lambda_c^+\pi^+\pi^+) - M(\Lambda_c^+)$, and Λ_c^+'s candidates are taken with masses with 1.6 $\sigma_{M_{\Lambda_c^+}}$ from 2.2867 MeV/c^2. The bottom plot shows $M(\Lambda_c^+\pi^+\pi^-) - M($"$\Lambda_c^+$ side"$)$, where a "Λ_c^+ side" is from Λ_c^+ sidebands which are taken from 3.4 to 5.0 $\sigma_{M_{\Lambda_c^+}}$ away from 2.2867 MeV/c^2.

production rate of the $\Lambda_{c1}^{+}(2625)$ by using the yield of the signal fitted by a single Gaussian, which is roughly 10% smaller than the yield obtained from the fit using a Breit-Wigner convoluted with a Gaussian. Corresponding systematic uncertainties were added in the final results of branching ratios and production ratios.

Table 4.1 shows the yields, mass differences, and widths obtained by using different fits to Figure 4.1. Fit Type 1 uses a Breit-Wigner convoluted with a Gaussian for the $\Lambda_{c1}^{+}(2593)$ peak and a single Gaussian for the $\Lambda_{c1}^{+}(2625)$ peak. Type 2 fits the region right to 294 MeV/c^2, excluding two entries from the plot. Type 3 uses a third-order polynomial to fit the background instead of the second-order one. Higher-order polynomials were also used, and the results are very similar. Types 4, 5, and 6 only fit the $\Lambda_{c1}^{+}(2593)$ peak. Type 4 excludes the region from 325 MeV/c^2 to 360 MeV/c^2; Type 5 excludes from 335 MeV/c^2 to 350 MeV/c^2; Type 6 only fits the region from 290 MeV/c^2 to 325 MeV/c^2. Types 7 and 8 only fit the $\Lambda_{c1}^{+}(2625)$ peak. Type 7 fits only from 335 MeV/c^2 to 390 MeV/c^2 and Type 8 excludes from 300 MeV/c^2 to 325 MeV/c^2. Type 9 uses a Breit-Wigner convoluted with a Gaussian to fit the $\Lambda_{c1}^{+}(2625)$ peak instead of a single Gaussian. The errors from Type 2 to Type 8 are not shown since they are roughly the same as in Type 1. We have performed more variations of fits other than listed in Table 4.1. Variations of the results are all within the range Table 4.1 shows.

Different values of x_p and cut around the Λ_c^{+} mass may vary the results of the mass and the width. As we checked, the variation of the widths on both particles and the mass difference of the $\Lambda_{c1}^{+}(2625)$ is less than the one shown in Table 4.1, but the mass of the $\Lambda_{c1}^{+}(2593)$ varies from 308.2 MeV/$c^2$to 309.1 MeV/c^2.

Table 4.1: The measured yield, mass, and extracted width of $\Lambda_{c1}^+ \to \Lambda_c^+\pi^+\pi^-$ by various fits.

	Fit Type	Yield	Mass(MeV/c^2)	Width(MeV/c^2)
$\Lambda_{c1}^+(2593)$	1	191^{+31}_{-28}	308.8 ± 0.4	$4.7^{+1.3}_{-1.1}$
	2	204	308.7	5.2
	3	175	308.6	4.2
	4	209	308.9	5.3
	5	194	308.7	4.9
	6	181	308.7	4.4
$\Lambda_{c1}^+(2625)$	1	431 ± 23	341.80 ± 0.10	
	2	428	341.78	
	3	428	341.81	
	4	433	341.84	
	7	429	341.77	
	8	431	341.86	
	9	475^{+29}_{-28}	341.84 ± 0.11	0.7 ± 0.3

4.3.2 $\Lambda_c^+\pi^0\pi^0$

To search for $\Lambda_{c1}^+ \to \Lambda_c^+\pi^0\pi^0$ signals, we combined each Λ_c^+ candidate with two π^0's and measured the mass difference with Λ_c^+. π^0 selection criteria are described in the last chapter. However, to suppress large background we need an additional cut on π^0 momentum. We chose the cut based on the optimization of the Monte Carlo signal versus the background from the data. As Table 4.2 shows, the Monte Carlo predicts that 150 MeV/c gives best signal to background ratio for different momentum cuts. By fitting the signals in the $M(\Lambda_c^+\pi^0\pi^0) - M(\Lambda_c^+)$ spectrum of the data using different $P(\pi^0)$ cuts, we have found the results are consistent with the Monte Carlo efficiencies.

The spectrum and its fit of the mass difference of $\Lambda_c^+\pi^0\pi^0$ combinations are shown in Figure 4.3. As we expected, two Λ_{c1}^+ signals present at 309 MeV/c^2 and 342 MeV/c^2. Unlike the $\Lambda_c^+\pi^+\pi^-$ case in which we see a much larger $\Lambda_{c1}^+(2625)$ signal than $\Lambda_{c1}^+(2593)$'s, the two signals are roughly the same size. The $\Lambda_{c1}^+(2593)$

Table 4.2: Signal versus background of $\Lambda_c^+\pi^0\pi^0$ combinations for different π^0 momentum cuts. S_1 and S_2 in the table are the fitted areas of the $\Lambda_{c1}^+(2593)$ and the $\Lambda_{c1}^+(2625)$, respectively, decaying into $\Lambda_c^+\pi^0\pi^0$ from Monte Carlo studies; while B is the background from plotting $\Lambda_c^+\pi^0\pi^0$ combinations of real data.

$P(\pi^0)$ (GeV/c^2)	S_1	S_2	B	$S_1/\sqrt{B}$	$S_2/\sqrt{B}$
0.50	747	661	6480	9.3	8.2
0.10	697	575	4380	10.5	8.7
0.15	518	424	2290	10.8	8.9
0.20	279	277	1078	8.5	7.2
0.25	69	109	414	3.4	5.4

signal is three times as large as our estimation from Monte Carlo efficiencies and isospin symmetry. We will provide an explanation in the next chapter.

To fit the plot, we have used the same functions as in the $\Lambda_c^+\pi\pi$ mass-difference spectrum. Also shown in the plot as a histogram is the mass-difference spectrum obtained by using Λ_c^+ sidebands instead of Λ_c^+ candidates. Sidebands are picked from 3.4 to 5.0 $\sigma_{M_{\Lambda_c^+}}$ on both side of Λ_c^+ mass. No evidence of peaks can be seen* in this Λ_c^+ sideband mass-difference distribution and its shape is consistent with the $M(\Lambda_c^+\pi^0\pi^0) - M(\Lambda_c^+)$ background.

We have fitted Figure 4.3 in many different ways. Table 4.3 shows the results from some different fitting procedures.

Fit Type 1 uses a Breit-Wigner convoluted with a Gaussian with a fixed width of 2.4 MeV/c^2 to fit the $\Lambda_{c1}^+(2593)$ signal and a single Gaussian with a fixed width of 2.9 MeV/c^2 to fit the $\Lambda_{c1}^+(2625)$ signal. Both Gaussian widths are determined by Monte Carlo studies. Type 2 fixes the width of the $\Lambda_{c1}^+(2593)$ signal using the measured value from the $\Lambda_c^+\pi\pi$ decay, with the Gaussian width floated. Types 3 and 4 only fit the $\Lambda_{c1}^+(2593)$ signal. Type 3 fits the region from 290 MeV/c^2 to 320 MeV/c^2, and Type 4 excludes the region from 230 MeV/c^2 to 355 MeV/c^2. Type 6

*By fitting it with the fixed masses and widths, we find yields of 23 ± 14 at 307 MeV/c^2 and -9 ± 14 at 342 MeV/c^2.

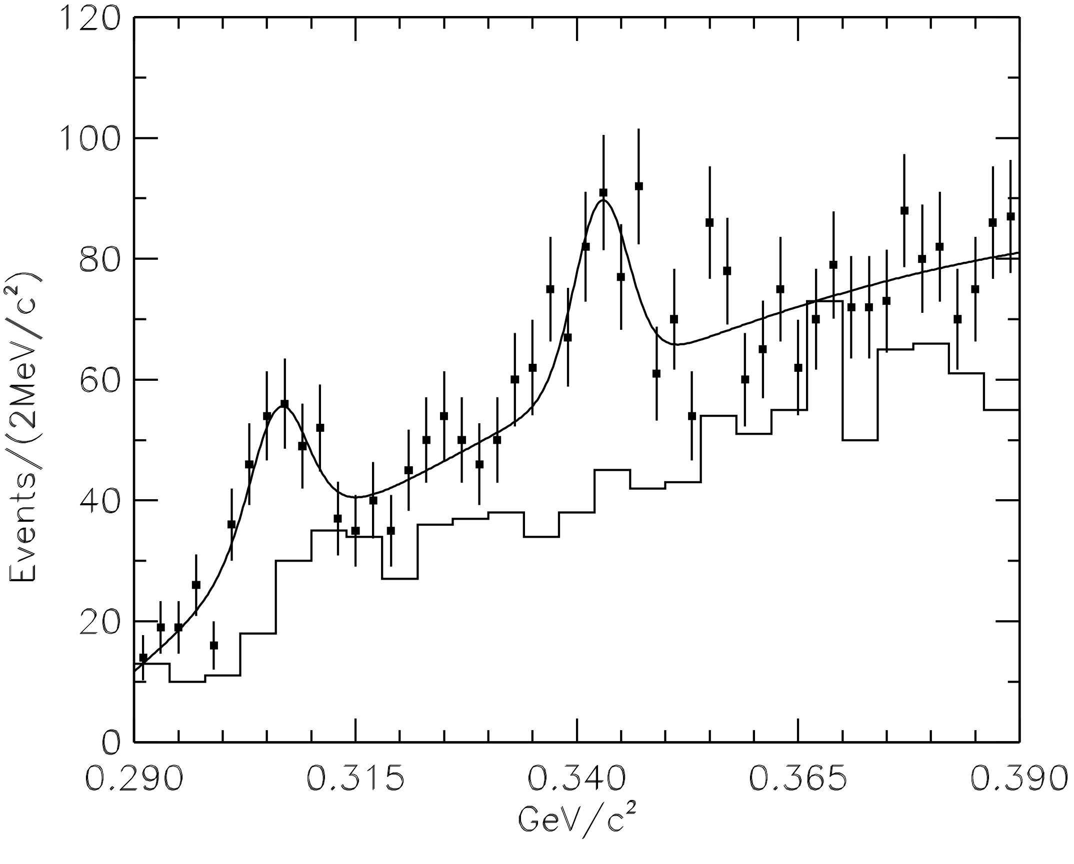

Figure 4.3: Mass difference $M(\Lambda_c^+\pi^0\pi^0) - M(\Lambda_c^+)$ together with the rescaled histogram which is the mass difference $M(\Lambda_c^+\pi^0\pi^0) - M($"$\Lambda_c^+$ side"$)$, where "Λ_c^+ side" is the same as the one in Figure 4.2.

Table 4.3: The yield, mass difference($\Delta(M)$), Breit-Wigner width(Γ), and Gaussian width(σ) of signal events from various fits to $\Lambda_{c1}^+ \to \Lambda_c^+\pi^0\pi^0$. The numbers labeled by $*$ are fixed values in the fit.

	Fit Type	Yield	$\Delta(M)$(MeV/c^2)	Γ(MeV/c^2)	σ(MeV/c^2)
$\Lambda_{c1}^+(2593)$	1	99^{+32}_{-26}	306.3 ± 0.7	$2.9^{+2.6}_{-2.0}$	$2.4*$
	2	113^{+27}_{-23}	306.4 ± 0.7	$4.7*$	$2.3^{+1.1}_{-1.0}$
	3	129^{+39}_{-30}	306.6 ± 0.8	$5.8^{+3.2}_{-2.5}$	$2.4*$
	4	109^{+36}_{-26}	306.2 ± 0.7	$3.2^{+2.8}_{-2.1}$	$2.4*$
	5	102^{+34}_{-27}	306.2 ± 0.7	$3.1^{+2.7}_{-2.1}$	$2.4*$
$\Lambda_{c1}^+(2625)$	1	105 ± 22	342.9 ± 0.9		$2.9*$
	5	150^{+46}_{-38}	342.2 ± 1.1		$4.6^{+1.5}_{-1.1}$
	6	132 ± 27	$342.7^{+0.9}_{-1.0}$	$1.5*$	$2.9*$
	7	106 ± 24	343.0 ± 0.9		$2.9*$
	8	107 ± 23	342.8 ± 0.9		$2.9*$

and further only fit the $\Lambda_{c1}^+(2625)$ signal. Type 6 fits the signal with a Breit-Wigner with a fixed width of 1.5 MeV/c^2 convoluted with a Gaussian with a fixed with of 2.9 MeV/c^2.* Type 7 fits the region to the right of 320 MeV/c^2, and Type 8 excludes the region from 300 MeV/c^2 to 315 MeV/c^2.

Many other variations of fits like these are also performed. We find that using higher-order polynomials to fit the background gives almost the same results. Also, results are consistent with the ones in Table 4.3 if we fit only one peak by excluding the region of the other peak in the plot.

These fitting results show very strong evidence that the decay mode $\Lambda_{c1}^+ \to \Lambda_c^+\pi^0\pi^0$ does exist for both the $\Lambda_{c1}^+(2593)$ and the $\Lambda_{c1}^+(2625)$. The next point of interest is to calculate the branching ratio $\mathcal{B}(\Lambda_{c1}^+ \to \Lambda_c^+\pi^0\pi^0)/\mathcal{B}(\Lambda_{c1}^+ \to \Lambda_c^+\pi^+\pi^-)$. To do this we need to estimate the errors on the yields of $\Lambda_c^+\pi^0\pi^0$ signals.

We not only have large statistical errors because of the poor signal, but also large systematic errors, mostly due to the uncertainties of the resolutions and the natural

*The reason we do this fit is that we do not trust the result on fit Type 5 since the width is too much wider than the Monte Carlo predicted resolution. Here we use this fit trying to estimate the upper limit of the yield

Table 4.4: Comparison of productions of $\Lambda_c^+\pi^0\pi^0$ for different momentum cuts. The $\Lambda_{c1}^+(2593)$ yields are from the fits using a Breit-Wigner function with $\Gamma = 4.7$ MeV/c^2 convoluted with a Gaussian with fixed width from Monte Carlo studies. The $\Lambda_{c1}^+(2625)$ yields are from fits using a single Gaussian with fixed width from the Monte Carlo. The statistical errors on efficiencies are tiny.

	P_{π^0}(GeV)	Yield	Efficiency(%)	Yield/Efficiency($\times$100)
$\Lambda_{c1}^+(2593)$	0.05	133 ± 30	2.35	57 ± 13
	0.10	145 ± 28	2.19	66 ± 13
	0.15	115 ± 20	1.63	70 ± 12
	0.20	59 ± 13	0.88	67 ± 15
	0.25	11 ± 9	0.22	50 ± 41
$\Lambda_{c1}^+(2625)$	0.05	107 ± 34	2.46	43 ± 14
	0.10	95 ± 30	2.31	41 ± 13
	0.15	105 ± 22	1.78	59 ± 12
	0.20	65 ± 17	0.95	68 ± 18
	0.25	38 ± 11	0.37	103 ± 30

width of the particle. Thus we have fitted the signals by varying the resolution by $\pm 20\%$ of the Monte Carlo predicted values, varying the width of the $\Lambda_{c1}^+(2593)$ from 2 MeV/c^2 to 7 MeV/c^2, and varying the width of the $\Lambda_{c1}^+(2625)$ from 0 to 1.5 MeV/c^2. We then estimate that the fitting uncertainties of the yields are $^{+43}_{-15}$ for the $\Lambda_{c1}^+(2593)$ and $^{+27}_{-10}$ for the $\Lambda_{c1}^+(2625)$.

Since a 150 MeV/c momentum cut on both independent π^0's is a very hard cut, a consistency check has been made by comparing the efficiency-corrected productions for different π^0 momentum cuts. As shown in Table 4.4, for the $\Lambda_{c1}^+(2593)$ decay, the Monte Carlo and the data agree very well, but for the $\Lambda_{c1}^+(2625)$, we see some disgreement. Thus we need to intoduce a corresponding systematic error when we calculate the decay ratios.

4.4 Substructures

Studying $\Lambda_{c1}^+ \to \Lambda_c^+\pi\pi$ decay substructures through intermediate Σ_c's is very useful to identify J^P of the Λ_{c1}^+'s and gain more understanding of these two states. In this section, we describe the measurements on the number of Λ_{c1}^+'s which decay to Σ_c's. The ratio is defined to be

$$f_{\Sigma_c} = \mathcal{B}(\Lambda_{c1}^+ \to \Sigma_c\pi)/\mathcal{B}(\Lambda_{c1}^+ \to \Lambda_c^+\pi\pi).$$

4.4.1 $\Lambda_{c1}^+ \to \Sigma_c^{++}\pi^-$ and $\Lambda_{c1}^+ \to \Sigma_c^0\pi^+$

Figure 4.4 plots the mass difference $M(\Lambda_c^+\pi^-) - M(\Lambda_c^+)$ against $M(\Lambda_c^+\pi^+) - M(\Lambda_c^+)$ for the same $\Lambda_c^+\pi^+\pi^-$ combinations in Figure 4.1. By looking directly at the figure, it is easy to tell that there are two very prominent clusters which correspond to the decays through intermediate Σ_c^{++} and Σ_c^0at the two ends of the diagonal band of $\Lambda_{c1}^+(2593)$'s in which all entries are shown as inverted triangles; in the diagonal band of $\Lambda_{c1}^+(2625)$'s in which all entries are shown as triangles, no obvious clusters can be seen. Therefore, by simply inspecting this scatter plot, we can tell that the $\Sigma_c\pi$ mode dominates the $\Lambda_{c1}^+(2593)$ decay, and the non-resonant $\Lambda_c^+\pi\pi$ mode dominates the $\Lambda_{c1}^+(2625)$ decay.

To determine the fraction $f_{\Sigma_c^{++}}$ and $f_{\Sigma_c^0}$ of the $\Lambda_{c1}^+(2593)$, we first measured the $\Lambda_{c1}^+(2593)$ yield as a function of $\Lambda_c^+\pi^\pm$ submass. Figure 4.5 shows the mass enhancement of Σ_c^0 and Σ_c^{++} from $\Lambda_c^+\pi^+\pi^-$ combinations with the mass difference $M(\Lambda_c^+\pi^+\pi^-) - M(\Lambda_c^+)$ between 304 MeV/c^2 and 314 MeV/c^2.

We fit each plot in Figure 4.5 with a bifurcated Gaussian* (left) and a single Gaussian (right) together with the same background function. The same combinations in the two plots are constrainted to have the same area.

*A bifurcated Gaussian is A Gaussian with different slopes on either side of the mean.

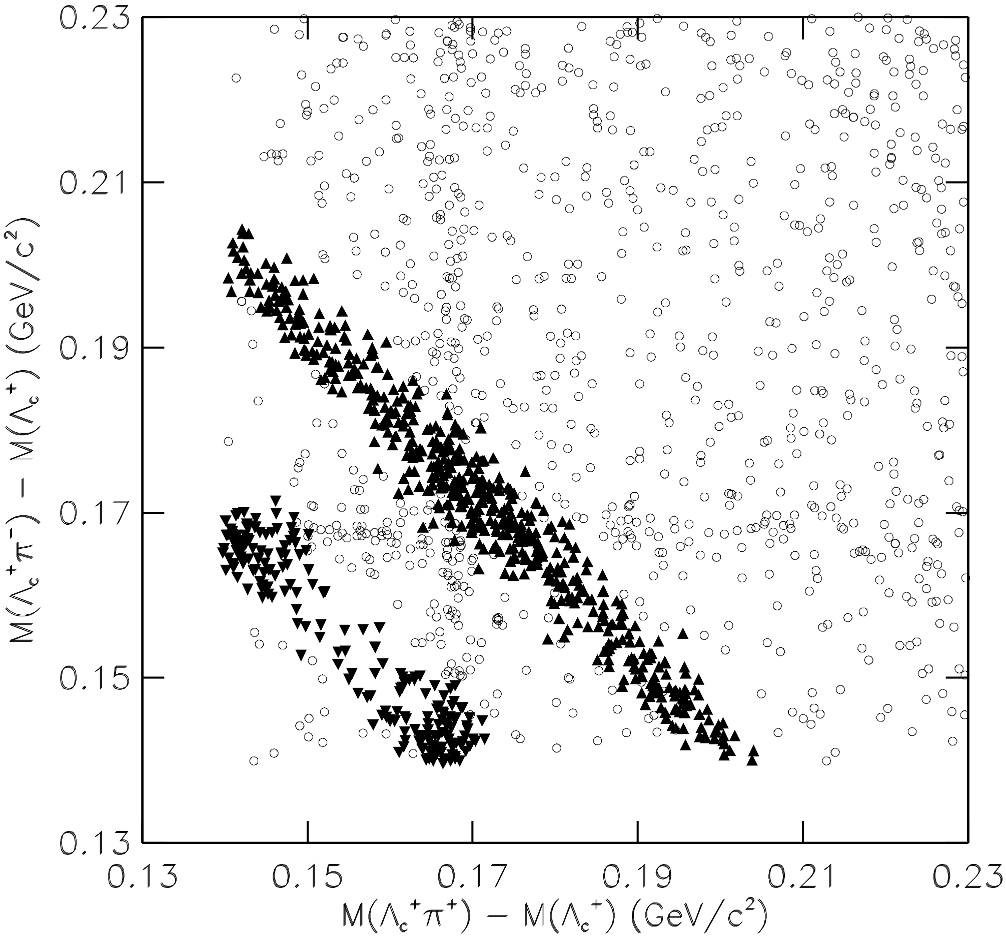

Figure 4.4: Scatter plot of the mass difference $M(\Lambda_c^+\pi^-) - M(\Lambda_c^+)$ vs. the mass difference $M(\Lambda_c^+\pi^+) - M(\Lambda_c^+)$. Shown in the plot are (1) the vertical band at $\Lambda_c^+\pi^+$ mass difference of about 168 MeV/c^2, corresponding to $\Sigma_c^{++} \to \Lambda_c^+\pi^+$; (2) the horizontal band at $\Lambda_c^+\pi^-$ mass difference of about 168 MeV/c^2, corresponding to $\Sigma_c^0 \to \Lambda_c^+\pi^-$; (3) the diagonal band extending from (0.14, 0.20) to (0.20, 0.14), corresponding to combinations from the $\Lambda_{c1}^+(2625)$ signal region in Figure 4.1 (triangles); and (4) the diagonal band extending from (0.14, 0.168) to (0.168, 0.14), corresponding to combinations from the $\Lambda_{c1}^+(2593)$ signal region in 4.1 (inverted triangles), within which there are two lobes at the kinematic limits: (a) the enhancement in the Σ_c^{++} band, just above the threshold for $\Lambda_c^+\pi^+$, and (b) the enhancement in the Σ_c^0 band, just above the threshold for $\Lambda_c^+\pi^-$.

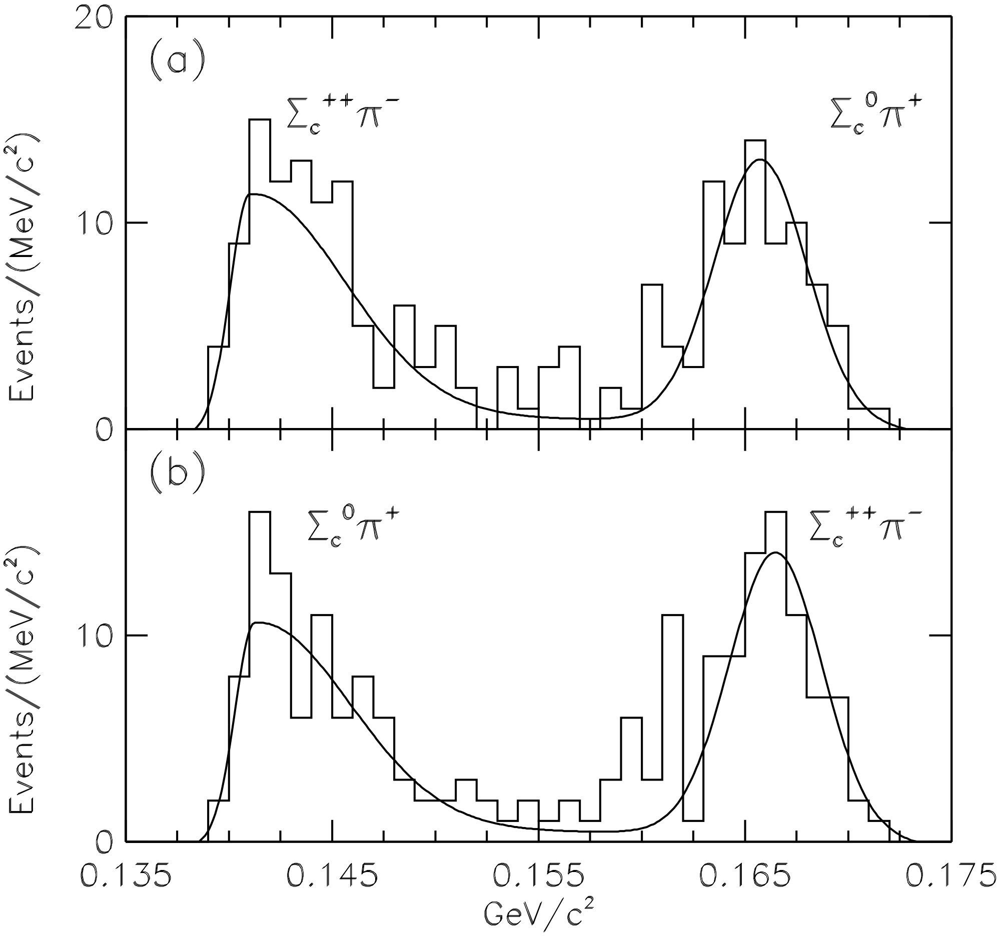

Figure 4.5: Events and fits of Σ_c^0's and Σ_c^{++}'s with the mass difference of $M(\Lambda_c^+\pi^+\pi^-) - M(\Lambda_c^+)$ between 304 MeV/c^2 and 314 MeV/c^2 (the $\Lambda_{c1}^+(2593)$ signal). Plot (a) shows the mass difference $M(\Lambda_c^+\pi^-) - M(\Lambda_c^+)$. The right peak centered at 167 MeV/c^2 is the Σ_c^0 signal; and the left peak is the reflection of the Σ_c^{++} signal on the $\Lambda_{c1}^+(2593)$ band. Plot (b) shows the mass difference $M(\Lambda_c^+\pi^+) - M(\Lambda_c^+)$. The right peak centered at 167 MeV/c^2 is the Σ_c^{++} signal; and the left peak is the reflection of the Σ_c^0 signal on the $\Lambda_{c1}^+(2593)$ band. Since plots (a) and (b) represent the same events projected in two different directions, they are fitted simultaneously by constraining the area of the left/right peak in (a) to be the same as the area of the right/left peak in (b) The left peaks in both (a) and (b) are fitted by bifurcated Gaussians, and the right peaks are fitted by single Gaussians. They are all constrainted to have the same widths.

Shapes of the bifurcated Gaussian and the single Gaussian are determined by Monte Carlo studies of $\Lambda_{c1}^{+}\to\Sigma_c\pi$ and $\Sigma_c\to\Lambda_c^{+}\pi$ decays. The background is expected to be a mixture of two parts: random $\Lambda_c^{+}\pi^{+}\pi^{-}$ combinations and non-resonant $\Lambda_{c1}^{+}(2593)\to\Lambda_c^{+}\pi^{+}\pi^{-}$ events. Alhough it is very difficult to predict what its exact shape is, we know this shape has cut-offs at phase space lower limit 139 MeV/c^2 and upper limit about 172 MeV/c^2,*. We used a "double-threshold" function $y(x)$ with upper and lower thresholds at a and b (in this particular case a = 139 MeV/c^2 and b = 172 MeV/c^2),

$$y(x) = N(x-a)(b-x)e^{s_1(x-a)+s_2(x-a)^2}e^{s_3(b-x)+s_4(b-x)^2}, \tag{4.1}$$

to fit the background of Figure 4.5. Here N is a normalization factor and s_i, where i = 1, 2, 3, and 4, determines the shape of the function. The fitted background shape obtained by fitting the plot in Figure 4.5 with floating s_i's is very consistent with the shape from the Monte Carlo generated $\Lambda_c^{+}\pi^{+}\pi^{-}$ non-resonance decay. As we tested, the fitted results are not sensitive to the variation of the background shape as far as a and b are fixed. Reasonably varying the parameters of the double-threshold function (reasonably means still giving a good fit) makes the yields of signals change within 5% of the mean value of fitted areas. We believe that statistical errors dominate the uncertainties of this measurement.

The areas of Σ_c^{0} and Σ_c^{++} signal we measured from Figure 4.5 are 77±7 and 72±7, respectively. These values are obtained by fitting Figure 4.5 by fixing the background, with shape determined by the Monte Carlo studies of $\Lambda_{c1}^{+}(2593)\to\Lambda_c^{+}\pi^{+}\pi^{-}$ non-resonance decay. To obtain the number of $\Lambda_{c1}^{+}(2593)$'s which decay into $\Sigma_c\pi$, these numbers need to be subtracted by the number of "independent" Σ_c's in the

*The lower limit is really the pion mass, and the upper limit, as we can tell in Figure 4.4 depends on the width of the $\Lambda_{c1}^{+}(2593)$ band.

sideband of the $\Lambda_{c1}^{+}(2593)$ signal. Due to the kinematic limit, only the higher-mass $\Lambda_{c1}^{+}(2593)$ sideband contains Σ_c's. Therefore we estimated the background as being half.

The number of Σ_c's in the $\Lambda_{c1}^{+}(2593)$ sideband were measured similarly as we did with the number of Σ_c's in the $\Lambda_{c1}^{+}(2593)$ peak except that the mass-difference range is wider and the kinematic reflections of the peaks are in different mass-difference ranges. The sidebands were taken from the range of the mass difference $M(\Lambda_c^+\pi^+\pi^-) - M(\Lambda_c^+)$ between 320 MeV/c^2 and 330 MeV/c^2. Figure 4.6 shows the histograms and the fits. The fitted yields are 19±4 of Σ_c^{++}'s and 15±4 of Σ_c^{0}'s.

After subtracting one-half of the yield from the sideband, we obtained the number of $\Lambda_{c1}^{+}(2593)$'s which decay to Σ_c's: 67±8 for the Σ_c^{++} and 65±8 for the Σ_c^{0}. Compared with the total number of $\Lambda_{c1}^{+}(2593)$'s in the mass-difference range between 304 MeV/c^2 and 314 MeV/c^2, which is 137±22 measured in Figure 4.1, we see that resonance via the Σ_c dominates these transitions.

The same methods were applied to measure f_{Σ_c}'s of the $\Lambda_{c1}^{+}(2625)$ except that in this case there are two $\Lambda_{c1}^{+}(2625)$ sidebands other than the one in the $\Lambda_{c1}^{+}(2593)$ case. The numbers of Σ_c^{++}'s and Σ_c^{0}'s inside the $\Lambda_{c1}^{+}(2625)$ signal are measured as shown in Figure 4.7, and the fitted yields are 46±9 for Σ_c^{++} and 36±9 for Σ_c^{0}. The lower $\Lambda_{c1}^{+}(2625)$ sideband is chosen to be between 320 MeV/c^2 and 330 MeV/c^2, which is the same as the one shown in Figure 4.6, and there are 19±4 Σ_c^{++}'s and 15±4 Σ_c^{0}'s. The higher sideband is therefore in the range between 354 MeV/c^2 and 364 MeV/c^2, and the number of Σ_c^{++}'s and Σ_c^{0}'s is measured to be 13±3 and 6±4, respectively. The fit for the higher sideband is shown in Figure 4.8. After the sideband subtraction, the results are 30±10 Λ_{c1}^{+}'s decay to Σ_c^{++}'s and 25±10 decay to Σ_c^{0}'s. These numbers indicate that resonance through Σ_c is very small in the decay of the $\Lambda_{c1}^{+}(2625)$, since the total number of $\Lambda_{c1}^{+}(2625)$'s between mass difference 354 MeV/c^2 and 364 MeV/c^2, 450±29, is much larger.

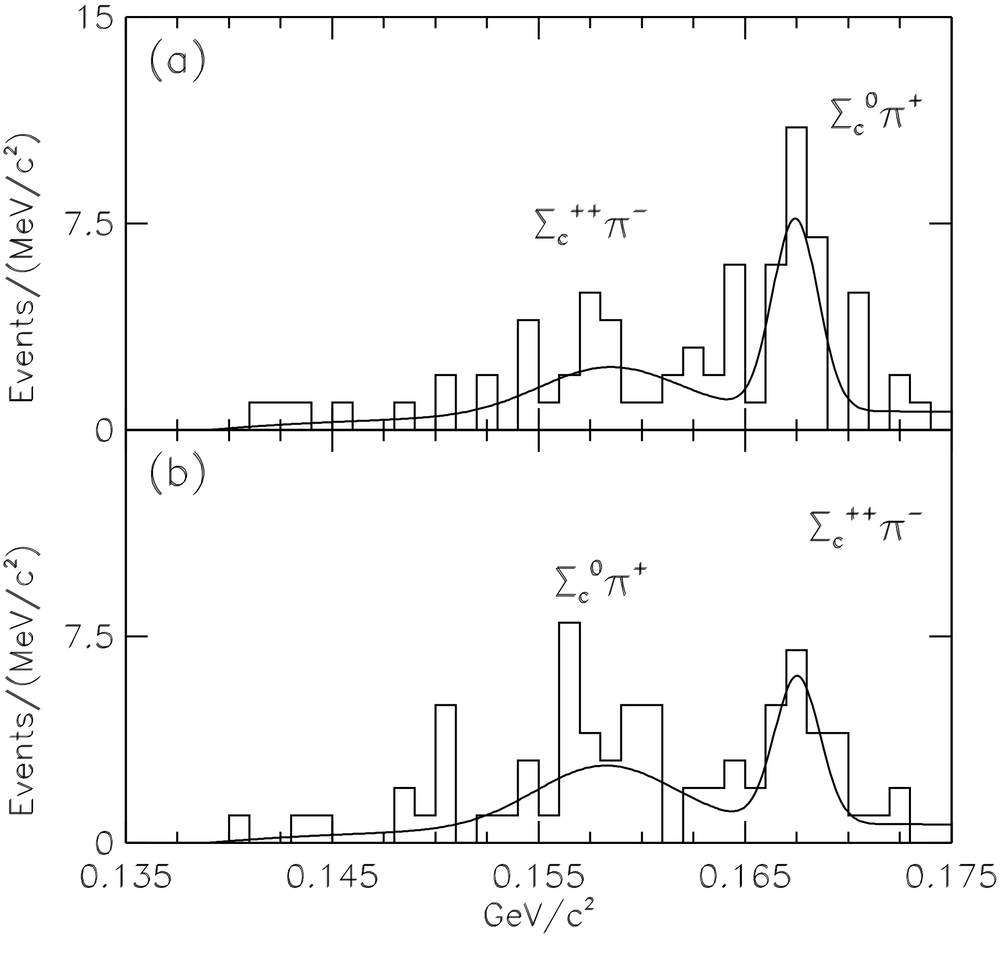

Figure 4.6: Events and the fits of Σ_c^0's and Σ_c^{++}'s in the $\Lambda_{c1}^+(2593)$ sideband. Plot (a) shows the mass difference $M(\Lambda_c^+\pi^-) - M(\Lambda_c^+)$, and plot (b) shows $M(\Lambda_c^+\pi^+) - M(\Lambda_c^+)$. The peaks in the right at about 168 MeV/c^2 on both plots are the signals of the Σ_c^0 and the Σ_c^{++}. In each plot a bump is centered at about 158 MeV/c^2, representing reflections of the $\Sigma_c^0(\Sigma_c^{++})$ peak seen in the direction of $\Sigma_c^{++}(\Sigma_c^0)$. Each plot is fitted by two single Gaussians with fixed widths (3.4 MeV/c^2 of the left bump and 1.1 MeV/c^2 of the right peak) from $\Sigma_c^0 \to \Lambda_c^+\pi^-$ ($\Sigma_c^{++} \to \Lambda_c^+\pi^+$) Monte Carlo studies and a double-threshold function the same as the one used to fit Figure 4.5, with the lower threshold 140 MeV/c^2 and the higher threshold 185 MeV/c^2. The areas representing the same combinations are constrainted to be the same, and the two plots are constrained to have an identical background.

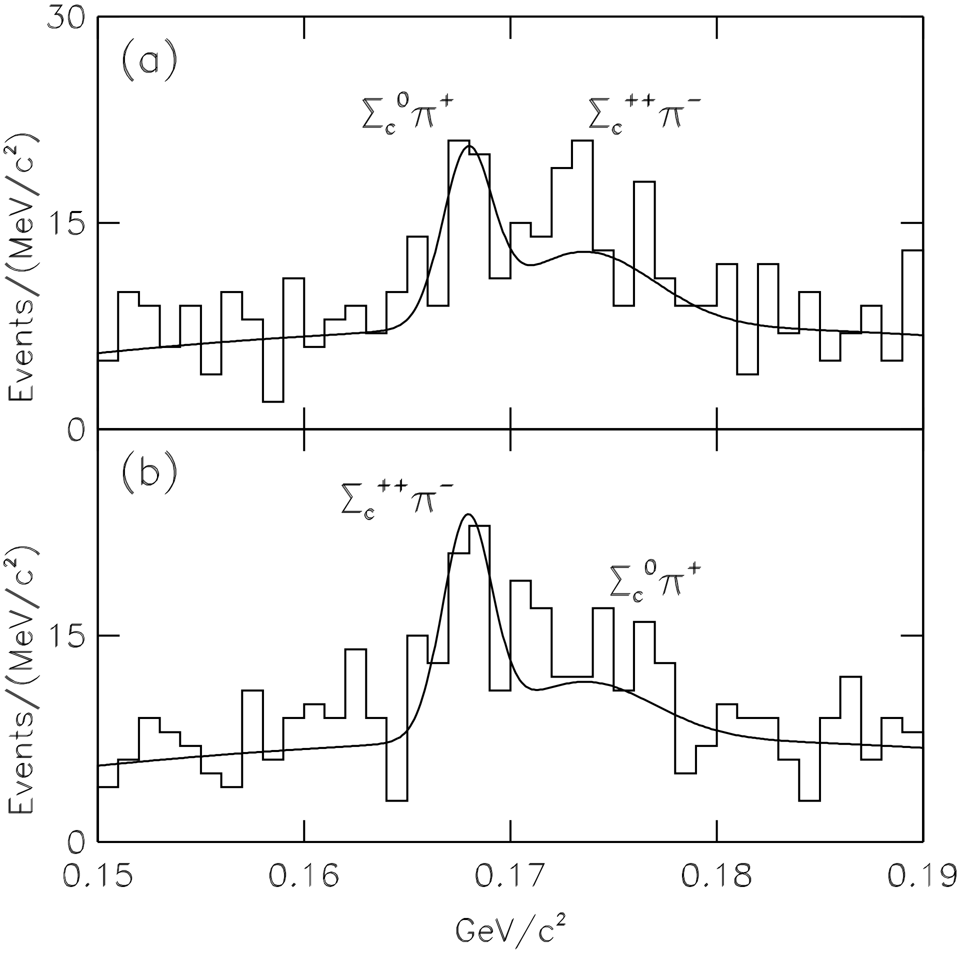

Figure 4.7: The mass difference of $M(\Lambda_c^+\pi^+\pi^-) - M(\Lambda_c^+)$ between 337 MeV/c^2 and 347 MeV/c^2 (the $\Lambda_{c1}^+(2625)$ signal). The meanings of the signals are the analog to those in Figure 4.5. The reflection of the peak of one combination is overlaid with the peak of the other combination. These shapes are predicted by $\Lambda_{c1}^+(2625) \rightarrow \Sigma_c\pi$ Monte Carlo studies. Each plot is fitted by two single Gaussians and a second-order Chebyshev polynomial. The widths of the Gaussians are fixed by the values from the Monte Carlo (1.2 MeV/c^2 of the peak in the left and 3.4 MeV/c^2 of the bump in the right). The areas representing the same combinations are constrained to be the same, and the two plots are constrained to have the same background.

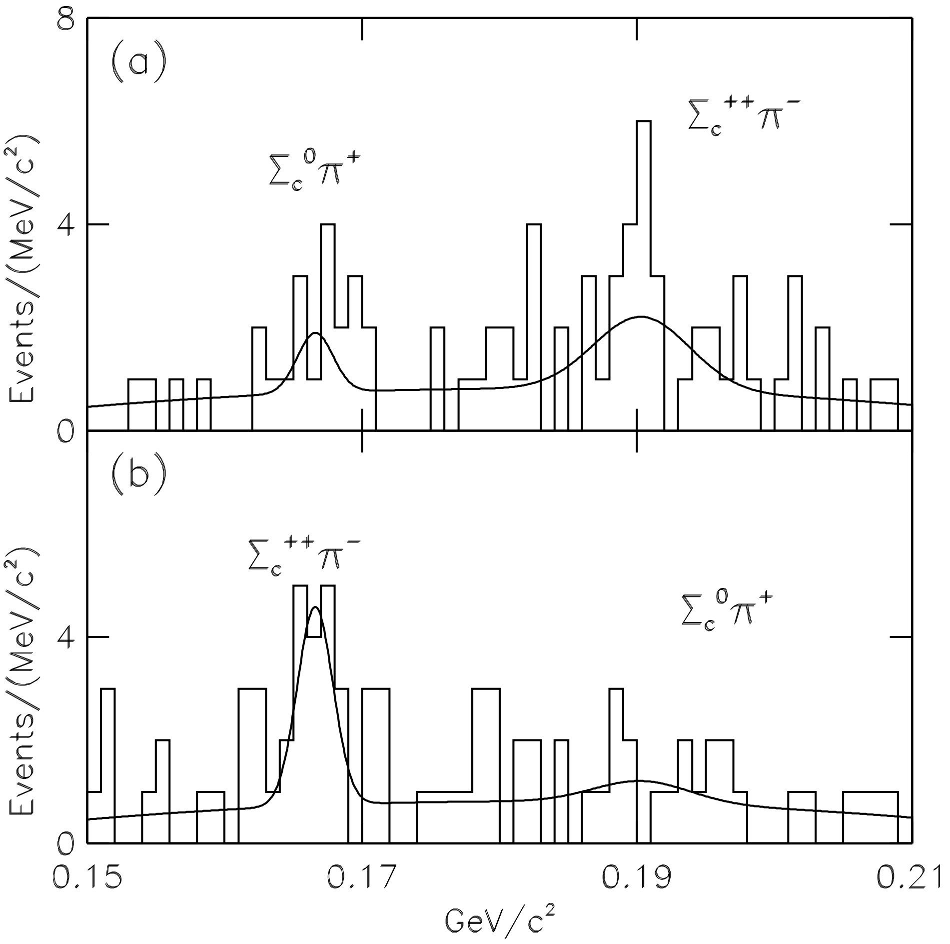

Figure 4.8: The mass difference of $M(\Lambda_c^+\pi^+\pi^-) - M(\Lambda_c^+)$ between 354 MeV/c^2 and 364 MeV/c^2 (the $\Lambda_{c1}^+(2625)$ sideband), fitted in the same way as fitting Figure 4.7. The widths of the Gaussians are fixed by the values from the $\Sigma_c \rightarrow \Lambda_c^+\pi$ Monte Carlo studies (1.3 MeV/c^2 in the left and 4 MeV/c^2 in the right).

After further considerations of systematic errors, we listed our results of $f_{\Sigma_c^{++}}$ and $f_{\Sigma_c^0}$, compared with the measurements with other experiments, in Table 4.13 and Table 4.14.

4.4.2 $\Lambda_{c1}^+ \to \Sigma_c^+\pi^0$

The technique of measuring

$$f_{\Sigma_c^+} = \mathcal{B}(\Lambda_{c1}^+ \to \Sigma_c^+\pi^0)/\mathcal{B}(\Lambda_{c1}^+ \to \Lambda_c^+\pi^0\pi^0),$$

is similar to that of measuring $f_{\Sigma_c^{++}}$ and $f_{\Sigma_c^0}$, and much simpler. Since $\Lambda_c^+\pi^0\pi^0$ decay only has one substructure, which is $\Lambda_c^+\pi^0$, instead of two ($\Sigma_c^{++}\pi^-$ and $\Sigma_c^0\pi^+$), we do not need to do complicated fits to correlate Σ_c^{++} and Σ_c^0 signals as we did in the $\Lambda_c^+\pi^+\pi^-$ case.

The scatter plot of $M(\Lambda_c^+\pi^0\pi^0) - M(\Lambda_c^+)$ versus $M(\Lambda_c^+\pi^0) - M(\Lambda_c^+)$ shown in Figure 4.9 shows the evidence of $\Lambda_{c1}^+(2593)\to\Sigma_c^+\pi^0$ substructure. In the plot, we can see two concentrated clusters of events in the $\Lambda_{c1}^+(2593)$ mass-difference band around 306 MeV/c^2: one at about 167 MeVc^2 which is consistent with Σ_c^+ mass difference, and another which is the kinematic reflection of the first, at about 140 MeV/c^2 just above the kinematic threshold. We cannot see this phenomenon for the $\Lambda_{c1}^+(2625)$ signal.

Low statistics and high background do not allow us to report the $\Lambda_{c1}^+(2625)\to\Sigma_c\pi^0$ measurement (the upper limit would be 1). Thus only a $f_{\Sigma_c^+}(\Lambda_{c1}^+(2593))$ measurement was performed.

Figure 4.10 shows the histogram and the fit of the Σ_c^+ signal and its kinematic reflection at the $\Lambda_{c1}^+(2593)$ mass-difference band taken from the $M(\Lambda_c^+\pi^0\pi^0) - M(\Lambda_c^+)$ mass-difference range between 304 and 314 MeV/c^2. The plot was fitted by two single Gaussians with fixed widths (2.9 MeV/c^2 for the left signal and 2.4 MeV/c^2

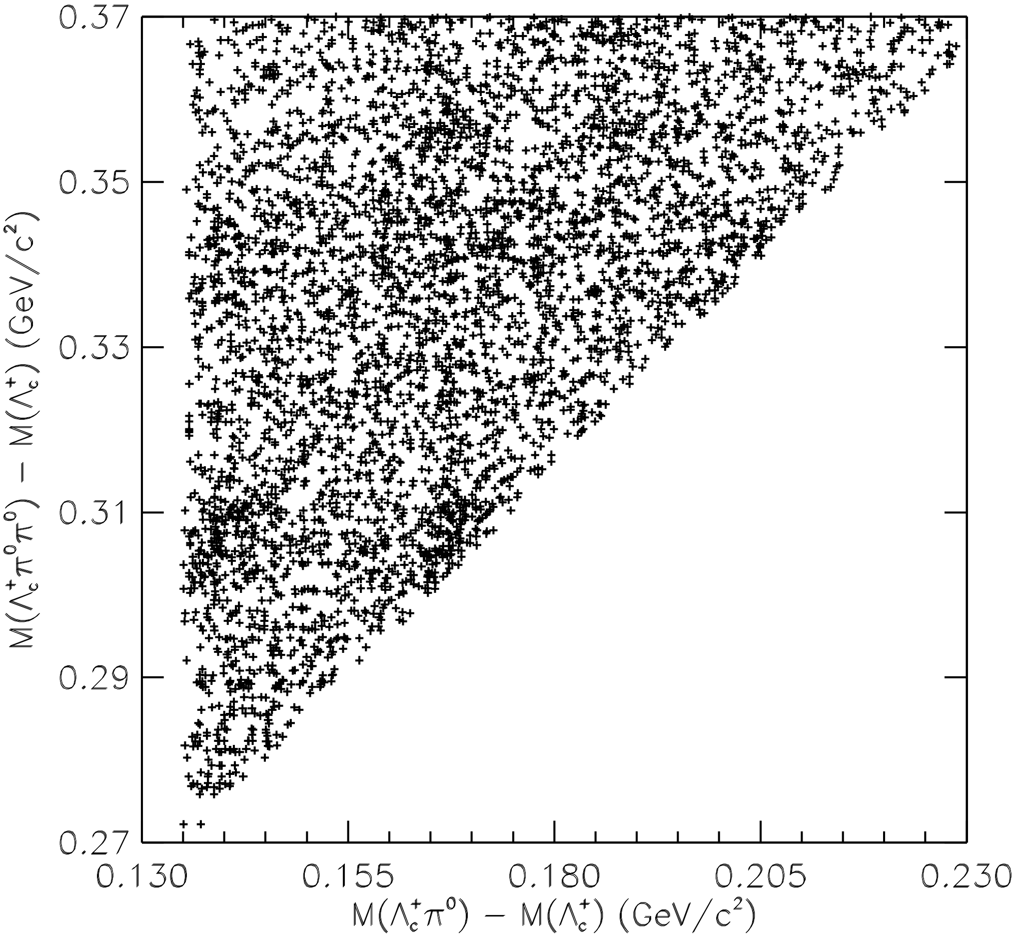

Figure 4.9: Scatter plot of the mass difference $M(\Lambda_c^+\pi^0\pi^0) - M(\Lambda_c^+)$ vs. the mass difference $M(\Lambda_c^+\pi^0) - M(\Lambda_c^+)$. Very visible in the figure is a horizontal band at about 306 MeV/c^2 of $M(\Lambda_c^+\pi^0\pi^0) - M(\Lambda_c^+)$, corresponding to $\Lambda_{c1}^+(2593) \to \Lambda_c^+\pi^0\pi^0$. It has two lobes at the kinematic limits: one at about 167 MeV/c^2 of $M(\Lambda_c^+\pi^0) - M(\Lambda_c^+)$, which is consistent with Σ_c^+ mass difference; and the other just above the kinematic threshold which is π^0 mass. We assume there are three other bands in the plot (visible but not obvious) which are not shown clearly: (1) a vertical band at about 167 MeV/c^2 of $M(\Lambda_c^+\pi^0) - M(\Lambda_c^+)$, corresponding to $\Sigma_c^+ \to \Lambda_c^+\pi^0$; (2) a diagonal band extending from (0.135, 0.308) to (0.2, 0.37), which is the kinematic reflection from band (1), corresponding to the single π^0's from the random $\Sigma_c^+\pi^0$ combinations; (3) a horizontal band at about 342 MeV/c^2 of $M(\Lambda_c^+\pi^0\pi^0) - M(\Lambda_c^+)$, in which no Σ_c^+ clustering can be seen, corresponding to $\Lambda_{c1}^+(2625) \to \Lambda_c^+\pi^0\pi^0$.

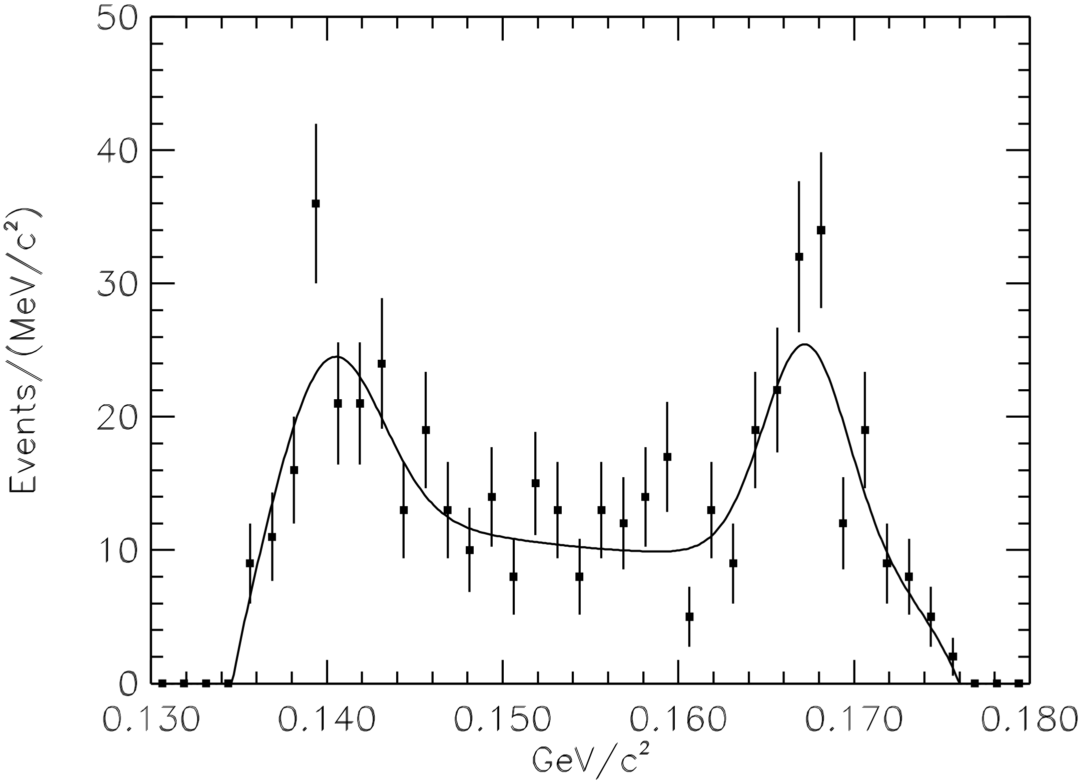

Figure 4.10: The mass difference $M(\Lambda_c^+\pi^0\pi^0) - M(\Lambda_c^+\pi^0)$ between 304 MeV/c^2 and 314 MeV/c^2 (the $\Lambda_{c1}^+(2593)$ signal). The two peaks correspond to Σ_c^+'s (left) and independent π^0's (right) in the $\Lambda_{c1}^+(2593) \to \Sigma_c^+\pi^0$ decay.

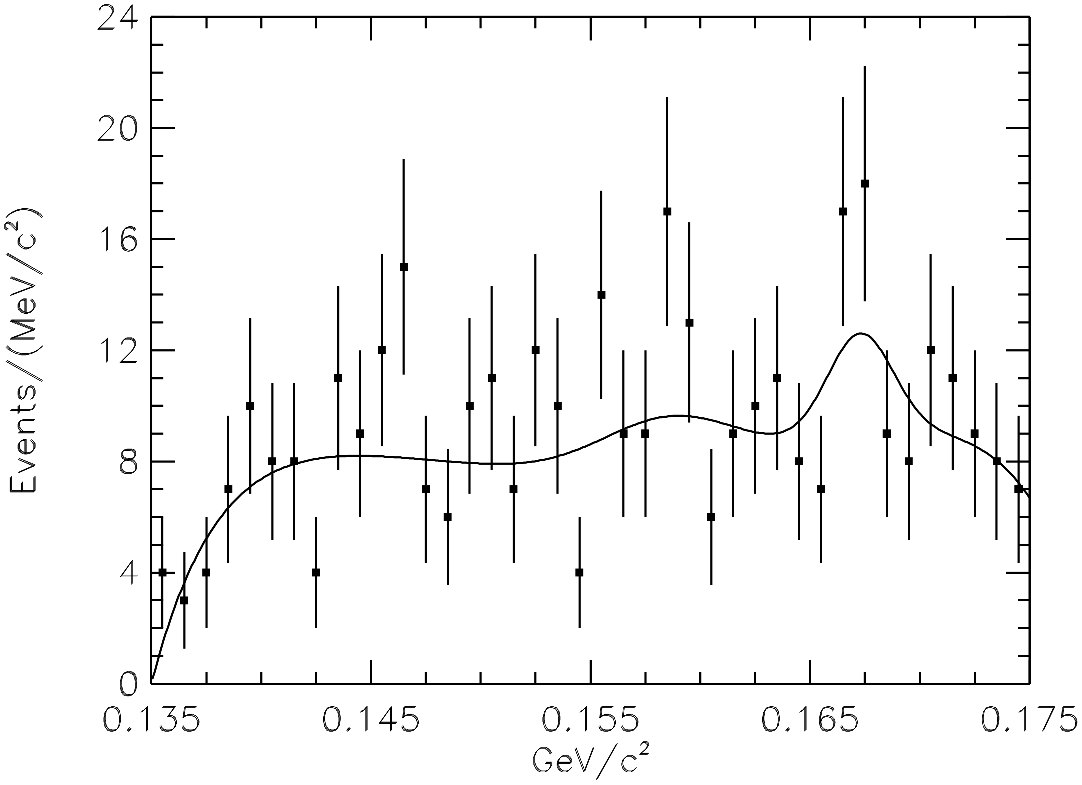

Figure 4.11: The mass difference $M(\Lambda_c^+\pi^0\pi^0) - M(\Lambda_c^+\pi^0)$ between 320 MeV/c^2 and 330 MeV/c^2 (the $\Lambda_{c1}^+(2593)$ sideband). The positions and shapes of the two bumps are determined by the $\Sigma_c^+ \to \Lambda_c^+\pi^0$ Monte Carlo. The signal at right corresponds to $\Sigma_c^+ \to \Lambda_c^+\pi^0$, and the left bump reflects single π^0's from the $\Sigma_c^+\pi^0$ combinations.

for the right signal) determined by the $\Lambda_{c1}^+(2593) \to \Sigma_c^+\pi^0$ Monte Carlo, and a double-threshold function which is defined in equation 4.1. The shape of the double-threshold function with the two thresholds 135 MeV/c^2 and 176 MeV/c^2 is determined by the non-resonance $\Lambda_{c1}^+(2593) \to \Lambda_c^+\pi^0\pi^0$ Monte Carlo. The areas of the the two Gaussians are constrained to be the same. Finally, the fitted yield is 89$\pm$11. Consistent fitting results were obtained when we fitted the background with a floating shape of the double-threshold function.

Figure 4.11 shows the $M(\Lambda_c^+\pi^0) - M(\Lambda_c^+)$ distribution at the $\Lambda_{c1}^+(2593)$ side band and the fit to it. The sideband was taken from the $M(\Lambda_c^+\pi^0\pi^0) - M(\Lambda_c^+)$ range between 320 and 330 MeV/c^2. The plot is fitted by two single Gaussians with fixed mean values and shapes determined by the $\Sigma_c^+ \to \Lambda_c^+ \pi^0$ Monte Carlo, and a double-threshold function with fixed thresholds and other floating parameters. The areas of the these two Gaussians are constrained to be the same. The fitted yield is 14±11.

We finally calculated that 81±16 of $\Lambda_{c1}^+(2593)$ decays are to Σ_c^+'s from a total number of 93±20 $\Lambda_{c1}^+(2593)$'s in the mass-difference range between 304 MeV/c^2 and 314 MeV/c^2. This is consistent with what we have seen in the $\Lambda_{c1}^+(2593) \to \Lambda_c^+ \pi\pi$ decay, for which the $\Sigma_c \pi$ substructure dominates. The result of $f_{\Sigma_c^+}(\Lambda_{c1}^+(2593))$ is presented in Table 4.12 after proper systematic errors are evaluated.

4.5 Search for Other Decays

Since isospin is conserved in strong decays, the $\Lambda_{c1}^+ \to \Lambda_c^+ \pi^0$ is forbidden. If any of the two $\Lambda_c^+ \pi^+ \pi^-$ states we observed were excited Σ_c baryons, $\Lambda_c^+ \pi$ decay should be not only allowed but more favorable than $\Lambda_c^+ \pi\pi$ decays due to the larger phase space. Λ_{c1}^+'s are allowed to decay electromagnetically to $\Lambda_c^+ \gamma$, and if any Λ_{c1}^+'s intrinsic width is sufficiently narrow, its decay may be competitive with $\Lambda_c^+ \pi\pi$ decays.

To search for these decays, we reconstructed $\Lambda_c^+ \pi^0$ and $\Lambda_c^+ \gamma$ combination using our previously defined candidates of Λ_c^+, π^0 and γ. Based on the optimization of Monte Carlo signals versus the background from data, a 200 MeV/c π^0 momentum cut for $\Lambda_c^+ \pi^0$ and a 300 MeV/c photon momentum cut for $\Lambda_c^+ \gamma$ are used.

Figure 4.12 shows the mass-difference spectrum of $M(\Lambda_c^+ \pi^0) - M(\Lambda_c^+)$, and no signal can be observed. To measure the upper limit of decay ratios, three functions are used to fit the distribution. A Breit-Wigner, with fixed 4.7 MeV/c^2 $\Lambda_{c1}^+(2593)$ width, convoluted with a Gaussian with fixed 5.7 MeV/c^2 Monte Carlo predicted resolution, is used to fit at a fixed mean value of 307 MeV/c^2; a single Gaussian

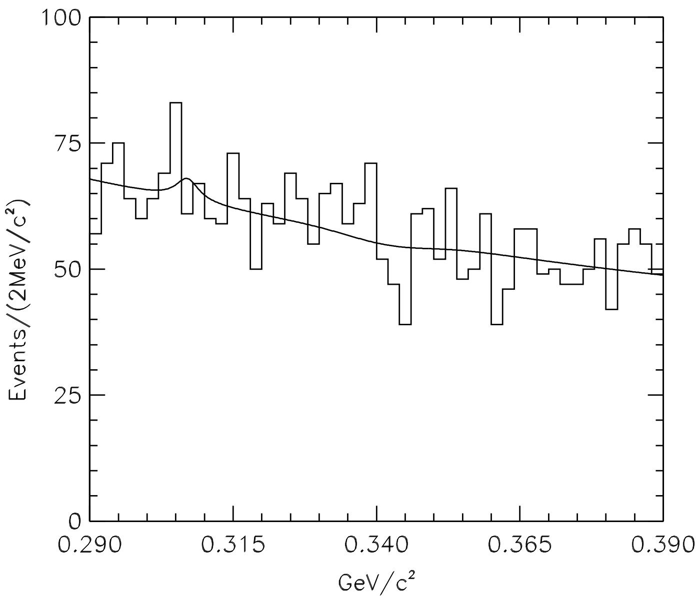

Figure 4.12: Mass difference of $M(\Lambda_c^+\pi^0) - M(\Lambda_c^+)$.

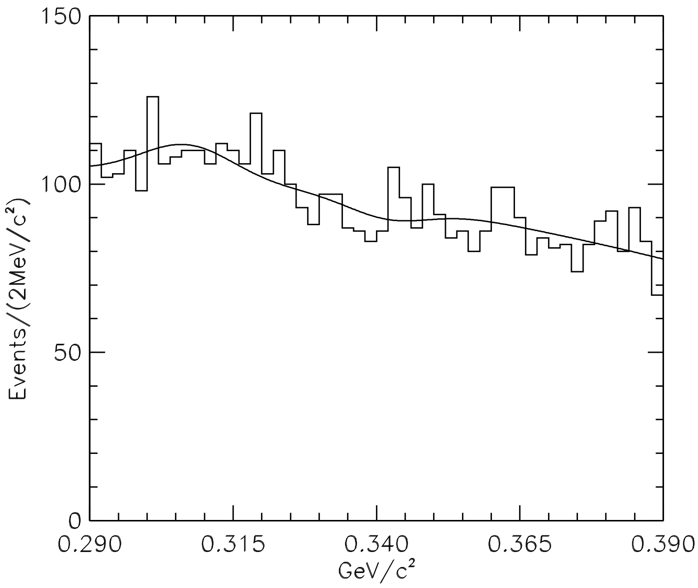

Figure 4.13: Mass difference of $M(\Lambda_c^+\gamma) - M(\Lambda_c^+)$.

Table 4.5: Fitting results on $M(\Lambda_c^+\pi^0)-M(\Lambda_c^+)$ and $M(\Lambda_c^+\gamma)-M(\Lambda_c^+)$ distributions.

Decay	Yield	Yield Upper Limit (90% C. L.)
$\Lambda_{c1}^+(2593)\to\Lambda_c^+\pi^0$	26 ± 28	160
$\Lambda_{c1}^+(2625)\to\Lambda_c^+\pi^0$	-8 ± 36	165
$\Lambda_{c1}^+(2593)\to\Lambda_c^+\gamma$	96 ± 71	381
$\Lambda_{c1}^+(2625)\to\Lambda_c^+\gamma$	-42 ± 52	120

with 6.7 MeV/c^2 Monte Carlo predicted resolution is used to fit at a fixed mean value of 342 MeV/c^2; and the background is fitted with a second-order polynomial.

Also, no signal is found at mass-difference spectrum of $M(\Lambda_c^+\gamma) - M(\Lambda_c^+)$, as shown in Figure 4.13. We used the exact-same fitting procedures as in the $M(\Lambda_c^+\pi^0)-M(\Lambda_c^+)$ case, except different Gaussian resolutions, which are 7.4 MeV/c^2 at mass difference 307 MeV/c^2 and 7.9 MeV/c^2 at mass difference 342 MeV/c^2.

The fitted yields and their projected upper limits are shown in Table 4.5. We conclude that we have observed no evidence of $\Lambda_c^+\pi^0$ or $\Lambda_c^+\gamma$ decays from Λ_{c1}^+.

4.6 Masses and Widths

4.6.1 Systematic Uncertainties

One major part of the systematic error of mass measurements is the fitting error, mostly from the uncertainty of the background shape or sometimes even the signal shape. To evaluate this error, we use many different fit types and check the variations of the mean value of the signal. For a particle with a considerably wide natural width, such as the Σ_c^{*++}, or a particle with an uncertain shape of the signal, such as the $\Lambda_{c1}^+(2593)$, the fitting error generally dominates the systematic uncertainty.

Since we measure the mass difference between the $\Lambda_c^+\pi\pi$ and the Λ_c^+ instead of measuring the Λ_{c1}^+ directly, most of the experimental uncertainties from the reconstruction of the Λ_c^+ cancel. As we checked, 3 MeV/c^2 change of the Λ_c^+ mass shifts the $M(\Lambda_c^+\pi^+\pi^-) - M(\Lambda_c^+)$ by no more than 0.01 MeV/c^2. So the systematic uncertainties other than the fitting errors mostly come from the measurement of the momenta and decay angles of the two extra pions. For charged pions, these errors are dominated by the uncertainties in the magnetic field normalization and the energy loss correction which is applied to the tracks traversing the beam pipe and the drift chambers. For π^0's, the errors come from the shower energy measurement by the crystal calorimeters.

To evaluate the systematic errors of mass-difference measurements caused by the independent charged pions with low momentum, we measured the mass difference $M(D^{*+}) - M(D^0)$ in decay $D^{*+} \to D^0\pi^+$ since the mass-difference measuring technique is the same as $M(\Lambda_c^+\pi^+\pi^-) - M(\Lambda_c^+)$ and the independent pion is soft. Our fitted result is 145.39$\pm$0.01 MeV/c^2, in excellent agreement with the PDG value, which is 145.397$\pm$0.030 MeV/c^2. We found that 0.2% momentum change of all charged tracks will shift the $M(D^{*+}) - M(D^0)$ by about 0.05 MeV/c^2, larger than the error of the PDG average. Therefore we believe 0.2% change in momentum is a reasonable amount to study the momentum scale in mass-different measurement with charged soft pions.

For the systematic errors caused by the measurement of the soft π^0's, similar to the charged ones, we check the photon energy scale by looking at the mass difference of $M(D^{*0})-M(D^0)$, and our fitted value agrees very well with the PDG value, which is 142.12$\pm$0.07 MeV/c^2. We think 1% energy change is a reasonable amount used for an energy-scale study since it shifts $M(D^{*0}) - M(D^0)$ by about 0.10 MeV/c^2.

In the study of $M(D^{*+}) - M(D^0)$ measurement, we find that mass difference is more sensitive to the systematic shifts of the position and angle parameters of tracks. However, the charged tracks are measured much more accurately. Our vertex constraint program would shift the track positions and angles by fair amounts. We find that calculating the mass difference by constraining the D^0 and the pion to be from the event vertex, gives up to 0.02 ± 0.01 MeV/c^2 mean-value difference, compared with the mean value of mass difference reconstructed without vertex constraint. This difference reasonably reflects the systematic error from the decay angle measurement.

The systematic error on the width measurement comes from two sources: the fitting error and the mass resolution of the detectors determined by Monte Carlo studies. The fitting error dominates the total error when the natural width of a particle is wide, and it can be evaluated by varying parameterizations of the background and the signal shapes. The detector resolution becomes important when it is close to, or bigger than the natural width, and its correctness can be checked by fitting the signals of other particles with well-known widths and comparing the results with corresponding Monte Carlo signals. As we tested, the CLEO Monte Carlo program does a very good job with tracks with medium-to-high momentum spectra, but for tracks with low-momentum spectra, it tends to overestimate the detector performance and therefore predicts a mass resolution with a lower value than the real resolution. But by the time this research work was performed, we are unable to make corrections, since it is very difficult to detect what the exact reason is and by exactly how much the Monte Carlo is wrong. So we have to be very careful and conservative with our estimates of the uncertainties on narrow-width measurements.

4.6.2 $\Lambda_{c1}^+(2625)$ Mass and Width Limit

The result presented on the $\Lambda_{c1}^+(2625)$ mass difference with the Λ_c^+, 341.80 ± 0.10 MeV/c^2 is our measured mean value by fitting the $\Lambda_c^+\pi^+\pi^-$ signal with a width-float single Gaussian. By fitting the $\Lambda_c^+\pi^0\pi^0$ signal, we obtained a value of 342.9 ± 0.9 MeV/c^2. We have also checked the fits to the $\Lambda_c^+\pi^+\pi^-$ signal using a double Gaussian, a bifurcated Gaussian, and a Breit-Wigner convoluted with a Gaussian, with variations of different shapes. All fitted means agree within 0.13 MeV/c^2.

In the momentum-scale study, we find that a 0.2% momentum change for all charged tracks shifts $M(\Lambda_{c1}^+(2625)) - M(\Lambda_c^+)$ by about 0.22 MeV/c^2. We find that the mass difference $M(\Lambda_{c1}^+(2625)) - M(\Lambda_c^+)$ shifts for about 0.2$\pm$0.1 MeV/c^2 if we do not constrain the Λ_c^+ and the two pions to be from a single vertex compared with constraining them into the main vertex. This proved that the uncertainty of the pion decay angle does not bring large systematic errors. We also compared $M(\overline{\Lambda_c^+}\pi^+\pi^-) - M(\overline{\Lambda_c^+})$ with $M(\Lambda_c^+\pi^+\pi^-) - M(\Lambda_c^+)$, and their mean values agree within statistical errors.

According to Table 4.1, the fitting error due to the background parameterization with the signal fitted by a single Gaussian is about $\pm$0.04 MeV/c^2, which is tiny compared with the uncertainty of the soft pion momentum measurement. Considering all these sources of errors, we conservatively estimate that the systematic uncertainty is 0.35 MeV/c^2.

With the width of 0.7$\pm$0.3 MeV/c^2 extracted from the Breit-Wigner convoluted with a Gaussian fit, considering that our Monte Carlo predicted resolution should not be larger than the actual one, we calculated the upper limit of the $\Lambda_{c1}^+(2625)$ width to be 1.4 MeV/c^2 at 90% confidence level.

Table 4.6: Measurements of the $\Lambda_{c1}^+(2625)$ mass and width limit.

Experiments	$[M(\Lambda_{c1}^+) - M(\Lambda_c^+)](\mathrm{MeV}/c^2)$	$\Gamma_{\Lambda_{c1}^+}(\mathrm{MeV}/c^2)$
E687[29]	340.4±0.6±0.3	
CLEO-II[30]	342.2±0.2±0.5	< 1.9
ARGUS[32]	342.1±0.5±0.5	< 3.2
CLEO-II(this)	341.80±0.10±0.35	< 1.4

Table 4.7: Measurements of $\Lambda_{c1}^+(2593)$ mass and width together with the mass resolutions in the corresponding experiments. All quantities are in units of MeV/c^2. Note that E687[31] fitted their signal using a single Gaussian and the fitted Gaussian width is consistent with that $\Lambda_{c1}^+(2593)$ has a zero intrinsic width.

Experiments	Resolution	$[M(\Lambda_{c1}^+) - M(\Lambda_c^+)](\mathrm{MeV}/c^2)$	$\Gamma_{\Lambda_{c1}^+}(\mathrm{MeV}/c^2)$
CLEO-II[30]	2.0	307.5±0.4±1.0	$3.9^{+1.4+2.0}_{-1.2-1.0}$
E687[31]	1.8	309.2±0.7±0.3	
ARGUS[32]	1.8	309.7±0.9±0.4	$2.9^{+2.9+1.8}_{-2.1-1.4}$
CLEO-II(this)	1.62	308.8±0.4±0.4	$4.7^{+1.3+1.4}_{-1.1-0.9}$

The results of mass difference with the Λ_c^+ and the upper limit of the width are listed in Table 4.6. A comparison with the previous experiment results is given in the table.

4.6.3 $\Lambda_{c1}^+(2593)$ Mass and Width

In Figure 4.1, we fit the $\Lambda_{c1}^+(2593) \to \Lambda_c^+\pi^+\pi^-$ signal in the same manner as the previous experiments: using a Breit-Wigner function convoluted with a Gaussian. The results of the mass and width are listed in Table 4.7, together with the measurements of previous experiments. Here the systematic errors are mostly fitting errors, evaluated based on Table 4.1.

Although our measurements agree with previous experiments, we doubt the results, and the most obvious reasons comes from the following facts: (1) $\Lambda_{c1}^+(2593)$

has a nearly 100% dominating decay channel, $\Sigma_c\pi$; (2) the combination of $\Sigma_c^0\pi^+$ (or $\Sigma_c^{++}\pi^-$) has a kinematic limit at the mass difference of about 307 MeV/c^2; (3) the fit to the $\Lambda_{c1}^+(2593)$ signal in Figure 4.1 is poor. Because of these and some other thoughts which will be stated later, we feel that using a full Breit-Wigner distribution to parameterize the $\Sigma_c^0\pi^+$ (or $\Sigma_c\pi^-$) decay very close to the kinematic threshold may not be correct. We will describe a new way to parameterize the signal in the next chapter, since the new method uses the Σ_c^{++} and Σ_c^0masses and widths.

4.7 Fragmentation Functions

As stated in Chapter 1, all quarks "fragment" into hadrons. The initially produced pair of hadron and anti-hadron should be expected to have more energy than the subsequent hadrons produced further in the decay chains. Each hadron, as it is produced, carry away a fraction, z, of total energy of the corresponding original quark. A fragmentation function ($\frac{dN}{dz}$, where N is the number of hadron produced from a type of specific physical process) proportional to the probability a hadron being produced in the interval of $[z,\ z + dz)$.

In e^+e^- annihilation experiments, measurement of the fragmentation functions of heavy quarks provides information about non-perturbative particle production in a variety of experimental environments. Many forms of functions have been suggested to describe the normalized momentum spectra for heavy quarks. Among those, the functional form given by Peterson et al.[33] is the most widely used. The Peterson function has form

$$\frac{dN}{dz} = \frac{1}{z[1 - (1/z) - \epsilon_P/(1-z)]^2},$$

where $z = (E + p_{||})_{hadron}/(E + p_Q)$, and $p_{||}$ is the longitudinal momentum and p_Q is the total momentum of the heavy quark. The quantity z is not experimentally accessible, and in CLEO experiments a close approximation is made by using the

Table 4.8: Efficiencies and productions of Λ_{c1}^+'s for different x_p's. The statistical errors on efficiencies are negligible.

	x_p	Efficiency(%)	Yield	Normalized Yield
$\Lambda_{c1}^+(2593)$	0.5-0.6	5.45	34 ± 16	0.13 ± 0.06
	0.6-0.7	6.44	74 ± 18	0.25 ± 0.06
	0.7-0.8	7.07	91 ± 18	0.27 ± 0.05
	0.8-0.9	7.11	71 ± 15	0.21 ± 0.05
	0.9-1.0	5.47	35 ± 11	0.14 ± 0.05
$\Lambda_{c1}^+(2625)$	0.5-0.6	5.63	114 ± 13	0.18 ± 0.02
	0.6-0.7	6.47	217 ± 16	0.30 ± 0.02
	0.7-0.8	7.08	214 ± 16	0.27 ± 0.02
	0.8-0.9	7.78	161 ± 14	0.19 ± 0.02
	0.9-1.0	7.48	48 ± 8	0.06 ± 0.01

scaling variable $x_p = p/p_{max}$, as defined for Λ_c^+ in the last chapter. ϵ_P physically represents the "hardness" of the heavy quark fragmentation. The smaller the value of ϵ_P is, the larger the portion of the total momentum the heavy quark carries.

Although the Peterson function agrees pretty well with the fragmentation of D^0 and D^{*+} measured in the experiments [34][35], there is no reason why any charmed particle momentum spectrum should follow an analytical curve of this type, as many particles are the decay results of excited states. However, the measurement of ϵ_P of Peterson function remains useful for comparing the spectra of different particles.

To measure the Peterson function of a particle, we fit the distribution of efficiency-corrected cross section at a different x_p range and extract the parameter ϵ_P. Table 4.8 shows the yields and Monte Carlo derived efficiencies at different x_p ranges. Also listed are the efficiency-corrected yields normalized to $x_p > 0.5$.

Figure 4.14 shows the $\frac{dN}{Ndx_p}$ (N is the efficiency-corrected number of Λ_{c1}^+'s for $x_p > 0.5$) distribution for the $\Lambda_{c1}^+(2593)$ and the $\Lambda_{c1}^+(2625)$ based on the efficiency-corrected yields listed in Table 4.8. Only statistical errors are shown in Table 4.8. Systematic errors are dominated by fitting procedures and are found to be a little

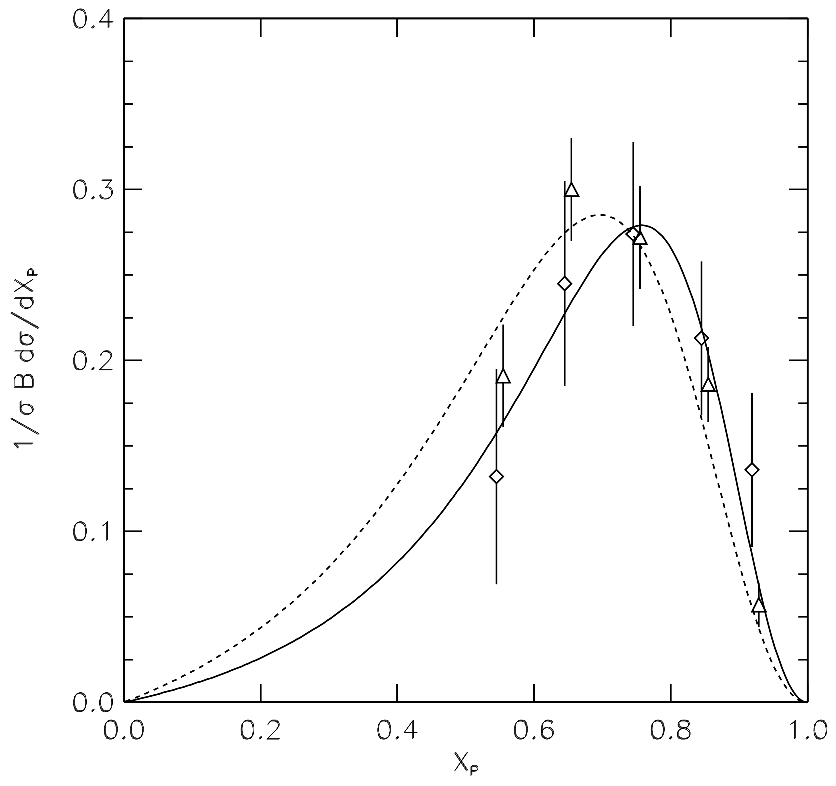

Figure 4.14: Normalized spectra of scaled momentum for Λ_{c1}^{+} samples. The data for the $\Lambda_{c1}^{+}(2593)$ (diamonds) and the $\Lambda_{c1}^{+}(2625)$ (triangles) are fitted to the Peterson function overlaid as the solid and dashed curves, respectively.

smaller than the statistical errors. The error bars shown in Figure 4.14 are the total errors. Also shown in the figure are the curves obtained by fitting the distributions by Peterson function. The measurement results are listed in Table 4.9 compared to the previous measurements. The measurements show that Λ_{c1}^{+} fragmentation at 10 GeV/c^2 is close to the fragmentation of D^{*+}, which was measured to have $\epsilon_P = 0.078 \pm 0.008$[36].

Table 4.9: Measurements of the fragmentation of Λ_{c1}^{+}'s using Peterson functions.

	Experiments	ϵ_P
$\Lambda_{c1}^{+}(2593)$	CLEO-II[30]	$0.057 \pm 0.023 \pm 0.016$
	ARGUS[32]	$0.069^{+0.065}_{-0.034} \pm 0.040$
	CLEO-II(this)	$0.064^{+0.021}_{-0.016}$
$\Lambda_{c1}^{+}(2625)$	ARGUS[28]	0.044 ± 0.018
	CLEO-II[30]	$0.065 \pm 0.016 \pm 0.013$
	CLEO-II (this)	$0.108^{+0.011}_{-0.009}$

4.8 Decay Ratios and Production Ratios

4.8.1 Systematic Errors on Yields and Efficiencies

To calculate the branching ratios and productions, the yields on the signals and the Monte Carlo derived efficiencies are used. Both bring systematic errors to the result.

The systematic errors on the yield of a signal come from the fitting procedures, including the signal and background parameterizations and the mass resolution determined by the Monte Carlo. As we explained in the last section, for the $\Sigma_c^*(2593) \to \Lambda_c^+ \pi^+ \pi^-$ signal, the systematic error is dominated by the uncertainty of the signal shape, and background parameterization is also a factor since the signal is just at the kinematic threshold. Based on Table 4.1 and other fit results, the fitting errors of the $\Sigma_c^*(2593) \to \Lambda_c^+ \pi^+ \pi^-$ yield are $\pm 15\%$ from the peak parameterization and $\pm 8\%$ from the background parameterization. As we tested, varying the Gaussian resolution by a reasonable amount only changes the $\Lambda_{c1}^{+}(2593)$ yield by 2%. We therefore estimate the fitting error on the $\Lambda_{c1}^{+}(2593) \to \Lambda_c^+ \pi^+ \pi^-$ yield to be $\pm 17\%$. For $\Lambda_{c1}^{+}(2625) \to \Lambda_c^+ \pi^+ \pi^-$, we have a clean signal at very low background, so the systematic error comes mostly from the Monte Carlo predicted resolution or, equivalently, the uncertain natural width of this state. We finally estimate that the fitting error of the $\Lambda_{c1}^{+}(2625)\to\Lambda_{c}^{+}\pi^{+}\pi^{-}$ yield is $^{+10}_{-2}\%$.

As the $\Lambda_{c1}^{+}\to\Lambda_{c}^{+}\pi^{0}\pi^{0}$ signals are poor, both statistical and fitting errors are very large. The fitting errors are mostly due to the uncertainty of the mass resolutions and the natural widths of the states. We expect the $\Lambda_{c1}^{+}(2593)\to\Lambda_{c}^{+}\pi^{0}\pi^{0}$ signal to be nearly a full Breit-Wigner convoluted with a Gaussian, since the kinematic threshold is at 301 MeV/c^2. The fitting errors are evaluated by reasonably varying the background parameterizations, the mass resolutions, and the widths of the states. From the results listed in Table 4.3 and some further tests, we estimate the fitting errors on $\Lambda_{c1}^{+}\to\Lambda_{c}^{+}\pi^{0}\pi^{0}$ signals are $\pm13\%$ for $\Lambda_{c1}^{+}(2593)$ and $^{+27}_{-9}\%$.

Since we measure the branching fractions by ratios, the systematic errors on the efficiencies of Λ_{c}^{+} reconstruction will cancel. Based on comprehensive studies by the CLEO collaboration, the systematic errors on efficiencies are 1% on finding one charged track and 5% on finding a π^0.

4.8.2 $\Lambda_{c}^{+}\pi^{0}\pi^{0}$, $\Lambda_{c}^{+}\pi^{0}$, and $\Lambda_{c}^{+}\gamma$ Decays

Since the yield of $\Lambda_{c1}^{+}\to\Lambda_{c}^{+}\pi^{+}\pi^{-}$ was the best measured for Λ_{c1}^{+}, the branching ratios we measured are all given relative to this decay mode.

This is the first time that the decay $\Lambda_{c1}^{+}\to\Lambda_{c}^{+}\pi^{0}\pi^{0}$ is reported. Of interest is the branching ratio $\mathcal{B}(\Lambda_{c}^{+}\pi^{0}\pi^{0})/\mathcal{B}(\Lambda_{c}^{+}\pi^{+}\pi^{-})$. If only isospin symmetry is applied on these states, this ratio should be 1/2.

Based on the discussion in the last subsection, we assign the systematic errors on $\mathcal{B}(\Lambda_{c}^{+}\pi^{0}\pi^{0})/\mathcal{B}(\Lambda_{c}^{+}\pi^{+}\pi^{-})$ to be $\pm26\%$ for the $\Lambda_{c1}^{+}(2593)$ and $^{+29}_{-16}\%$ for the $\Lambda_{c1}^{+}(2625)$. Table 4.10 gives the result calculated from the yield and the Monte Carlo predicted efficiency of each decay mode.

Table 4.10: Branching ratios of $\Lambda_c^+\pi^0\pi^0$ relative to $\Lambda_c^+\pi^+\pi^-$.

Particle	$\mathcal{B}(\Lambda_c^+\pi^0\pi^0)/\mathcal{B}(\Lambda_c^+\pi^+\pi^-)$
$\Lambda_{c1}^+(2593)$	$2.6\pm0.6\pm0.7$
$\Lambda_{c1}^+(2625)$	$1.0\pm0.3^{+0.3}_{-0.2}$

Table 4.11: Limits on branching ratios of $\Lambda_{c1}^+\to\Lambda_c^+\pi^0$ and $\Lambda_{c1}^+\to\Lambda_c^+\gamma$ relative to $\Lambda_{c1}^+\to\Lambda_c^+\pi^+\pi^-$. All values are evaluated at 90% *C.L.*

	Experiments	$\mathcal{B}(\Lambda_c^+\pi^0)/\mathcal{B}(\Lambda_c^+\pi^+\pi^-)$	$\mathcal{B}(\Lambda_c^+\gamma)/\mathcal{B}(\Lambda_c^+\pi^+\pi^-)$
$\Lambda_{c1}^+(2593)$	CLEO-II[30]	< 3.53	< 0.98
	CLEO-II(this)	< 1.1	< 3.0
$\Lambda_{c1}^+(2625)$	CLEO-II[30]	< 0.91	< 0.52
	CLEO-II(this)	< 0.45	< 0.36

The result on the $\Lambda_{c1}^+(2625)$ is larger than 0.5 but consistent with it, but the number on the $\Lambda_{c1}^+(2593)$ is significantly larger than 0.5. This can be explained by the phase-space suppression. The $\Lambda_{c1}^+(2593)$ mostly decays into $\Sigma_c\pi$ first then goes to the final state $\Lambda_c^+\pi\pi$. Since the mass of the $\Lambda_{c1}^+(2593)$ is just at the threshold to decay into a Σ_c plus a charged pion, so the decay $\Lambda_{c1}^+(2593) \to \Sigma_c^{++}\pi^-$ and $\Lambda_{c1}^+(2593) \to \Sigma_c^0\pi^+$ will be suppressed. On the other hand, isospin symmetry is not exact, so the π^0 mass is about 5 MeV/c^2 lower than charged ones, so the decay $\Lambda_{c1}^+(2593) \to \Sigma_c^+\pi^0$ is not suppressed by phase space. Thus for the $\Lambda_{c1}^+(2593)$, we expect $\mathcal{B}(\Lambda_{c1}^+ \to \Lambda_c^+\pi^0\pi^0)/\mathcal{B}(\Lambda_{c1}^+ \to \Lambda_c^+\pi^+\pi^-)$ to be higher than 1/2. We will discuss this more in the next chapter.

According to Table 4.5, taking the systematic errors on $\Lambda_c^+\pi^+\pi^-$ yields into account, we estimated the upper limits of $\Lambda_c^+\pi^0$ and $\Lambda_c^+\gamma$ decay ratios relative to $\Lambda_c^+\pi^+\pi^-$.

Table 4.12: Branching fractions of substructure Σ_c^+ in $\Lambda_{c1}^+ \to \Lambda_c^+ \pi^+ \pi^-$ decays. Note the Λ_{c1}^+ yields are smaller than the fitted results in Figure 4.1 since we measure the Σ_c yields from 304 MeV/c^2 to 314 MeV/c^2 of the $\Lambda_{c1}^+(2593)$ peak and from 337 MeV/c^2 to 347 MeV/c^2 of the $\Lambda_{c1}^+(2625)$ peak.

	Decay	Λ_{c1}^+ Yield	Σ_c Yield	f_{Σ_c}
$\Lambda_{c1}^+(2593)$	$\Sigma_c^{++}\pi^-$	$137 \pm 22 \pm 22$	$67 \pm 7 \pm 5$	$0.45 \pm 0.12 \pm 0.11$
	$\Sigma_c^0\pi^+$	$137 \pm 22 \pm 22$	$65 \pm 7 \pm 5$	$0.47 \pm 0.12 \pm 0.11$
	$\Sigma_c^+\pi^0$	$93 \pm 20 \pm 22$	$74 \pm 11 \pm 10$	$0.73 \pm 0.20 \pm 0.20$
$\Lambda_{c1}^+(2625)$	$\Sigma_c^{++}\pi^-$	$450 \pm 29 \pm 9$	$24 \pm 10 \pm 7$	$0.05 \pm 0.02 \pm 0.02$
	$\Sigma_c^0\pi^+$	$450 \pm 29 \pm 9$	$32 \pm 10 \pm 7$	$0.07 \pm 0.02 \pm 0.02$

Table 4.13: Comparison of measurements of branching ratios of Σ_c^{++} and Σ_c^0 substructures in $\Lambda_{c1}^+(2593) \to \Lambda_c^+ \pi^+ \pi^-$ decays from different experiments.

Experiment	$f_{\Sigma_c^{++}}$	$f_{\Sigma_c^0}$	$f_{(\Sigma_c^{++}+\Sigma_c^0)}$
E687[29]			> 0.51 90% $C.L.$
CLEO-II[30]	$0.36 \pm 0.09 \pm 0.09$	$0.42 \pm 0.09 \pm 0.09$	
ARGUS[32]	$0.37 \pm 0.12 \pm 0.13$	$0.29 \pm 0.10 \pm 0.11$	$0.66^{+0.13}_{-0.16} \pm 0.07$
CLEO-II(this)	$0.45 \pm 0.12 \pm 0.11$	$0.47 \pm 0.12 \pm 0.11$	

4.8.3 $\Sigma_c\pi$ Decays

The $\Lambda(1405)$, the spin 1/2 strange baryon, decays 100% to $\Sigma\pi$; and the spin 3/2 state $\Lambda(1520)$ decays to both $\Sigma\pi$ and $\Lambda\pi\pi$. We have observed the similar phenomenon for the $\Lambda_{c1}^+(2593)$ and the $\Lambda_{c1}^+(2625)$. Measurements of $f_{\Sigma_c} = \mathcal{B}(\Lambda_{c1}^+ \to \Sigma_c\pi)/\mathcal{B}(\Lambda_{c1}^+ \to \Lambda_c^+\pi\pi)$ for Σ_c^{++}, Σ_c^+, and Σ_c^0 are tabulated in Table 4.12. The systematic errors are dominated by the fitting errors on Σ_c yields on Λ_{c1}^+ signals and backgrounds.

Our observation is close to the previous CLEO measurements and consistent with the prediction that the $\Lambda_{c1}^+(2593)$ and $\Lambda_{c1}^+(2625)$ have J^P $1/2^-$ and $3/2^-$, respectively. The $\Lambda_{c1}^+(2593)$ can decay through both S-wave $\Sigma_c\pi$ and P-wave non-resonance $\Lambda_c^+\pi^+\pi^-$ channels, but the S-wave is preferred. However, angular mo-

Table 4.14: Comparison of measurements of branching ratios of Σ_c^{++} and Σ_c^0 substructures in $\Lambda_{c1}^+(2625) \to \Lambda_c^+\pi^+\pi^-$ decays from different experiments.

Experiment	$f_{\Sigma_c^{++}}$	$f_{\Sigma_c^0}$	$f_{(\Sigma_c^{++}+\Sigma_c^0)}$
ARGUS[28]			0.46 ± 0.14
E687[31]			< 0.36 90% $C.L.$
CLEO-II[30]	< 0.08 90% $C.L.$	< 0.07 90% $C.L.$	
CLEO-II(this)	$0.05 \pm 0.02 \pm 0.02$	$0.07 \pm 0.02 \pm 0.02$	

Table 4.15: Measurements of $\Lambda_{c1}^+ \to \Lambda_c^+\pi^+\pi^-$ production ratio relative to the total inclusive Λ_c^+ production.

	Experiment	$\frac{\sigma(\Lambda_{c1}^+ \to \Lambda_c^+\pi\pi)}{\sigma\Lambda_c^+}(\%)$
$\Lambda_{c1}^+(2593)$	CLEO[30]	$1.44 \pm 0.24 \pm 0.30$
	ARGUS[32]	$2.1^{+2.0}_{-1.1} \pm 1.1$
	CLEO(this)	$1.46^{+0.23+0.29}_{-0.22-0.29}$
$\Lambda_{c1}^+(2625)$	ARGUS[28]	$4.1 \pm 1.0 \pm 0.8$
	CLEO[30]	$3.51 \pm 0.34 \pm 0.28$
	CLEO(this)	$3.47 \pm 0.17^{+0.42}_{-0.27}$

mentum and parity conservations require $\Lambda_{c1}^+(2625) \to \Sigma_c\pi$ to be D-wave, so for the $\Lambda_{c1}^+(2625)$, the P-wave non-resonance $\Lambda_c^+\pi^+\pi^-$ is preferred and expected to have a smaller width.

4.8.4 Λ_{c1}^+ Production Ratios

Since we do not have good statistics with $\Lambda_c^+\pi^0\pi^0$ decay channels, we only present the $\Lambda_{c1}^+ \to \Lambda_c^+\pi^+\pi^-$ production as a fraction of Λ_c^+ baryons in the 10 GeV/c^2 e^+e^- annihilations. We have only measured the number of Λ_c^+'s and Λ_{c1}^+'s at $x_p(\Lambda_{c1}^+) > 0.5$, so we need to extrapolate the Peterson function to zero momentum. Fortunately, the two Λ_{c1}^+'s are fragmented very hard (only about 20% are fragmented below $x_p = 0.5$,) so the systematic errors from extrapolation are not very large. Based on our estimation, the sources and their values of systematic errors of the $\Lambda_{c1}^+(2593)$

are 15% for the peak parameterization, 8% for the background parameterization, and 10% for the $x_p = 0$ extrapolation. We estimate the total systematic error of the $\Lambda_{c1}^{+}(2593)$ production ratio measurement to be 20%. For the $\Lambda_{c1}^{+}(2625)$, the fitting errors are dominated by the uncertainty of the detector resolution. The total fitting error is estimated to be $^{+10}_{-2}$%, and the $x_p = 0$ extrapolation uncertainty is estimated to be 7%. Thus the total systematic error of the $\Lambda_{c1}^{+}(2625)$ production ratio measurement is estimated to be $^{+12}_{-8}$%. Our results are consistent with the previous experiments.

CHAPTER 5
STUDIES OF Σ_c AND Σ_c^* BARYONS

5.1 Introduction

The isospin triplet (Σ_c^{++}, Σ_c^{+}, Σ_c^{0}) is the charm counterpart of the Σ triplet with the two light quarks antisymmetric under exchange. The quark-model-predicted spin-parity J^P for the triplet is $1/2^+$ with the two light quarks in a $J^P = 1^+$ configuration. Although all three states have been observed by many experiments[37, 38, 39, 40, 41, 42, 43, 44], only the mass splittings and production ratios of the Σ_c^{++} and the Σ_c^{0} are reported, and no attempt has been made to measure their intrinsic widths. With a much larger data sample and the improved resolution of the CLEO-II detector, we are now able to measure the widths and production ratios of all three states.

The $3/2^+$ excitation of the Σ_c is the Σ_c^* triplet. CLEO has recently made the first observation of the Σ_c^{*++} and the Σ_c^{*0}[21]. Here we present an update of the measurements of these two particles and give evidence of the observation of the previously undiscovered Σ_c^{*+}.

In this chapter we first describe the observations and the fits of Σ_c and Σ_c^* signals in section 2.2, then in later sections we present the results of masses, widths, fragmentation functions, and production ratios of these particles. The physical significance of these measurements is also discussed. Finally, we describe a tentative measurement on the mass and width of the $\Lambda_{c1}^{+}(2593)$ in a new way, different from the methods used in previous experiments. We present this last because it requires the knowledge of the Σ_c mass and width.

5.2 Signals

All Σ_c's and Σ_c^*'s have one decay mode: $\Lambda_c^+\pi$. To obtain the signals, we combine each Λ_c^+ candidate with a pion, then measure the mass difference $M(\Lambda_c^+\pi) - M(\Lambda_c^+)$. The Λ_c^+ candidates are selected in the same way as we did in observing Λ_{c1}^+'s. To improve the signal to background ratio, a cut of $x_p > 0.5$ for $\Lambda_c^+\pi^\pm$ and a harder cut of $x_p > 0.6$ for $\Lambda_c^+\pi^0$ are used, since the $\Lambda_c^+\pi^0$ combination has much larger background and is more difficult to observe. Here x_p is defined in the same way as the x_p of the Λ_{c1}^+.

All charged tracks are used to be the independent $\pi^\pm$ candidates. In order to suppress the large background from these low-momentum charged pions, a cut on $cos(\theta_{dec})$ is used for $\Lambda_c^+\pi^\pm$ modes. θ_{dec} is defined to be the angle between the the pion momentum measured in the rest frame of the $\Lambda_c^+\pi^\pm$, and the direction of the $\Lambda_c^+\pi^\pm$ in the laboratory frame. According to Monte Carlo studies, θ_{dec} cut is more efficient than simply cutting on $\pi^\pm$ momentum to improve the signal to background ratio of the Σ_c^{*++} and the Σ_c^{*0}. We used $cos(\theta_{dec}) > -0.4$ which is the optimization from the $\Sigma_c^* \to \Sigma_c\pi$Monte Carlo studies.

When reconstructing $\Lambda_c^+\pi^\pm$ invariant mass, we constrain the Λ_c^+ and the independent pion to be from the event vertex, whose finding procedure was described in Chapter 3. This improves the mass resolution by roughly 5% for both the Σ_c^{++} and the Σ_c^0.

π^0 selection is described in Chapter 3. To suppress the large background, a π^0 momentum cut is needed. The Monte Carlo shows that a direct π^0 momentum cut is slightly more efficient than θ_{dec} cut for the Σ_c^{*+} observation and predicted that a 150 MeV/c cut gives largest signal to background ratio.

Sufficient Monte Carlo events have been generated. The mass differences we used are 167.87 MeV/c^2 for the Σ_c^{++}, 168.70 MeV/c^2 for the Σ_c^+, 167.30 MeV/c^2 for the

Σ_c^0, and 233 MeV/c^2 for all three Σ_c^*'s. We found that slightly varying the generated mass does not affect the Monte Carlo prediction for either width or efficiency. We first generated events with zero width to get the resolution of the signal; then after we extracted the width from real data, we generated events with the found width. Efficiencies are calculated using the latter Monte Carlo events. Using the same signal-fitting functions, the same natural width can be extracted from the Monte Carlo signal. All reconstructed mass differences in Monte Carlo shift by less than 0.03 MeV/c^2 relative to the generated ones.

5.2.1 $\Lambda_c^+\pi^\pm$

Figure 5.1 shows the mass-difference spectrum of $M(\Lambda_c^+\pi^\pm) - M(\Lambda_c^+)$. The clear peaks near 167 MeV/c^2 are Σ_c's, and wide bumps near 233 MeV/c^2 are Σ_c^*'s. In addition, we should expect broad enhancements below 205 MeV/c^2 which are $\Lambda_c^+\pi$ combinations from $\Lambda_{c1}^+(2625)\to\Lambda_c^+\pi^+\pi^-$ decays. It is because of this background that we did the Λ_{c1}^+ analysis before the $\Sigma_c^{(*)}$'s. It is calculated from $\Lambda_{c1}^+(2625)\to\Lambda_c^+\pi^+\pi^-$ signal and Monte Carlo predicted efficiencies that the excess from this source yields 728 events between 150 MeV/c^2 and 205 MeV/c^2.

In the same plots shown as solid histograms are the mass-difference spectra using the sidebands of the Λ_c^+signal. The sidebands are taken from the Λ_c^+ combinations in the mass-difference region 3 – 4.6 σ_M away from the known Λ_c^+ mass, 2286.7 MeV/c^2. No enhancement can be observed from these histograms, and they can be very well fitted by second-order polynomials.

In Figure 5.1, Σ_c and Σ_c^* signals are fitted with Breit-Wigners convoluted with a Gaussian with a fixed resolution width of 1.04 MeV/c^2 for the Σ_c or 1.53 MeV/c^2 for the Σ_c^*. The Gaussian resolutions are determined by the Monte Carlo studies. The broad excesses in the region below 205 MeV/c^2 are fitted by a double-threshold

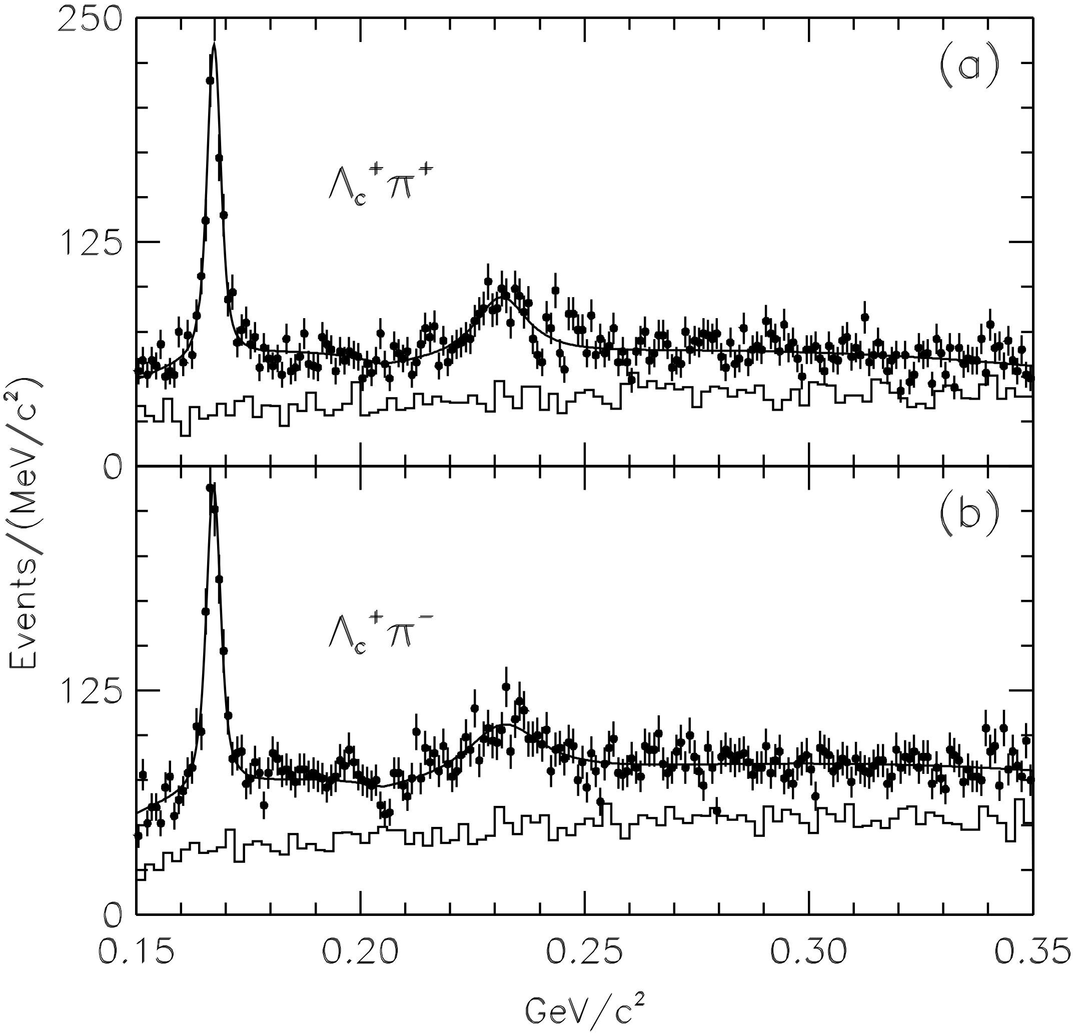

Figure 5.1: Mass difference for (a) $M(\Lambda_c^+\pi^+) - M(\Lambda_c^+)$, and (b) $M(\Lambda_c^+\pi^-) - M(\Lambda_c^+)$. The solid histogams are the spectra of $M(\Lambda_c^+\pi^\pm) - M(\Lambda_c^+$ "side"), where a "Λ_c^+ side" is from Λ_c^+ sidebands.

function with a fixed shape determined from $\Lambda_c^+\pi$ shapes in $\Lambda_{c1}^+(2625)\to\Lambda_c^+\pi^+\pi^-$ Monte Carlo (with thesholds at 139 MeV/c^2 and 205 MeV/c^2), and a fixed area, 728, determined by the efficiency-corrected $\Lambda_{c1}^+(2625)$ production. The rest of the background is fitted by a second-order polynomial with all parameters floated.

The results are sensitive to different fitting procedures. The extracted parameters from some variations of fits are listed in Table 5.1. Fit Type 1, which has the fitted curves shown in Figure 5.1, provides the presented results. Type 2 fixes the convoluted Gaussian width of the Σ_c's to be 1.25 MeV/c^2, widening the Monte Carlo predicted resolution of the Σ_c's by 20%. Type 3 reduces the area of the double-threshold function by 50%, and Type 4 enlarges it by 50%. Type 5 uses a third order of polynomial instead of the 2nd order to fit the background. Type 6 fits the region in the plot below 200 MeV/c^c and Type 7 fits the region above 200 MeV/c^2. Type 8 uses 4 MeV/c^2 bin size instead of 1 MeV/c^2. The statistical errors given in the table are only for fit Type 1 since the errors for the other types are roughly the same.

Besides the fit types listed in Table 5.1, many other fitting procedures are used, such as varying and floating the parameters of the double-threshold function (we found that our results are much more sensitive to the area than the actual shape of the double-threshold function), using higher-order Chebychev polynomials to fit the entire background, using a single Gaussian, a double-Gaussian, or a bifurcated Gaussian to fit the peaks to check the variation of the means, fitting the two peaks separately in different mass-difference ranges and with different backgrounds. The measured parameters from all reasonable fits are within the range listed in Table 5.1. Also, we measured the same parameters with different σ_M cuts around the Λ_c^+ mass and found that the signals we have are consistently associated with the Λ_c^+.

To study the fragmentation function of these particles, we divide the 0.5 – 1.0 x_p range into 4 bins and add an extra bin from 0.4 to 0.5, then fit each mass-difference

Table 5.1: The yield (Y), mass difference ΔM, and extracted width Γ measured from various fits to $\Lambda_c^+\pi^\pm$.

	Fit Type	Y	$\Delta M(\mathrm{MeV}/c^2)$	$\Gamma(\mathrm{MeV}/c^2)$
Σ_c^{++}	1	880^{+60}_{-58}	167.34 ± 0.10	2.1 ± 0.3
	2	845	167.35	1.7
	3	915	167.35	2.3
	4	851	167.33	2.1
	5	875	167.34	2.1
	6	908	167.36	2.2
Σ_c^0	1	895^{+64}_{-62}	167.24 ± 0.11	$2.3^{+0.4}_{-0.3}$
	2	870	167.23	1.9
	3	942	167.24	2.1
	4	925	167.22	2.0
	5	879	167.22	2.3
	6	895	167.21	2.3
Σ_c^{*++}	1	765^{+147}_{-123}	231.4 ± 0.8	14 ± 3
	2	825	231.4	15
	3	649	231.6	12
	4	931	231.2	16
	5	829	231.4	15
	7	715	231.4	13
	8	821	231.7	15
Σ_c^{*0}	1	1015^{+242}_{-195}	231.9 ± 1.2	20^{+5}_{-4}
	2	769	232.8	16
	3	811	233.1	16
	4	1249	231.6	24
	5	822	232.7	17
	7	1193	231.9	23
	8	1116	231.7	22

Table 5.2: The yield (Y), efficiency, and normalized production of $\Lambda_c^+\pi^\pm$ events for different x_p cuts.

	x_p	Y	Efficiency (%)	Normalized Production
Σ_c^{++}	0.4 - 1.0	1094 ± 54	6.64	16988 ± 813
	0.4 - 0.5	211 ± 29	6.57	3212 ± 441
	0.5 - 0.6	246 ± 27	6.61	3722 ± 408
	0.6 - 0.7	295 ± 26	6.69	4410 ± 389
	0.7 - 0.8	232 ± 23	6.64	3493 ± 364
	0.8 - 1.0	137 ± 16	6.42	2134 ± 249
Σ_c^0	0.4 - 1.0	1109 ± 55	6.64	16702 ± 828
	0.4 - 0.5	214 ± 28	6.57	3257 ± 426
	0.5 - 0.6	241 ± 27	6.61	3645 ± 318
	0.6 - 0.7	289 ± 27	6.69	4319 ± 403
	0.7 - 0.8	209 ± 23	6.64	3148 ± 346
	0.8 - 1.0	120 ± 14	6.42	1869 ± 218
Σ_c^{*++}	0.4 - 1.0	1097 ± 121	7.06	15538 ± 1714
	0.4 - 0.5	244 ± 67	7.07	3451 ± 948
	0.5 - 0.6	321 ± 55	7.23	4440 ± 761
	0.6 - 0.7	282 ± 46	7.09	3977 ± 649
	0.7 - 0.8	155 ± 33	6.70	2313 ± 493
	0.8 - 1.0	70 ± 15	6.88	1017 ± 218
Σ_c^{*0}	0.4 - 1.0	1348 ± 189	7.06	19093 ± 2677
	0.4 - 0.5	311 ± 79	7.07	4399 ± 1117
	0.5 - 0.6	384 ± 71	7.23	5311 ± 982
	0.6 - 0.7	277 ± 60	7.09	3907 ± 846
	0.7 - 0.8	227 ± 47	6.70	3388 ± 701
	0.8 - 1.0	134 ± 34	6.88	1948 ± 494

spectrum individually. Each Gaussian width is fixed by the predicted resolution from corresponding Monte Carlo events. If we float the masses and the Breit-Wigner widths of all signals, both mass and width of the same particle vary considerably due to poor statistics. However, if we fix all the masses to the measured values in the 0.5 – 1.0 x_p range, all widths vary around our presented values, measured in the 0.5 – 1.0 x_p range, within statistical errors. If we fix all the widths to be our presented values, Σ_c masses vary within 0.16 MeV around our presented masses with statistical errors about ± 0.20 MeV/c^2, and Σ_c^* masses vary within $^{+3.1}_{-3.5}$ MeV/c^2 around our presented masses with statistical errors of about ± 2 MeV/c^2. Table 5.2 listed the yields and efficiency-corrected productions with all widths fixed. Each efficiency is determined by the Monte Carlo, and its error is within 0.01%.

We also fitted the mass-difference spectra with variations of the θ_{dec} cut and, almost equivalently, of the $\pi^\pm$ momentum cuts to see if there are any systematic changes in masses and widths. We find the signals of the data are consistent with Monte Carlo studies, and all extracted parameters agree within statistical errors.

5.2.2 $\Lambda_c^+\pi^0$

For $\Lambda_c^+\pi^0$ combinations, π^0 momentum cut is very important to reduce the background. The 150 MeV/c^2 cut we used is the prediction from the Monte Carlo. Table 5.3 displays signal-to-background ratios of $\Lambda_c^+\pi^0$ combinations for different π^0 momentum cuts. In the table S's are the fitted areas of the Σ_c or the Σ_c^* from the Monte Carlo plots; B's are the size of the background from the Σ_c or Σ_c^* sidebands from $\Lambda_c^+\pi^0$ combinations of real data.

The plot of mass difference $M(\Lambda_c^+\pi^0) - M(\Lambda_c^+)$ is shown in Figure 5.2. The two signals and the background are fitted by the same four functions used in Figure 5.1. The convoluted Gaussian widths are determined by Monte Carlo stud-

Table 5.3: Signal versus background of $\Lambda_c^+\pi^0$ combinations for different π^0 momentum cuts. In the table S is the fitted area of the Σ_c or the Σ_c^* signal from the Monte Carlo events; B is the area of the background (taken from the Σ_c or Σ_c^* sidebands) from $\Lambda_c^+\pi^0$ combinations of real data.

$P(\pi^0)$ (GeV)	$S_{\Sigma_c^+}$	$S_{\Sigma_c^{*+}}$	$B_{\Sigma_c^+}$	$B_{\Sigma_c^{*+}}$	$S_{\Sigma_c^+}/\sqrt{B_{\Sigma_c^+}}$	$S_{\Sigma_c^{*+}}/\sqrt{B_{\Sigma_c^{*+}}}$
0.05	2877	2610	5448	9977	39.0	26.1
0.10	2873	2526	5376	7760	39.3	28.7
0.15	2734	2398	4685	6068	40.0	30.8
0.20	2363	2010	3676	4685	39.0	30.7
0.25	1929	1694	2632	3654	37.6	28.0

ies: 1.92 MeV/c^2 for the Σ_c^+ at 167 MeV/c^2 and 3.71 MeV/c^2 for the Σ_c^{*+} at 229 MeV/c^2. The shape of the double-threshold function is determined by $\Lambda_c^+\pi^0$ shape in the $\Lambda_{c1}^+(2625)\rightarrow\Lambda_c^+\pi^0\pi^0$ Monte Carlo, and the two thresholds are fixed to be at 135 MeV/c^2 and 216 MeV/c^2. The area of the double-threshold function is the number of $\Lambda_{c1}^+(2625)\rightarrow\Lambda_c^+\pi^0\pi^0$ feed-down, and it is calculated (from the efficiency-corrected $\Lambda_{c1}^+(2625)\rightarrow\Lambda_c^+\pi^0\pi^0$) to be 216. The solid histogram in the plot shows the spectrum of the combination of π^0's and the Λ_c^+ sidebands, taken from the same mass-difference region (3 – 4.6 σ_M) as in the $\Lambda_c^+\pi^\pm$ case.

Fitting procedures affect the extracted parameters. Many different fits were performed to investigate the stabilities of the signals using different fitting methods. Table 5.4 shows some results from different fit types. Fit Type 1 is the procedure just described whose fitted curve is shown in Figure 5.2, and the fitted results are our presented values. Type 2 fixes the width of the convoluted Gaussian of the Σ_c^+ peak to be 2.20 MeV/c^c, 15% larger than the Monte Carlo predicted resolution; and Type 3 fixes it to be 2.50 MeV/c^2, 30% larger than the Monte Carlo value. We found that the fitted Γ of the Σ_c^{*+} is insensitive to the change of the convoluted Gaussian width. In fit Type 4 the double-threshold function representing the feed-down of $\Lambda_{c1}^+(2625)$ is taken away; and in Type 5 its area is enlarged by 100%. Type 6 uses a

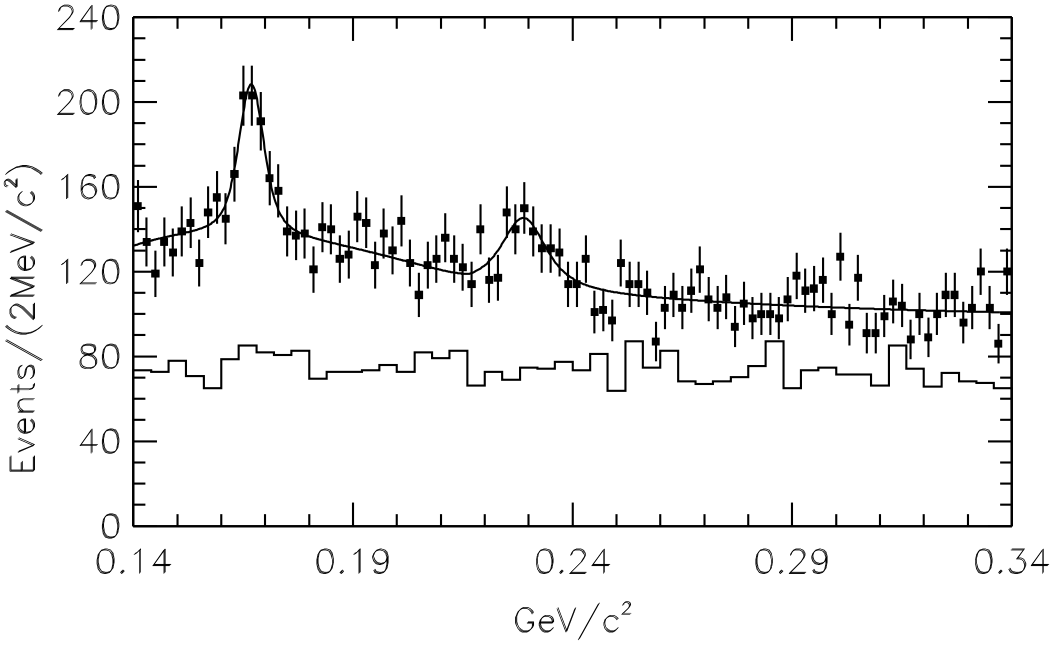

Figure 5.2: Mass difference $M(\Lambda_c^+\pi^0) - M(\Lambda_c^+)$.

Table 5.4: The yield Y, mass difference ΔM, and extracted width Γ measured from various fits to the $\Lambda_c^+\pi^0$ signal.

	Fit Type	Y	$\Delta M(\mathrm{MeV}/c^2)$	$\Gamma(\mathrm{MeV}/c^2)$
Σ_c^+	1	367^{+85}_{-72}	166.9 ± 0.5	$4.5^{+2.1}_{-1.7}$
	2	356	166.9	3.9
	3	343	167.0	3.2
	4	415	167.0	5.4
	5	329	166.8	3.9
	6	337	166.8	4.0
	7	376	166.9	4.7
	9	352	166.9	3.7
	10	355	167.1	4.5
Σ_c^{*+}	1	236^{+109}_{-79}	229.2 ± 1.3	$5.3^{+6.4}_{-4.6}$
	2	224	229.2	5.2
	3	231	229.2	5.1
	4	190	229.2	3.3
	5	297	229.0	7.7
	6	203	229.4	3.7
	8	215	229.5	4.2
	9	238	229.3	5.5
	10	217	229.4	4.1

third-order polynomial instead of the second order in Type 1 to fit the background. Fit Type 7 and 8 try to eliminate the influence of one signal to the other. Type 7 excludes the region from 200 MeV/c^2 to 250 MeV/c^2 so only the Σ_c^+ signal is fitted. Type 8 fits the region above 200 MeV/c^2 so the Σ_c^+ signal is excluded. All the above fit types fit the spectrum with 2 MeV/c^2 bin size. Types 9 and 10 are the fits to plots with the bin size 1 MeV/c^2 and 4 MeV/c^2, respectively. The statistical errors for all fit types are roughly the same as the ones given in Type 1.

As in the $\Lambda_c^+\pi^\pm$ cases, we have used more variations of fits, and the variations on all measured parameters do not exceed the ranges of those listed values in Table 5.4.

It is worth mentioning that although the yield of the Σ_c^{*+}, which is 236^{+109}_{-79}, does not seem statistically significant, if we fit the signal by a single Gaussian with floated width, a 162^{+50}_{-45} signal is obtained with a mean value of 229.4 ± 1.4 MeV/c^2. We also notice that if we fit the mass-difference region from 190 MeV/c^2 to 290 MeV/c^2 (Σ_c^+ signal only) in Figure 5.2, the χ^2 obtained in our best fit is 31.5 for 44 *d.o.f.* (degrees of freedom), whereas in a fit with no signal allowed, the χ^2 rises to 49.5. The fit strongly supports the existence of a signal, and this represents the first evidence for the particle Σ_c^{*+}.

When we vary π^0 momentum cuts from 50 MeV/c to 250 MeV/c, we found that the mass difference shifts from 166.1 to 166.9 MeV/c^2 for the Σ_c^+ and from 233.5 to 229.7 MeV/c for the Σ_c^{*+}; and the extracted width varies from 3.4 to 4.8 MeV/c^2 for the Σ_c and from 5.0 to 8.4 MeV/c^2. Also, for the yield in the Σ_c^+ signal, the data agrees fairly well with the Monte Carlo. Although we have obtained the best statistical significance for the Σ_c^{*+} signal at 200 MeV/$c\pi^0$ momentum cut, the Monte Carlo optimized 150 MeV/c cut is actually used. To prove the consistency of our signal with Λ_c^+ samples, we looked at the signal with different σ_M cuts around the Λ_c^+ mass, and the measured masses, widths, and yields agree very well.

Table 5.5: The yield (Y), mass difference (ΔM), efficiency, and normalized production of the Σ_c^+ for different x_p cuts. Both M and Γ are in units of MeV/c^2.

x_p	ΔM	Y	Efficiency(%)	Y/Efficiency
0.5 - 1.0	167.1 ± 0.4	559 ± 60	2.77	20181 ± 2166
0.5 - 0.6	167.4 ± 0.7	208 ± 38	2.45	8490 ± 1551
0.6 - 0.7	167.2 ± 0.8	168 ± 34	2.82	5957 ± 1206
0.7 - 0.8	166.4 ± 0.7	182 ± 28	2.88	6319 ± 972
0.8 - 1.0	168.2 ± 1.3	72 ± 18	2.85	2526 ± 632

We tabulated the masses and the yields of the Σ_c^+ for different x_p ranges in Table 5.5. For the Σ_c^* signal, lacking statistics makes it very difficult and not quite meaningful to fit the mass-difference spectra at different x_p bins. The numbers in the table are all obtained by fixing the Breit-Wigner width to be 4.5 MeV/c^2 and fixing the width of the convoluted Gaussian to be the number obtained by Monte Carlo, ranging from 1.80 MeV/c^2 to 2.32 MeV/c^2. All statistical errors on efficiencies are no larger than 0.01%.

5.3 Masses

The masses we present are the mean values of the Breit-Wigner convoluted with a Gaussian. We have checked that fitting with a single Gaussian, a double Gaussian, or a bifurcated Gaussian (constraining the two width difference no larger than 15%) gives the mean value within 1 σ of the statistical error.

As discussed in the last chapter, the uncertainties in the magnetic field normalization and the energy-loss correction applied to the charged soft pions, or the uncertainty of the shower energy calibration applied to the neutral pions, bring systematic errors on mass measurement for $M(\Lambda_c^+\pi) - M(\Lambda_c^+)$. We find that 0.2% change of charged track momentum shifts $M(\Sigma_c) - M(\Lambda_c^+)$ by about 0.10 MeV/c^2 and $M(\Sigma_c^*) - M(\Lambda_c^+)$ by about 0.30 MeV/c^2, 1.0% change of photon energy shifts

Table 5.6: Measurements of mass differences between Σ_c's and the Λ_c^+. All numbers are in units of MeV/c^2.

Experiment	$M(\Sigma_c^{++}) - M(\Lambda_c^+)$	$M(\Sigma_c^{+}) - M(\Lambda_c^+)$	$M(\Sigma_c^{0}) - M(\Lambda_c^+)$
ARGUS[41]	$168.2 \pm 0.5 \pm 1.6$		$167.0 \pm 0.5 \pm 1.6$
CLEO-II[42, 43]	$168.2 \pm 0.3 \pm 0.2$	$168.5 \pm 0.4 \pm 0.2$	$167.1 \pm 0.3 \pm 0.2$
E687[45]	$167.6 \pm 0.6 \pm 0.6$		$166.6 \pm 0.5 \pm 0.6$
E791[44]	$167.8 \pm 0.3 \pm 0.2$		$167.4 \pm 0.3 \pm 0.2$
CLEO-II(This)	$167.3 \pm 0.1 \pm 0.2$	$166.9 \pm 0.5 \pm 0.3$	$167.2 \pm 0.1 \pm 0.2$

$M(\Sigma_c^+) - M(\Lambda_c^+)$ by about 0.13 MeV/c^2 and $M(\Sigma_c^{*+}) - M(\Lambda_c^+)$ by about 0.38 MeV/c^2.

Reconstructing mass $M(\Lambda_c^+\pi)$ using vertex constraint on the Λ_c^+ and the independent pion shifts $M(\Sigma_c) - M(\Lambda_c^+)$ by about 0.05±0.10 MeV/c^2. For the Σ_c, $M(\Lambda_c^+\pi^+) - M(\Lambda_c^+)$ and $M(\overline{\Lambda_c^+}\pi^+) - M(\Lambda_c^+)$ are about 0.2±0.10 MeV/c^2 higher than $M(\overline{\Lambda_c^+}\pi^-) - M(\Lambda_c^+)$ and $M(\Lambda_c^+\pi^-) - M(\Lambda_c^+)$, respectively.

For Σ_c's which have clean signals and narrow widths, fitting errors are less important than the errors from other sources, but for Σ_c^*'s which have very wide widths, fitting errors dominate the systematic uncertainties.

Based on Table 5.1, Table 5.4, and more other fitting results of $M(\Lambda_c^+\pi) - M(\Lambda_c^+)$, we conclude that the systematic errors due to fitting procedures are ±0.03 MeV/c^2 for both $M(\Sigma_c^{++}) - M(\Lambda_c^+)$ and $M(\Sigma_c^0) - M(\Lambda_c^+)$, ±0.2 MeV/$c^2$ for $M(\Sigma_c^+) - M(\Lambda_c^+)$, $^{+0.8}_{-0.5}$ MeV/c^2 for $M(\Sigma_c^{*++}) - M(\Lambda_c^+)$, ±0.5 MeV/$c^2$ for $M(\Sigma_c^{*+}) - M(\Lambda_c^+)$, $^{+1.3}_{-0.7}$ MeV/c^2 for $M(\Sigma_c^{*++}) - M(\Lambda_c^+)$.

To be conservative, we finally assign the total systematic errors to be 0.2 MeV/c^2 for $M(\Sigma_c^{++}) - M(\Lambda_c^+)$ and $M(\Sigma_c^0) - M(\Lambda_c^+)$, 0.3 MeV/$c^2$ for $M(\Sigma_c^+) - M(\Lambda_c^+)$, $^{+0.9}_{-0.6}$ MeV/c^2 for $M(\Sigma_c^{*++}) - M(\Lambda_c^+)$, ±0.7 MeV/$c^2$ for $M(\Sigma_c^{*+}) - M(\Lambda_c^+)$, $^{+1.3}_{-0.8}$ MeV/c^2 for $M(\Sigma_c^{*++}) - M(\Lambda_c^+)$.

Table 5.7: Measurements of mass splitting of the Σ_c triplet and comparison with theoretical calculations. All numbers are in units of MeV/c^2.

		$M(\Sigma_c^{++}) - M(\Sigma_c^0)$	$M(\Sigma_c^{+}) - M(\Sigma_c^0)$
Theory	Chan[46]	0.4	-0.7
	Hwang[47]	3.0	-0.5
	Wright[48]	-1.4	-2.0
	Deshpande[49]	-3.3	-2.5
	Sinha[50]	1.5	-0.3
	Capstick[51]	1.4	-0.2
Experiments	ARGUS[41]	$1.2 \pm 0.7 \pm 0.3$	
	E791[44]	$0.38 \pm 0.40 \pm 0.15$	
	CLEO-II[42, 43]	$1.1 \pm 0.4 \pm 0.1$	$1.4 \pm 0.5 \pm 0.3$
	CLEO-II(this)	$0.1 \pm 0.1 \pm 0.1$	$-0.3 \pm 0.5 \pm 0.1$

Table 5.6 summarizes the measurements of the Σ_c masses from different experiments. Note that we have larger errors on $M(\Sigma_c^+) - M(\Lambda_c^+)$ than the previous CLEO measurement. This is because we have fitted the mass difference with a floated natural width (Breit-Wigner function) instead of the assumed negligible natural width in the previous works. For Σ_c^{++} and Σ_c^0 mass differences, we have better statistical errors due to the significant improvement of the resolution of soft charged pions.

The experimental measurements of mass splitting among the three Σ_c states together with some theoretical predictions from these models are listed in Table 5.7. Our $M(\Sigma_c^0)$ result is in vary good agreement with previous results. Our $M(\Sigma_c^{++})$ result is lower than the average of the previous results, but nearly equal to $M(\Sigma_c^0)$. Only CLEO has observed Σ_c^+, and our measured mass is obviously lower than the previous result.

Theoretical predictions about Σ_c isospin mass splitting range from -6.5 MeV/c^2 to $+18.0$ MeV/c^2. Table 5.7 lists the predictions which are close to our measurements. These models have considered the following effect: (1) the intrinsic mass difference between the u and d quarks; (2) electromagnetic interactions consisting

Table 5.8: Measurements of mass difference between Σ_c^*'s and the Λ_c^+, in unit of MeV/c^2.

Experiment	$M(\Sigma_c^{*++}) - M(\Lambda_c^+)$	$M(\Sigma_c^{*+}) - M(\Lambda_c^+)$	$M(\Sigma_c^{*0}) - M(\Lambda_c^+)$
CLEO-II[21]	$234.5 \pm 1.1 \pm 0.8$		$232.6 \pm 1.0 \pm 0.8$
CLEO-II(this)	$231.4 \pm 0.8^{+0.9}_{-0.5}$	$229.2 \pm 1.3 \pm 0.5$	$231.9 \pm 1.2^{+1.2}_{-0.7}$

of Coulomb interactions between every pair of quarks and spin-spin interactions; (3) contributions of QCD effects (in some of models).

CLEO is the only experiment which has reported the measurements on Σ_c^*'s. Table 5.8 compared the mass differences measured in this work with the recent reported values. Both measurements used the same datasets, but the latter used the recompressed data in which the charged tracks are processed differently and supposed to be measured better. In this work we have roughly the same errors since we could not take much advantage of better charged track resolution due to the large natural width of these states. We have strongly confirmed the existence of the Σ_c^{*++} and the Σ_c^{*0} and shown the first evidence of the existence of the Σ_c^{*+}.

5.4 Widths

As discussed in Chapter 3, the measurement of a particle's natural width depends on the Monte Carlo simulated resolution of the detector, especially when the width is narrow. Also as stated in Chapter 3, we know that the real detector resolution of the $M(D^{*+}) - M(D^0)$ measurement is, in the worst case, 15% larger than the Monte Carlo predicted one. We also found that the $\Lambda_{c1}^+(2625)$ actual resolution is likely bigger, and can be up to 10% larger than the Monte Carlo predicted resolution if $\Lambda_{c1}^+(2625)$ intrinsic width is negligible. Since the momentum spectrum on the soft charged pion for the Σ_c^{++} or the Σ_c^0 is similar to the two independent pions in the $\Lambda_{c1}^+(2625) \rightarrow \Lambda_c^+ \pi^+ \pi^-$ decay, we should expect that the Monte Carlo predicted

Table 5.9: Measurements of widths of Σ_c's.

	$\Gamma(\Sigma_c^{++})(\mathrm{MeV}/c^2)$	$\Gamma(\Sigma_c^{+})(\mathrm{MeV}/c^2)$	$\Gamma(\Sigma_c^{0})(\mathrm{MeV}/c^2)$
Fitted Value	$2.1 \pm 0.3^{+0.3}_{-0.5}$	$4.5^{+2.1+1.0}_{-1.7-1.5}$	$2.3^{+0.4+0.3}_{-0.3-0.5}$
Limit	> 0.6 (90% $C.L.$)		> 0.7 (90% $C.L.$)

resolution on $M(\Lambda_c^+\pi^\pm) - M(\Lambda_c^+)$ may be lower than the actual one by roughly the same amount and take this into account when we evaluate the systematic errors.

The Monte Carlo resolution on both the Σ_c^{++} and the Σ_c^0 is 1.04 MeV/c^2. To make sure that we have seen the finite widths of these states, we fit the $M(\Lambda_c^+\pi^+) - M(\Lambda_c^+)$ signal, which is slightly narrower than $M(\Lambda_c^+\pi^-) - M(\Lambda_c^+)$ signal, by a width-floated single Gaussian. The fitted widths range from 1.81 to 1.95 MeV/c^2, depending on how the background is parameterized. We get obviously bad fits if we fit the signal by a single Gaussian with a fixed width lower than 1.6 MeV/c^2. We have also tried to fit the signal by a double-Gaussian, with a fixed shape determined by Monte Carlo, and could only get reasonable fits by enlarging the Monte Carlo width by at least 50%. Therefore we believe that our detector resolution, which should not be poorer than 1.35 MeV/c^2, has enabled us to extract finite widths of Σ_c's from the fits.

Even conservatively, we are very certain that the detector resolution must be better than 1.35 MeV/c^2, which is 30% worse than the Monte Carlo predicted resolution. Then we looked at the χ^2 distribution of fits to the mass difference using different Breit-Wigner widths convoluted with a single Gaussian with fixed 1.35 MeV/c^2 width. It can be concluded that at 90% confidence level, $\Gamma(\Sigma_c^{++}) > 0.6$ MeV/c^2 and $\Gamma(\Sigma_c^0) > 0.7$ MeV/c^2.

Table 5.9 gives the results on Σ_c widths measurements. The fitted values and their errors are based on Table 5.1 and Table 5.4. Uncertainties of the detector resolution dominate the systematic errors. No other experiments has reported Σ_c

Table 5.10: Measurements of widths of Σ_c^*'s.

Experiment	$\Gamma(\Sigma_c^{*++})$	$\Gamma(\Sigma_c^{*+})$	$\Gamma(\Sigma_c^{*0})$
CLEO-II[21]	$17.9^{+3.8}_{-3.2} \pm 4.0$		$13.0^{+3.7}_{-3.0} \pm 4.0$
CLEO-II(this)	$14 \pm 3 \pm 3$	5^{+6+3}_{-5-2}	$20^{+5}_{-4} \pm 5$

Table 5.11: CLEO Measurements of fragmentation functions using the Peterson function for the Σ_c and the Σ_c^*.

Particles	ϵ_P
Σ_c^{++}	$0.28^{+0.05}_{-0.04}$
Σ_c^{+}	$0.25^{+0.18}_{-0.09}$
Σ_c^{0}	$0.29^{+0.05}_{-0.04}$
$\Sigma_c^{++} + \Sigma_c^0$	0.28 ± 0.03
Σ_cAverage	0.28 ± 0.03
Σ_c^{*++}	$0.36^{+0.17}_{-0.11}$
Σ_c^{*0}	$0.32^{+0.20}_{-0.11}$
$\Sigma_c^{*++} + \Sigma_c^{*0}$	$0.34^{+0.13}_{-0.09}$
Σ_c^{*++} Σ_c^{*0} Average	$0.33^{+0.11}_{-0.07}$

widths measurements, and all previously published Σ_c observations have the detector resolution no better than 2 MeV/c^2.

Our results of the Σ_c^* widths, together with the CLEO previously measured values, are tabulated in Table 5.10. The new results are consistent with the previous ones. As we explained in the last section, this measurement cannot do much better than the previous work with Σ_c^*. The Σ_c^{*+} width we first measured is not very meaningful, since the signal needs to be further confirmed and the error is too large.

5.5 Fragmentation Functions

Figure 5.3 and Figure 5.4 show the $\frac{dN}{Ndx_p}$ distributions for the Σ_c and the Σ_c^*. The yields in the figures are the numbers in Table 5.2 and Table 5.5 with the correct systematic errors added, and they are normalized to the total yield in the 0.4 – 1.0

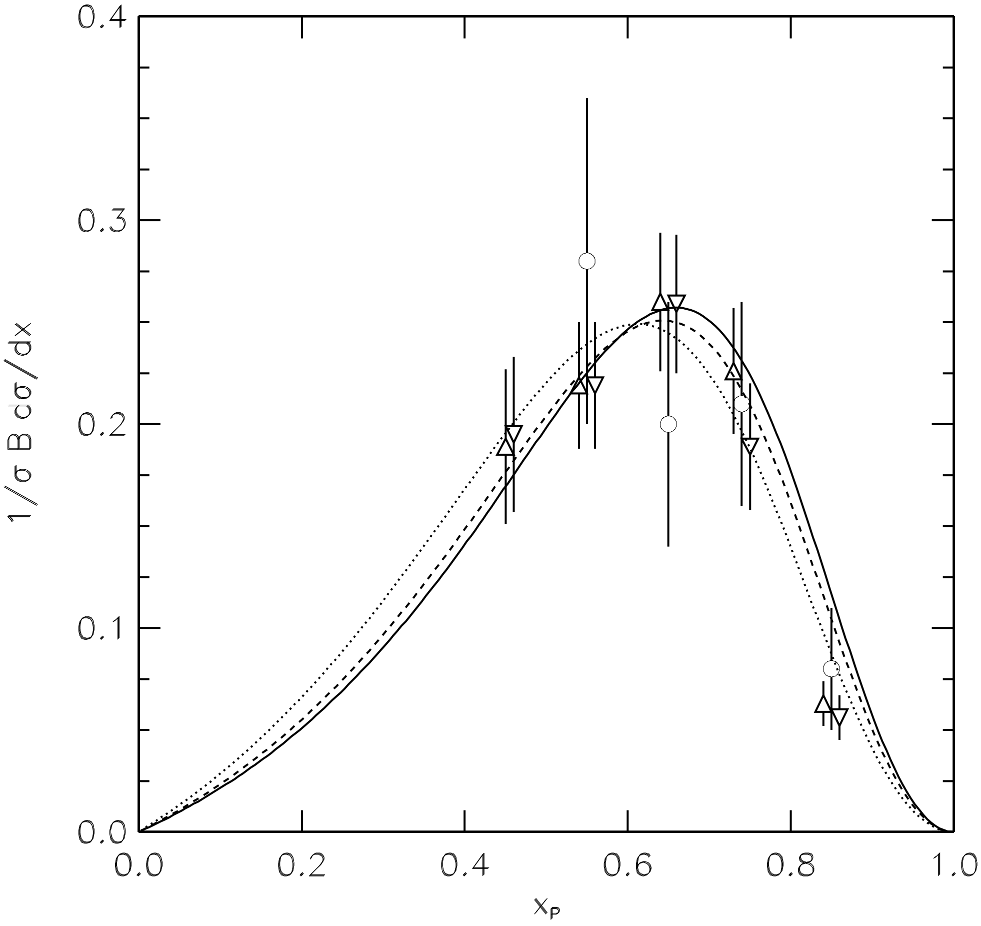

Figure 5.3: Normalized production spectra of scaled momentum for Σ_c samples. The data for the Σ_c^{++}(triangles), the Σ_c^{+}(circles), and the Σ_c^{0}(inverted triangles) are fitted to the Peterson functions overlaid as solid, dotted, and dashed curves, respectively.

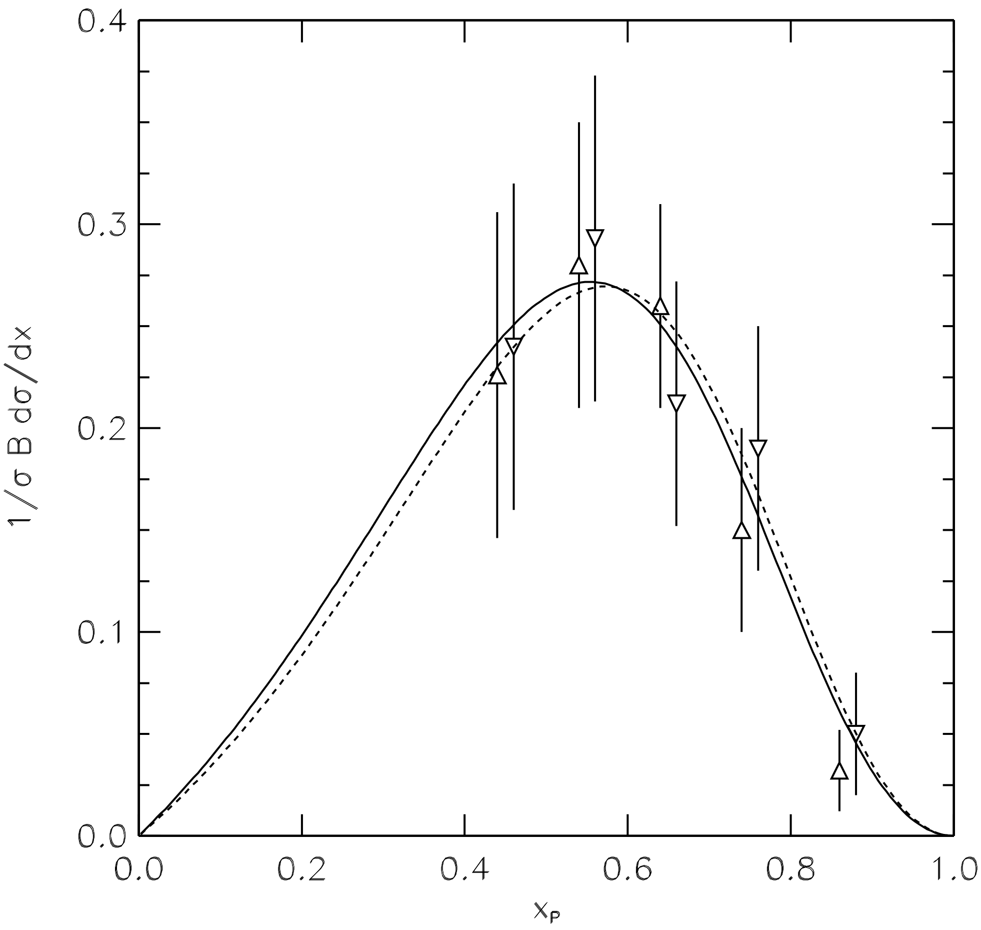

Figure 5.4: Normalized production spectra of scaled momentum for Σ_c^* samples. The data for the Σ_c^{*++}(triangles), and the Σ_c^{*0}(inverted triangles) are fitted to the Peterson functions overlaid as solid and dashed curves, respectively.

x_p range. The distributions are fitted using the Peterson function. Table 5.11 gives the measured values of ϵ for Σ_c's and Σ_c^*'s.

Our value of $\epsilon_P(\Sigma_c^{++} + \Sigma_c^0)$, 0.28 ± 0.03, is in agreement with the previous result, 0.29 ± 0.06, done by ARGUS[41] also in the 10 GeV/c^2 e^+e^- experiment. Our Σ_c^* values are also agree with the previous value, $\epsilon_P(\Sigma_c^{*++} + \Sigma_c^{*0}) = 0.30^{+0.10}_{-0.07}$.

Based on the measurements, it seems that $\Sigma_c^{(*)}$'s are fragmented slightly harder than Λ_c^+, which has $\epsilon_P = 0.25 \pm 0.03$[1] from 10GeV/$c^2$ e^+e^- annihilation. Λ_{c1}^+'s are obviously fragmented much harder. This is possibly because many Λ_{c1}^+'s are directly created from the annihilation, whereas a much larger fraction of $\Sigma_c^{(*)}$'s are the decay products from higher excited states.

5.6 Production Ratios

To calculate the ratio of the Λ_c^+ production from Σ_c and Σ_c^* decays relative to the total inclusive production, the reconstruction efficiencies of the Λ_c^+, the Σ_c, and the Σ_c^* from the Monte Carlo simulation are used. Our calculation covers the x_p region of 0.4 – 1.0 for $\Sigma_c^{(*)++}$ and $\Sigma_c^{(*)0}$, and 0.5 – 1.0 for the Σ_c^+. Since we measure the productions by ratio, most of the systematic errors on the Λ_c^+ reconstruction cancel. We estimate that the efficiency errors are 3% for $\Sigma_c^{(*)++}$ or $\Sigma_c^{(*)0}$ and 6% for the Σ_c^+. The statistical errors on the Monte Carlo efficiency calculation are tiny.

The uncertainty of the detector mass resolution brings large errors in the calculation of Σ_c^{++} and Σ_c^0 productions. We estimate this uncertainty by reducing and increasing the Monte Carlo resolution by 25% and comparing the areas of the Breit-Wigner distributions. We estimate this error to be $^{+7}_{-4}$%. Other fitting errors are mostly due to different background shapes, and they are tested to be no more than 3%.

Table 5.12: Measurements of the Σ_c production relative to total inclusive Λ_c^+ production from different experiments. All numbers are in units of %.

Experiment	Beam	$\sigma_{\Sigma_c^{++}}/\sigma_{\Lambda_c^+}$	$\sigma_{\Sigma_c^0}/\sigma_{\Lambda_c^+}$
E691	145 GeV γ	$5 \pm 3 \pm 2$	$13 \pm 4 \pm 2$
E687	220 GeV γ	6.7 ± 1.9	7.8 ± 2.1
NA32	230 GeV π^-	$< 5.2(90\% C.L.)$	$< 5.3(90\% C.L.)$
E791	500 GeV π^-	$6.7 \pm 1.0 \pm 1.0$	$7.9 \pm 1.1 \pm 1.0$
CLEO-I.5	10 GeV e^+e^-	6 ± 3	6 ± 3
CLEO-II(this)	10 GeV e^+e^-	$7.2 \pm 0.5 \pm 0.7$	$7.3 \pm 0.5 \pm 0.7$

Fitting procedures dominate the systematic errors for the Σ_c^+ and Σ_c^*'s, and the uncertainties on the resolution are much less important. We estimate the fitting errors are $^{+12}_{-8}\%$ for the Σ_c^+, $\pm 25\%$ for the two Σ_c^*'s.

We extrapolate the production distribution down to $x_p = 0$ of the Peterson function. The uncertainties on fragmentation function measurements bring large errors. This is not only because we lack the statistics to measure the fragmentation function accurately, but also because there is no reason to expect the Peterson function to perfectly represent the data. We estimate the errors in the extrapolations are 6% for the Σ_c^{++} and the Σ_c^0, 22% for the Σ_c^+, and 18% for Σ_c^*'s.

We finally assign the total systematic errors on production ratio measurements to be $^{+10}_{-9}\%$ for the $\Sigma_c^{++}$and the Σ_c^0, $^{+26}_{-24}\%$ for the Σ_c^+, and $\pm 31\%$ for Σ_c^*'s.

The background is not simply formed like the phase space of arbitrary particle combinations. We already know that there is wide enhancement around the region between 140 MeV/c^2 to 210 MeV/^{2} due to a feed-down of $\Lambda_{c1}^+(2625) \to \Lambda_c^+ \pi\pi$ decay. Very likely there are some other unknown physical processes making non-phase space contributions elsewhere in the mass-difference spectra, for instance, feed-down from more higher states of the Λ_c^+ and the Σ_c which decay into Λ_c^+'s.

Table 5.12 lists the measurements of $\sigma_{\Sigma_c}/\sigma_{\Lambda_c^+}$ for the Σ_c^{++} and Σ_c^0. The Σ_c^+ relative production ratio has not been measured by any previous experiments, and

Table 5.13: Measurements of Σ_c^* production ratio relative to total inclusive Λ_c^+ production in units of %.

Experiment	$\sigma_{\Sigma_c^{*++}}/\sigma_{\Lambda_c^+}$	$\sigma_{\Sigma_c^{*0}}/\sigma_{\Lambda_c^+}$	$(\sigma_{\Sigma_c^{*++}}+\sigma_{\Sigma_c^{*0}})/\sigma_{\Lambda_c^+}$
CLEO-II 1996			$12.8^{+1.5}_{-1.3} \pm 3.2$
CLEO-II (this)	$5.9^{+1.1}_{-0.9} \pm 1.8$	$7.8^{+1.9}_{-1.5} \pm 2.4$	$13.7^{+2.2}_{-1.7} \pm 3.0$

for the first time we have calculated that

$$\sigma_{\Sigma_c^+}/\sigma_{\Lambda_c^+} = 10.3 \pm 1.6 \pm 2.7\%.$$

Note if we fit the Σ_c^+ signal with fixed natural width the same as the Σ_c^0 signal, the result would be $7.5 \pm 1.1 \pm 2.0$. Also, if we assume that Σ_c's do not have natural widths and fit the signals with width-floated single Gaussians, the results on the Σ_c^{++} and the Σ_c^0 are 15% smaller and the result on the Σ_c^+ is 20% smaller.

Table 5.13 lists the $\sigma_{\Sigma_c^*}/\sigma_{\Lambda_c^+}$ measurements from CLEO. The new result, which agrees with the previous one, shows that the Σ_c^* and the Σ_c are nearly equally produced.

According to their spins, which are 1/2 for the Σ_c and 3/2 for the Σ_c^*, the number of Σ_c^*'s created should be two times as large as the number of Σ_c's from the e^+e^- annihilation. Then why is the number of Σ_c's in CLEO experiments even larger than 1/2 of Σ_c^*'s? As the Σ_c^* has higher mass, its creation should be slightly more suppressed than the creation of a Σ_c; however, we expect this to be a small effect. We think the real reason is very likely that there are more higher states which decay to the Σ_c than decay to the Σ_c^*. For instance, we know the decay $\Lambda_{c1}^+(2593)\rightarrow\Sigma_c\pi$ contributes about 20% of the Σ_c production.

5.7 New Measurements of $\Lambda_{c1}^{+}(2593)\to\Lambda_c^+\pi^+\pi^-$

According to our measurements, $\Lambda_{c1}^{+}(2593)$ decays almost 100% to $\Sigma_c\pi$, and using our average Σ_c^{++} and Σ_c^0 mass value, we can calculate that the kinematic threshold of $\Sigma_c^{++}\pi^-$ and $\Sigma_c^0\pi^+$ is at a mass difference of 306.86 MeV/c^2. Since this threshold is very close to the central mass of the resonance, the shape of the signal will not be an "ordinary" Breit-Wigner. We believe this is the reason why a Breit-Wigner convoluted with a Gaussian resolution does not fit the $\Lambda_{c1}^{+}(2593)\to\Lambda_c^+\pi^+\pi^-$ signal well as shown in Figure 5.5. The fit gives a ln(`Likelihood`)* value of 48.0 for 30 *d.o.f.*

If we assume that $\Lambda_{c1}^{+}(2593)$ decay 100% to $\Sigma_c\pi$, a reasonable way to fit the $\Lambda_{c1}^{+}(2593)\to\Lambda_c^+\pi^+\pi^-$ signal is to use a relativistic Breit-Wigner form[1, 52] with the amplitude

$$A_{BW}(\pi^\pm) = \frac{\sqrt{M\Gamma_r(\pi^\pm)}}{M_r^2 - M^2 - iM_r[\Gamma_r(\pi^0) + \Gamma_r(\pi^\pm)]}, \tag{5.1}$$

where M is the invariant mass of the $\Sigma_c\pi$ in the final state that results from the decay of the $\Lambda_{c1}^{+}(2593)$, M_r is the mass of the $\Lambda_{c1}^{+}(2593)$, and $\Gamma_r(\pi^0)$ and $\Gamma_r(\pi^\pm)$ are the mass-dependent widths of $\Lambda_{c1}^{+}(2593)$ corresponding to the decay $\Lambda_c^+\pi^0\pi^0$ and $\Lambda_c^+\pi^+\pi^-$, respectively. Note both $\Gamma_r(\pi^0)$ and $\Gamma_r(\pi^\pm)$ are in the denominator but only $\Gamma_r(\pi^\pm)$ is in the numerator. This is because we must put the "full" width in the denominator, and $\Lambda_{c1}^{+}(2593)$ has both $\Lambda_c^+\pi^0\pi^0$ and $\Lambda_c^+\pi^+\pi^-$ decay channels, but here we are only measuring the signal of the $\Lambda_c^+\pi^+\pi^-$ decay. We need a factor $\sqrt{M}$ in the numerator of the Breit-Wigner, because the phase space factor is a factor times $dM^2 = MdM$, and we are fitting the data as a function of M. The factor would not be present if we fit the data as a function of M^2. For $\Lambda_{c1}^{+}(2593)$, $M \gg \Gamma_r$, so this $\sqrt{M}$ factor virtually does not affect the Breit-Wigner shape. The normalization factor in equation 5.1 is omitted, and it is evaluated numerically in the fit procedure.

*ln(`Likelihood`) is the same as χ^2 for large statistics.

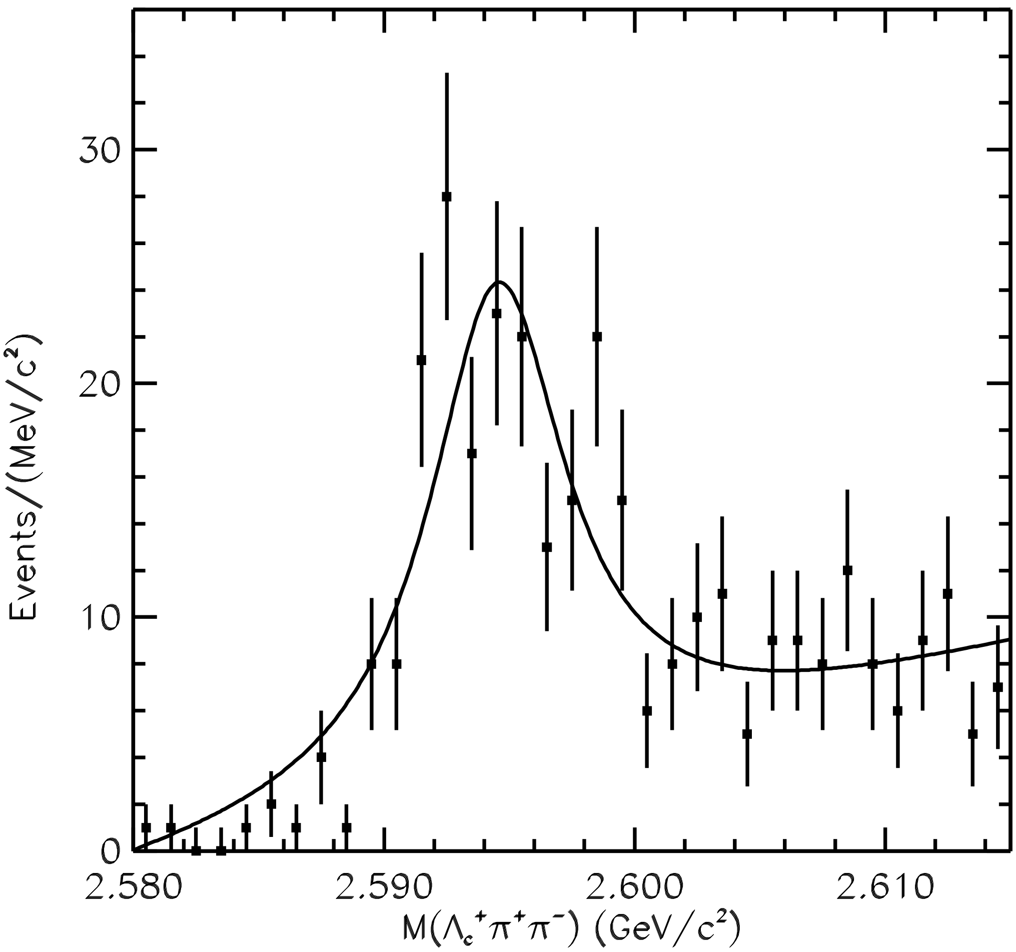

Figure 5.5: The fit to the $\Lambda_{c1}^+(2593)\rightarrow\Lambda_c^+\pi^+\pi^-$ signal using a simple Breit-Wigner function convoluted with the detector resolution. The mass-difference spectrum and the fit are the same as Figure 4.1, but here we only fitted $\Lambda_{c1}^+(2593)$ in order check the likelihood of the fit, and 1-MeV/c^2 bin size is shown instead of 1-MeV/c^2 in order to get a clearer view near the threshold.

For this relativistic Breit-Wigner function, the width parameter of the resonance is mass dependent. For a decay by a partial wave of orbital angular momentum L, the width can be described as

$$\Gamma_r = (p^*/M)^{2L} p^* a, \tag{5.2}$$

where p^* is the momentum in the rest frame of the resonance of either one of the daughters, and a is a mass-independent parameter. It has been tested in experiments that the width parameterization of equation 5.2 can reasonably fit to the mass-dependent width of P-wave decay of the ρ[53, 54].

$\Lambda_{c1}^+(2593) \to \Sigma_c^0 \pi^-$ is two-body decay, so we have

$$p^*(\Sigma_c^0 \pi^-) = \frac{[(M^2 - (M_{\Sigma_c^0} + M_{\pi^-})^2)(M^2 - (M_{\Sigma_c^0} - M_{\pi^-})^2)]^{\frac{1}{2}}}{2M}. \tag{5.3}$$

$p^*(\Sigma_c^+ \pi^0)$ and $p^*(\Sigma_c^{++} \pi^+)$ can be expressed similarly. In our fit procedure we assume that $M_{\Sigma_c^{++}} = M_{\Sigma_c^0}$; thus we have $p^*(\pi^\pm) = p^*(\Sigma_c^0 \pi^-) = p^*(\Sigma_c^{++} \pi^+)$. Since $\Lambda_{c1}^+(2593) \to \Sigma_c \pi$ is S-wave decay, according to equation 5.2,

$$\Gamma_r(\pi^\pm) = p^*(\pi^\pm) a(\pi^\pm), \tag{5.4}$$

$$\Gamma_r(\pi^0) = p^*(\pi^0) a(\pi^0), \tag{5.5}$$

From isospin symmetry, we can assume that $a(\pi^0) = \frac{1}{2} a(\pi^\pm)$. Now we have three parameters to fit the data: M_r, $a(\pi^\pm)$, and the area of the signal.

To fit the $\Lambda_{c1}^+(2593) \to \Lambda_c^+ \pi^+ \pi^-$ signal, we used the relativistic Breit-Wigner function as in the equation 5.1, smeared with a single Gaussian and a regular Breit-Wigner function. The Gaussian is used to parameterize the detector resolution of $\Lambda_{c1}^+(2593) \to \Lambda_c^+ \pi^+ \pi^-$, 1.28 MeV/$c^2$, determined by Monte Carlo studies; and the

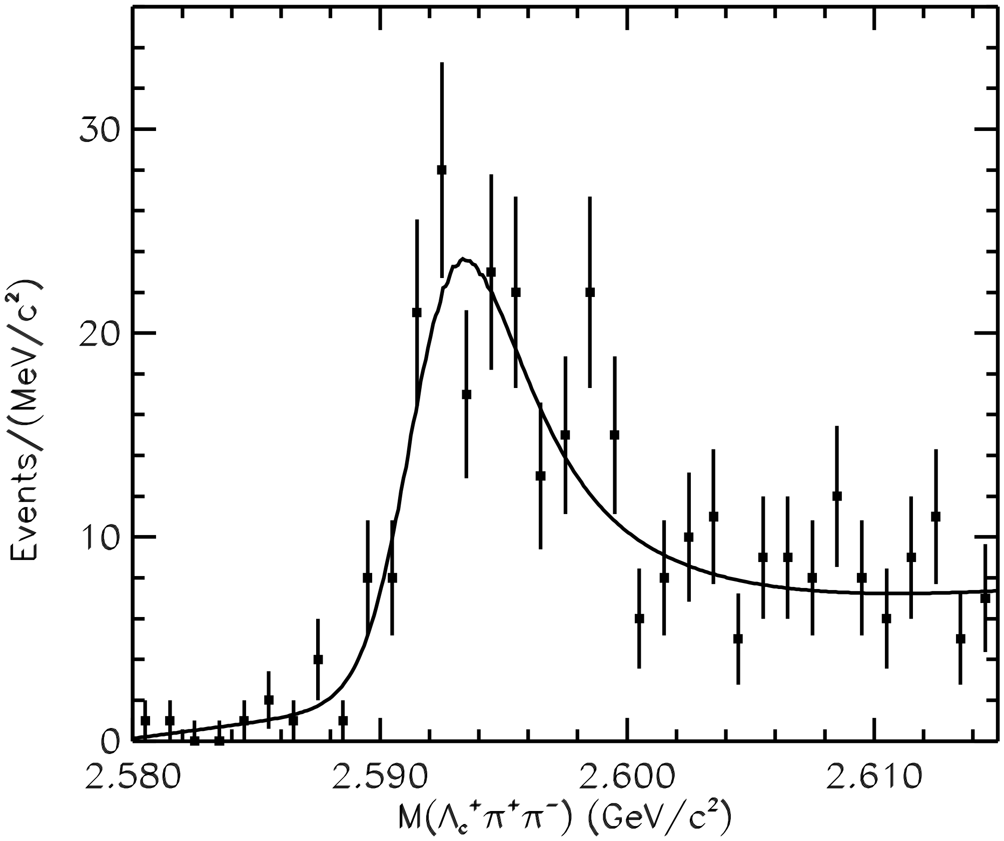

Figure 5.6: New fit to the $\Lambda_{c1}^{+}(2593)\to\Lambda_c^+\pi^+\pi^-$ signal using the relativistic Breit-Wigner function described in the text convoluted with the detector resolution and the Σ_c width.

Breit-Wigner represents the natural width of Σ_c^{++} or Σ_c^0, with an average value of 2.2 MeV$/c^2$. To input a Σ_c mass, we used the mass difference, 167.3 MeV$/c^2$, which is our measured average of Σ_c^{++} and Σ_c^0. The background is fitted by a second order polynomial with the area and shape floated. Figure 5.6 shows such a fit. The ln(`Likelihood`) value for the fit is 30.4 for 30 *d.o.f*, much better compared with 48.0 from the fit using the regular Breit-Wigner function.

The results of the fit shown in Figure 5.6, which are used as our presented values, are listed in the first row of the values in Table 5.14. In the following rows of the table, we tabulated the results obtained by different types of signal parameterization. The first three numbers in each row are input values of the fit and the last three

Table 5.14: Fit results of $\Lambda_{c1}^+(2593) \to \Lambda_c^+\pi^+\pi^-$ signal in Figure 5.6. The Σ_c mass difference (with Λ_c^+) ΔM_{Σ_c}, the Σ_c width Γ_{Σ_c}, and the $\Lambda_{c1}^+(2593) \to \Lambda_c^+\pi^+\pi^-$ mass resolution $\sigma_{\Lambda_{c1}^+}$ are fixed as the input to the fitting function. The mass difference (with Λ_c^+) of the $\Lambda_{c1}^+(2593)$, $a(\pi^\pm)$ and the yield of the signal are the measured parameters. All mass differences and widths in the table are shown in units of MeV/c^2.

Fixed parameter			Fitted parameter		
ΔM_{Σ_c}	Γ_{Σ_c}	$\sigma_{\Lambda_{c1}^+}$	$\Delta M_{\Lambda_{c1}^+}$	$a(\pi^\pm)$	Yield
167.3	2.2	1.28	305.3 ± 0.4	83^{+10}_{-8}	195^{+36}_{-34}
167.0	2.2	1.28	305.2	96	194
167.6	2.2	1.28	305.4	73	198
167.3	**0.7**	1.28	305.9	16	164
167.3	**1.5**	1.28	305.0	68	187
167.3	**2.8**	1.28	305.4	98	195
167.3	2.2	**1.00**	304.8	90	195
167.3	2.2	**1.70**	305.7	82	183

numbers are the extracted parameters. In each row except the first, there is a number shown in boldface in order to emphasis that this is the number we reasonably altered from the central value. Note that the mass, but not the mass difference, is used in the fit. So Λ_c^+ mass is actually used here. We proved that varying mass of Λ_c^+ by a few MeV/c^2 virtually does not changed the measured parameters. Although the $\Lambda_{c1}^+(2593)$ mass is measured, we still present the mass difference since it is a more accurate value.

From Table 5.14, we see that the measured mass slightly varies when other input parameters change. So all input parameters, within reasonable ranges, do not influence the value of the mass very much. Also note that the yield measured here is almost the same as the measurement described in Chapter 4 with similar statistical error and fitting error, thus all the $\Lambda_{c1}^+(2593)$ related branching ratios and production ratios measured in Chapter 4 still hold.

$a(\pi^{\pm})$ is very sensitive to changes of any input parameter, but we also notice that the shape of the resonance varies only slightly when $a(\pi^{\pm})$ changes. It seems that the a parameter is not proportional to the "width" of the signal, and the value of a is very sensitive to any change of parameterization near the threshold. We think the measurement of the a parameter in our fit is not very reliable, and the systematic error we quote is large.

Using the measured value of $a(\pi^{\pm})$ and assuming $a(\pi^{\pm}) = 2a(\pi^0)$, we can predict the branching ratio $\Gamma(\Lambda_c^+\pi^0\pi^0)/\Gamma(\Lambda_c^+\pi^+\pi^-)$ using the $A_{BW}(\pi^{\pm})$ formula in equation 5.1 and the similar formula for $\Sigma_c^+\pi^0$ decay,

$$A_{BW}(\pi^0) = \frac{\sqrt{M\Gamma_r(\pi^0)}}{M_r^2 - M^2 - iM_r[\Gamma_r(\pi^0) + \Gamma_r(\pi^{\pm})]}. \tag{5.6}$$

We found that

$$\Gamma(\Lambda_c^+\pi^0\pi^0)/\Gamma(\Lambda_c^+\pi^+\pi^-) = \begin{cases} 2.2 & \text{if } a(\pi^{\pm}) = 100, \\ 3.1 & \text{if } a(\pi^{\pm}) = 84, \\ 4.0 & \text{if } a(\pi^{\pm}) = 60. \end{cases}$$

This proves that the range of $a(\pi^{\pm})$ in Table 5.14 is consistent with our our measured $\Gamma(\Lambda_c^+\pi^0\pi^0)/\Gamma(\Lambda_c^+\pi^+\pi^-)$ in Chapter 4, which is $2.6 \pm 0.6 \pm 0.7$.

Similar to the $\Lambda_{c1}^+(2593)\to\Lambda_c^+\pi^+\pi^-$ case, we can also fit the $\Lambda_{c1}^+(2593)\to\Lambda_c^+\pi^0\pi^0$ signal using a Breit-Wigner function with the amplitude $A_{BW}(\pi^0)$ in equation 5.6. Note that $A_{BW}(\pi^0)$ is very close to a regular Breit-Wigner amplitude since the $\Sigma_c^+\pi^0$ threshold is at about 302 MeV/c^2, 4 MeV/c^2 below the center mass, and therefore fitting the $\Lambda_{c1}^+(2593)\to\Lambda_c^+\pi^0\pi^0$ signal using $A_{BW}(\pi^0)$* obtains almost the same mass

*Another way to do the measurement is to fit the $\Lambda_c^+\pi^+\pi^-$ and $\Lambda_c^+\pi^0\pi^0$ signals simultaneously by constraining them to have the same a's, but since $\Lambda_c^+\pi^0\pi^0$ signal is much poor, the measured parameters would be almost determined by the $\Lambda_c^+\pi^+\pi^-$ signal. We think it is more reasonable to fit them separately.

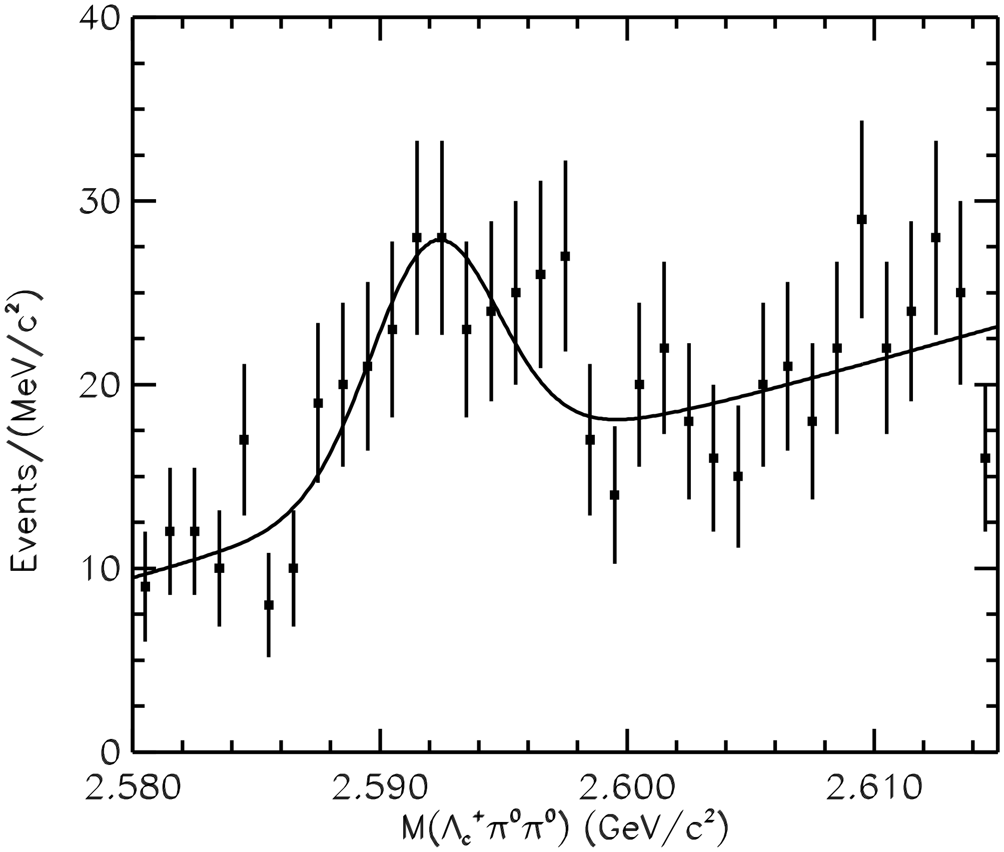

Figure 5.7: New fit to the $\Lambda_{c1}^+(2593) \rightarrow \Lambda_c^+\pi^0\pi^0$ signal using the relativistic Breit-Wigner function described in the text convoluted with the detector resolution and the Σ_c width.

and yield as the fit in Figure 4.3. Figure 5.7 shows such a fit. In the fit, we used a convoluting Gaussian with a width of 2.4 MeV/c^2, representing the $\Lambda_c^+\pi^0\pi^0$ mass resolution, and the same convoluting Breit-Wigner as we used to fit the $\Lambda_c^+\pi^+\pi^-$ signal*. However, due to low statistics, this fit measures the a parameter with enormous statistical error, so we cannot get more information about $A_{BW}(\pi^0)$ and $A_{BW}(\pi^\pm)$ by directly fitting them with the $\Lambda_c^+\pi^0\pi^0$ signal. Figure 5.7 shows a very good fit by fixing $A_{BW}(\pi^\pm)$ to be 83.

*Since the Σ_c^+ width is very poorly measured, we assume that it is the same as the Σ_c^{++} and Σ_c^0. The fit does not change much even if we use $\Gamma(\Sigma_c^+) = 4.5$ MeV/c^2.

Finally, using a new method never used on $\Lambda_{c1}^{+}(2593)$ in any previous experiments, we have measured $\Lambda_{c1}^{+}(2593)$ with the results

$$M(\Lambda_{c1}^{+}(2593) - M(\Lambda_{c}^{+}) = 305.3 \pm 0.4 \pm 0.6 \text{ MeV}/c^2,$$

$$a(\pi^{\pm}) = 83^{+10}_{-8} \pm 40.$$

The fitting error, 0.5 MeV/c^2evaluated from Table 5.14, dominates the total systematic error of $\Lambda_{c1}^{+}(2593)$ measurements. The error estimated from the momentum scale study is 0.2 MeV/c^2. The value of mass is significantly lower than the previously measured values using a normal Breit-Wigner as the fit function listed in Table 4.7. But the value is consistent with our mean value of $\Lambda_{c1}^{+}(2593)\rightarrow\Lambda_{c}^{+}\pi^0\pi^0$, 306.3 ± 0.7 MeV/c^2.

The fit using the lower limit of the Γ_{Σ_c}, 0.7 MeV/c^2, gives a very small a. Although the fit is acceptable, it is not used to evaluated the systematic error of the $a(\pi^{\pm})$ value because the 0.7 MeV/c^2 limit is far beyond one unit of standard deviation. More careful studies are needed about the a parameter of $\Lambda_{c1}^{+}(2593)$ in both theoretical models and experiments.

CHAPTER 6
SUMMARY AND DISCUSSION

In this research, we have made a complete study of eight charmed baryons: the Λ_{c1}^+ doublet, which decays to $\Lambda_c^+\pi\pi$, and the Σ_c triplet and the Σ_c^* triplet which decay to $\Lambda_c^+\pi$.

With a large data sample and improved detector resolution, we measured the Σ_c masses more accurately than previous experiments, and the results are $167.3 \pm 0.1 \pm 0.2\mathrm{MeV}/c^2$ for Σ_c^{++}, $166.9 \pm 0.5 \pm 0.3\mathrm{MeV}/c^2$ for Σ_c^+, and $167.2 \pm 0.1 \pm 0.2\mathrm{MeV}/c^2$. Our results do not indicate any noticeable isospin mass splittings among this triplet.

Studying the mass splitting among baryons containing different-valence quarks is a good way to understand hadronic structure and the forces which determine the structure. The mass splittings in the charm baryon system are especially interesting since the large mass of the c quark simplifies the component structure in theoretical models so the experimental tests are more meaningful. The Σ_c is the first baryon isospin multiplet for which the intrinsic light-quark mass difference is not the dominating factor of the isospin mass splitting. However, the theoretical predictions vary largely for different models. Our results support that the splittings are very small, and the numbers are close to the prediction by Chan[46].

In this work, the Σ_c widths were measured for the first time, and the results are $2.1 \pm 0.3^{+0.3}_{-0.5}$ MeV$/c^2$ for Σ_c^{++}, $4.5^{+2.1+1.0}_{-1.7-1.5}$ MeV$/c^2$ for Σ_c^+, and $2.3^{+0.4+0.4}_{-0.3-0.5}$ MeV$/c^2$ for Σ_c^0. These values are in very good agreement with the prediction of heavy-quark chiral perturbation theory[16]. We measured the Σ_c^* widths $\Gamma(\Sigma_c^{*++}) = 14 \pm 3 \pm 3$ MeV$/c^2$ and $\Gamma(\Sigma_c^{*0}) = 20^{+5}_{-4} \pm 5$ MeV$/c^2$. These are consistent with the previous measurement by CLEO[21]. Note that based on equations 1.3 and 1.5, the Σ_c and

Σ_c^* widths are correlated with each other through the coupling constant g_2. Our results agree with the g_2 value predicted by many theoretical models.

We have confirmed the previous Σ_c^{*++} and Σ_c^{*0} observation made by CLEO, with masses measured to be $231.4 \pm 0.8^{+0.9}_{-0.5}$ MeV$/c^2$ for the Σ_c^{*++} and $231.9 \pm 1.2^{+1.2}_{-0.7}$ MeV$/c^2$ for the Σ_c^{*0}, and the widths measured to be $14 \pm 3 \pm 3$ MeV$/c^2$ for the Σ_c^{*++} and $20^{+5}_{-4} \pm 5$ MeV$/c^2$ for the Σ_c^{*0}, all consistent with previous results. In addition, for the first time we observed the Σ_c^{*+} evidence, with the mass measured to be $229.2 \pm 1.3 \pm 0.5$ MeV$/c^2$ and the width measured to be 5^{+6+3}_{-5-2} MeV$/c^2$.

We have measured the ratios of the Λ_c^+ productions from $\Sigma_c^{(*)}$ relative to the total inclusive Λ_c^+ production from the 10GeV$/c^2$ e^+e^- production, and the results are $7.2 \pm 0.5 \pm 0.7\%$ from Σ_c^{++}, $10.3 \pm 1.6 \pm 2.7\%$ from Σ_c^+, $7.3 \pm 0.5 \pm 0.7\%$ from Σ_c^0, $5.9^{+1.1}_{-0.9} \pm 1.8\%$ from Σ_c^{*++}, and $7.8^{+1.9}_{-1.5} \pm 1.8\%$ from Σ_c^{*0}. We are unable to make a Σ_c^{*+} measurement since the signal is too poor. This is the first time that $\sigma_{\Sigma_c^+}/\sigma_{\Lambda_c^+}$ is measured, and all the other ratios measured are in agreement with previous experiments. Based on our measurements, we can conclude that $25 \pm 4\%$ of Λ_c^+'s are from Σ_c decays. If we assume the three Σ_c^*'s are equally produced, then about 20% of Λ_c^+'s are produced from Σ_c^* decays.

The following evidences provide very strong proof that these two states are indeed Λ_{c1}^+ baryons with light degrees of freedom having $L = 1$: (1) the $\Lambda_c^+\pi^0$ signals are not seen; (2) the $\Sigma_c\pi$ channel transition dominates the $\Lambda_c^+(2593)$ decay and the same channel is measured small for $\Lambda_{c1}^+(2625)$; and (3) the $\Lambda_c^+\pi^0\pi^0$ channel is observed for both Λ_{c1}^+'s.

This is the first time the $\Lambda_c^+\pi^0\pi^0$ decay channel has been observed, and the relative decay ratio $\mathcal{B}(\Lambda_c^+\pi^0\pi^0)/\mathcal{B}(\Lambda_c^+\pi^+\pi^-)$ is measured to be $2.6 \pm 0.6 \pm 07$ for $\Lambda_{c1}^+(2593)$ and $1.0 \pm 0.3^{+0.3}_{-0.2}$ for $\Lambda_{c1}^+(2625)$. The value for $\Lambda_{c1}^+(2593)$ does not agree with isospin symmetry but can be explained by phase-space suppression.

The $\Lambda_{c1}^+(2625)$ mass was measured to be $341.80 \pm 0.10 \pm 0.35$ MeV/c^2. We measured the upper limit of the $\Lambda_{c1}^+(2625)$ width to be 1.4 MeV/c^2 at 90% confidence level. These values agree with previous experiments.

By fitting the $\Lambda_{c1}^+(2593)\to\Lambda_c^+\pi^+\pi^-$ signal the same way as the previous experiments, it is measured to have a mass $308.8 \pm 0.4 \pm 0.4$ MeV/c^2 and a width $4.7^{+1.3+1.4}_{-1.1-0.9}$ MeV/c^2 which are consistent with previous results but not consistent with our $\Lambda_{c1}^+(2593)\to\Lambda_c^+\pi^0\pi^0$ measurements, in which we measured the mass to be 306.3 ± 0.7 MeV/c^2. But these measurements are based on the signal parameterization using an ordinary Breit-Wigner function. Because $\Lambda_{c1}^+(2593)$ resonance is just at the $\Sigma_c\pi^\pm$ kinematic threshold, a relativistic Breit-Wigner function should be used. In this function, the width of a resonance is mass dependent and can only be parameterized by the a parameter. Using the new method, we obtained very good fit and measured the $\Lambda_{c1}^+(2593)$ to have a mass $305.3 \pm 0.4 \pm 0.6$ MeV/c^2. Assuming that $a(\pi^\pm) = 2a(\pi^0)$ based on isospin symmetry, we measured $a(\pi^\pm) = 83^{+10}_{-8} \pm 40$. These new measured values are consistent with our $\Gamma(\Lambda_c^+\pi^0\pi^0)/\Gamma(\Lambda_c^+\pi^+\pi^-)$ result, $2.6 \pm 0.6 \pm 0.7$.

The non-relativistic quark potential model[6] fails in its prediction of the Λ_{c1}^+ masses. The relativized model is close, but their 10 MeV/c^2 spin-orbital mass splitting is too small.

The mass splitting between the two Λ_{c1}^+ states is $36.5 \pm 0.4 \pm 0.6$ MeV/c^2 from our measurements, about 4 MeV/c^2 larger than $32.4 \pm 1.0 \pm 0.7$ MeV/c^2 measured by ARGUS[32]. From heavy-quark symmetry, we should expect that

$$M(\Lambda_{c1}^+(2625)) - M(\Lambda_{c1}^+(2593)) = M(D_2^*(2460)^0) - M(D_1(2420)^0).$$

The PDG[1] average value of $M(D_2^*(2460)^0) - M(D_1(2420)^0)$ is 37 ± 3 MeV/c^2. We see that HQET works quantitatively very well in this case.

To date, few theoretical models directly predicted the Λ_{c1}^+ widths. The most recent calculation was made by Tawfiq et al.[55]. They used a light-front constituent quark model which utilized the SU($2N_f$)$\times$O(3) diquark symmetry, where N_f represents the number of light flavors. Assuming the mass of a light quark to be 340 MeV/c^2, they predicted that $\Gamma(\Lambda_{c1}^+(2593) \to \Sigma_c\pi)$ is around $1.6 \sim 2.5$ MeV/c^2. They also predicted the D-wave transition rate $\Gamma(\Lambda_{c1}^+(2625) \to \Sigma_c\pi)$ to be about 0.7 MeV/c^2. But our measurements contradict these values. No model has directly predicted the widths of non-resonance two-pion transitions. Better Monte Carlo simulation and detector resolution are needed to perform further measurement of the $\Lambda_{c1}^+(2625)$ width.

Theoretical computations[56] give small values of of decay rates of the radiative $\Lambda_{c1}^+ \to \Lambda_c^+\gamma$ decays: 0.016 MeV/$c^2$for $\Lambda_{c1}^+(2593)$ and 0.021 MeV/$c^2$for $\Lambda_{c1}^+(2625)$. According to these values we should not be able to see $\Lambda_{c1}^+(2593) \to \Lambda_c^+\gamma$ since its width is obviously large, and we might be able to see $\Lambda_{c1}^+(2593) \to \Lambda_c^+\gamma$ if $\Gamma(\Lambda_{c1}^+(2625)) \to \Lambda_c^+\pi^+\pi^-$ is very narrow. We did not find any evidence of $\Lambda_{c1}^+ \to \Lambda_c^+\gamma$ decays. The upper limit we measured is too large to provide any indications.

REFERENCES

[1] Particle Data Group. Review of particle physics. *The European Physical Journal C*, 3(1-4), 1998.

[2] K. Wilson. *Phys. Rev.*, D10:2445, 1974.

[3] J. Kogut and L. Susskind. *Phys. Rev.*, D9:3501, 1974.

[4] S. Capstick and N. Isgur. *Phys. Rev.*, D34:2809, 1986.

[5] K. Maltman and N. Isgur. *Phys. Rev.*, D22:1701, 1980.

[6] L. Copley, N. Isgur, and G. Karl. *Phys. Rev.*, D20:768, 1979.

[7] H. Politzer and M. Wise. *Phys. Lett.*, B208:504, 1988.

[8] H. Politzer and M. Wise. *Phys. Lett.*, B206:681, 1988.

[9] N. Isgur and M. Wise. *Phys. Lett.*, B232:133, 1989.

[10] N. Isgur and M. Wise. *Phys. Lett.*, B237:527, 1990.

[11] E. Eichten and B. Hill. *Phys. Lett.*, B234:511, 1990.

[12] H. Georgi. *Phys. Lett.*, B240:447, 1990.

[13] B. Grinstein. *Nucl. Phys.*, B339:253, 1990.

[14] N. Isgur and M. Wise. *Nucl. Phys.*, B348:276, 1991.

[15] H. Georgi. *Nucl. Phys.*, B348:293, 1991.

[16] T.-M. Yan, H.-Y. Cheng, C.-Y. Cheung, G.-L. Lin, Y. Lin, and H.-L. Yu. *Phys. Rev.*, D46(3):1148, 1992.

[17] A. Manohar and H. Georgi. *Nucl. Phys.*, B234:189, 1984.

[18] A. Chodos. *Phys. Rev.*, D10:2599, 1974.

[19] M. Khanna and R. Verma. *Z. Phys.*, C7:275, 1990.

[20] S. Coleman and S. Glashow. *Phys. Rev.*, 134B:670, 1964.

[21] CLEO Collaboration. *Phys. Rev. Lett.*, 78:2304, 1997.

[22] D. Pirjol and T.-M. Yan. *Phys. Rev.*, D56(9):5483, 1997.

[23] CLEO Collaboration. *Phys. Rev.*, D57:4467, 1998.

[24] C. Prescott. The knvf secondary vertex finding package. *CLEO CSN*, 97/353, 1997. (unpublished).

[25] Brock I. Mn_fit - a fitting and plotting package using minuit. *L3 Note*, 918, 1995.

[26] Minuit - function minimization and error analysis. *CERN Program Library*, D506.

[27] CLEO Collaboration. *Phys. Rev.*, D43:3599, 1991.

[28] ARGUS Collaboration. *Phys. Lett.*, B317:227, 1993.

[29] FNAL E687 Collaboration. *Phys. Rev. Lett.*, 72:961, 1994.

[30] CLEO Collaboration. *Phys. Rev. Lett.*, (74):3331, 1995.

[31] FNAL E687 Collaboration. *Phys. Lett.*, B365:461, 1996.

[32] ARGUS Collaboration. *Phys. Lett.*, B402:207, 1997.

[33] C. Peterson, D. Schlatter, I. Schmitt, and P. M. Zerwas. *Phys. Rev.*, D27:105, 1983.

[34] CLEO Collaboration. *Phys. Rev.*, D37:1719, 1988.

[35] ARGUS Collaboration. *Z. Phys.*, C(52):353, 1991.

[36] CLEO Collaboration. *Phys. Rev.*, D37:1719, 1988.

[37] BNL. *Phys. Rev. Lett.*, 34:1125, 1975.

[38] COLU and BNL. *Phys. Rev. Lett.*, 42:1721, 1979.

[39] BEBC TST Neutrino Collaboration. *Phys. Lett.*, 93B(4):521, 1980.

[40] E400 Collaboration. *Phys. Rev. Lett.*, 59(24):2711, 1987.

[41] ARGUS Collaboration. *Phys. Lett.*, B211(4):489, 1988.

[42] CLEO Collaboration. *Phys. Rev. Lett.*, 62(11):1240, 1989.

[43] CLEO Collaboration. *Phys. Rev. Lett.*, 71(20):3259, 1993.

[44] E791 Collaboration. *Phys. Lett.*, B379:292, 1996.

[45] E687 Collaboration. *Phys. Lett.*, B365:461, 1996.

[46] L-H. Chan. *Phys. Rev.*, D31:204, 1985.

[47] W-Y. Hwang and D. Lichtenberg. *Phys. Rev.*, D35:3526, 1987.

[48] A. Wright. *Phys. Rev.*, D17:3130, 1978.

[49] N. Deshpande. *Phys. Rev.*, D15:1885, 1977.

[50] S. Sinha. *Phys. Lett.*, B218:333, 1989.

[51] S. Capstick. *Phys. Rev.*, D31:204, 1985.

[52] J. Jackson. *Il Nuovo Cimento*, XXXIV:1644, 1964.

[53] J. Pisut and M. Roos. *Nucl. Phys.*, B6:325, 1968.

[54] V. Chabaud. *Nucl. Phys.*, B223:1, 1983.

[55] A. Tawfiq, P. O'Donnell, and J. Körner. On p-wave to s-wave pion transitions of charmed baryons. *UTPT*, 98-08. (Unpublished).

[56] C. K. Chow. *Phys. Rev.*, D54:3374, 1996.

BIOGRAPHICAL SKETCH

Jiu Zheng was born in Tangshan, Hebei province, China on October 7, 1965. After ten years of elementary education in Beijing, he enrolled in the Department of Physics of Peking University in 1983. After obtained his Bachlor of Science degree in 1987, he worked as an electrical and cryogenic engineer in the Natural Constant Group of the National Institute of Metrology for six years. He began studying at the University of Florida in 1993, and he has conducted research in the CLEO collaboration since 1994.